NUMERICAL MODELING OF PROGRESSIVE AND RETROGRESSIVE FAILURE OF SUBMARINE SLOPES WITH A SENSITIVE CLAY LAYER

by

© SHUBHAGATA ROY

A thesis submitted to the

School of Graduate Studies

in partial fulfillment of the requirements for the degree of

Master of Engineering

Faculty of Engineering and Applied Science

Memorial University of Newfoundland

May, 2018

St. John's   Newfoundland   Canada

ABSTRACT

Submarine landslides are major concerns in offshore oil and gas development activities, as they can displace an enormous amount of sediment compared to onshore landslides. Among the different triggering factors identified in the past, the presence of a weak strain-softening clay layer and earthquake loading have been considered the primary causes of many large-scale landslides. Depending upon geometry, loading conditions and sediment properties, different types of failure patterns (e.g., slab, spread, ploughing, run-out) have been observed in the field. In the present study, a Eulerian-based finite-element (FE) approach in Abaqus software is used to study large-scale submarine landslides for varying slope angles.

The main objective of the present study is to numerically simulate the failure of submarine slopes with strain-softening clay layers triggered by two factors: i) shear strength reduction in a thin zone of soil which could be occurred due to gas hydrate dissociation, and ii) earthquake loading. Two approaches are used to model earthquake loading: (i) complete dynamic modeling base on acceleration–time history and (ii) modified pseudostatic loading with a simplified pulse of horizontal acceleration. A model for strain-softening behaviour of clay is implemented in the FE simulation, and analyses are performed for varying slope angles over a large seabed section. The FE simulations show that an initial shear band of sufficient length parallel to the seabed in the steeper part of the slope could cause a large-scale landslide by progressive formation of failure planes, both in upslope and downslope areas. In upslope areas, the failure pattern is similar to spreads commonly observed in sensitive clay slopes in onshore environments. In downslope areas, the failures tend to be similar to ploughing. The obtained failure patterns, ploughing distances, and retrogression distances for both types of earthquake loading are compared. Simple pulse-type pseudostatic loading can be used to reasonably model earthquake-induced landslides.

ACKNOWLEDGEMENTS

Table of Contents

List of Figures

List of Tables

List of Symbols

The following symbols are used in this thesis:

β slope angle

β' stiffness proportional damping

γ' submerged unit weight of soil

δ accumulated plastic shear displacement

δ_{pc} plastic shear displacement at point b in Fig. 3.2

δ_e elastic shear displacement

δ_{95} δ at which s_u reduced by 95% of (s_{up}-s_{uR})

δ_{ld} large displacement

δ_{total} total displacement

$\epsilon_q^p = \text{PEEQVAVG}$ equivalent plastic shear strain

γ^p plastic shear strain

$\dot{\epsilon}_{ij}^p$ plastic deviatoric strain rate tensor

ν_u undrained Poisson's ratio

k_m peak horizontal acceleration

E_u undrained Young's Modulus

F_s factor of safety

k_h horizontal seismic coefficient

k_c critical horizontal acceleration

M moment magnitude of earthquake

S_t sensitivity of clay, s_{up}/s_{uR}

s_u mobilized undrained shear strength

s_{up} peak undrained shear strength

s_{uR} remolded s_u at large plastic shear displacement

t_{FE} FE mesh size

t FE analysis time

T predominant period

t_{sig} significant duration of earthquake ground motion

a_h horizontal acceleration due to the earthquake

F_h horizontal seismic force

m   total mass of the slide soil

W   total weight of the slide soil

v_m peak ground velocity

g   gravitational acceleration

A_{RMS} root mean square of acceleration

Dur_{ac} duration for which acceleration is greater than yield acceleration

S_a spectral acceleration with 5% damping at 1 s

N_{eq} equivalent number of uniform cycles

I_a Arias intensity

α $\sin^{-1}(k_c/k_m)$

ϕ' angle of internal friction

L_{cr} critical length of shear band

H_m thickness of marine clay layer

H_g thickness of glacial clay layer

PI   plasticity index

L length of the model

L_ms length of the marine clay layer in the stable zone

h_p height of the accumulated soil in the ploughing area

EVF   Eulerian volume fraction

L_E lateral extent of the landslide

L_R retrogression distance

L_P ploughing distance

L_S slope length

CHAPTER 1

Introduction

1.1   General

A submarine landslide is a large-scale movement of sediments wherein the failed soil mass might travel a large distance over the continental shelf. Submarine landslides can pose a serious threat to human life and can damage offshore infrastructures, such as communication cables and offshore pipelines. Although submarine landslides are not visible, they have damaged not only offshore structures but also many coastal areas worldwide. Figure 1.1 shows 50 major submarine (black triangle) and subaerial landslides (white triangle) that have occurred around the world.
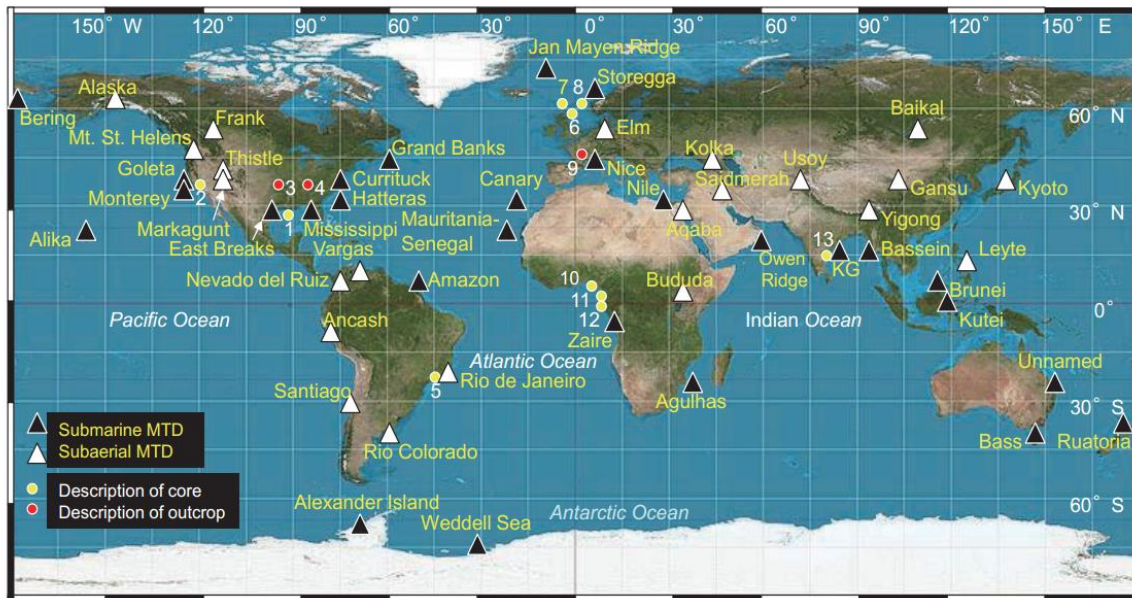
Figure 1.1: Location of 50 submarine (black triangle) and subaerial landslides (white triangle) (after Shanmugam and Wang 2015)

Examples of large-scale submarine landslides are the Storegga Slide in Norway (Bugge et al. 1987; Haflidason et al. 2005; Kvalstad et al. 2005a), the Chamais slump in the SE African margin (Dingle

1980), the Agulhas slump in the SE African margin (Dingle 1977), the Insular Slope slide in Puerto Rico (Schwab et al. 1993), the Brunei slide in NW Borneo (Gee et al. 2007), the Slump complex in Israel (Martinez et al. 2005), the Bassein slide in the NE Indian Ocean (Moore et al. 1976), the Nile slide in offshore Egypt (Newton et al. 2004), the Copper River slide in the northern Gulf of Alaska (Carlson and Molnia 1977), the Cape Fear slide (Popenoe et al. 1993; Lee 2009), the Currituck slide (Locat et al. 2009) in the U.S. Atlantic Margin, and the Grand Banks slide in Newfoundland (Piper and Aksu 1987; Piper et al. 1999; Bornhold et al. 2003).

Most of the studies have examined the morphology of these landslides. For example, the Storegga Slide involved ~ 5,600 km^3 volume of failed sediments and the total run-out distance was ~ 800 km. The headwall of the slide scar was 290 km long and the gradient was ~ 10° to 20° (Bugge et al. 1987; Harbitz 1992; Canals et al. 2004). According to the seismic data, the presence of relatively soft and fine-grained sediments (i.e., a weak zone) can initiate a failure due to an earthquake combined with the decomposition of gas hydrates. The failure surface propagates retrogressively with the formation of a series of grabens and ridges (Kvalstad et al. 2005a).

The Chamais Slump was composed of large rotated sediment blocks up to 20 km across and having thicknesses of around 225 m or less (Dingle 1980). The seabed floor in the proximal region is stepped, and in the distal parts the seabed is relatively smooth. The seismic profile of the southern boundary of the Chamais Slump showed a graben-like structure with perched blocks and large detached blocks. An earthquake could have been triggered this slump (Dingle 1980; Shanmugam and Wang 2015).

In the Agulhas Slump, four main features have been identified: a wide fissured zone, a prominent glide plane scar, a tensioned depression at the upper end, and a concave glide plane under the

2

slumped mass (Dingle 1977). The extent and movement in the downward direction appear to be greater than in any previous submarine slump.

The steep insular slope off Puerto Rico failed due to a strong earthquake shaking and a reduction of pre-existing faults that underlay the amphitheater-shaped headwall scarp, which is inclined at 8.5° (Schwab et al. 1992).

The Brunei Slide was located on an active convergent margin with a steep upper slope (> 4°), and rafted landslide blocks, and widespread basal sliding and erosion were observed. The presence of gas and gas hydrates might have caused the triggering (Gee et al. 2007).

In the Israel slump complex, basal shear surfaces are observed both upslope and downslope. In the upslope areas, a retrogressive failure occurred, together with formation of a depletion zone, which is characterized by extensional deformation and thinning of the slump mass. The failed soil mass accumulated downslope, and is characterized by compressional deformation and thickening of the slumped mass (Martinez et al. 2005).

The Currituck Slide took place due to excess pore water pressure and seismic acceleration, leading to a reduction in the soil strength. Two slides were observed, one in the lower escarpment (15° – 30°) and the other in the upper escarpment (9° – 10°) (Prior et al. 1986; Locat et al. 2009).

The Grand Banks Slide was triggered by an earthquake of magnitude 7.2, and failure occurred in a seabed that inclined between 6° and 10° (Piper et al. 1999).

The common features of these submarine landslides are: (a) the failure initiated due to one or more triggering factors; (b) the initial failure generally occurred in a steeper section of the seabed; (c) the slides propagated retrogressively in the upslope stable or less inclined areas; and (d) the slides might also have propagated in the downslope stable area, and the accumulated soil displaced in

the downslope direction (run-out); and (e) a typical large-scale landslide involves the failure of a large number of soil blocks.

During the last few decades, geo-marine surveys and mapping of the seabed have increased significantly around the world with the development of offshore petroleum projects. Geo-marine surveys using modern remote sensing equipment can provide high-resolution seafloor maps and more detailed information about seabed profiles. The high-resolution seafloor maps are used to evaluate the soil morphology of the seafloor and future failure possibilities in previous sliding zones, such as the Norwegian margin, Gulf of Mexico, offshore California, the U.K. Atlantic Margin, offshore Brazil, the Caspian Sea, and West Africa. Some conceptual models have also been proposed (e.g., Gee et al. 2005; Kvalstad et al. 2005a). However, the complete processes of submarine slope failure and sediment transport into the deep sea are still poorly understood. An advanced numerical modeling technique is presented in this thesis using the concept of soil mechanics to explain large submarine landslides.

Large submarine landslides are more common in inclined areas of the seabed, and the mass movement is larger than that in onshore landslides. Most offshore slopes' profile angles are not constant, and can contain a combination of steep, mild, and even zero-degree slopes. The offshore profile might contain one or multiple clay layers having strain-softening behaviour. The possibility of submarine landslides increases when a weak material such as a marine sensitive clay layer exists (Bryn et al. 2005; Kvalstad et al. 2005a; Dan et al. 2007; Dey et al. 2016). The initial failure of a submarine slope can start from a small weak zone of the steeper slope and extent downslope by propagation of failure plane (see Fig. 1.2). The failure through the weak zone can initiate due to a single triggering factor or a combination of different triggering factors such as an earthquake, the presence of a weak layer, gas hydrates, rapid sedimentation and salt tectonism.
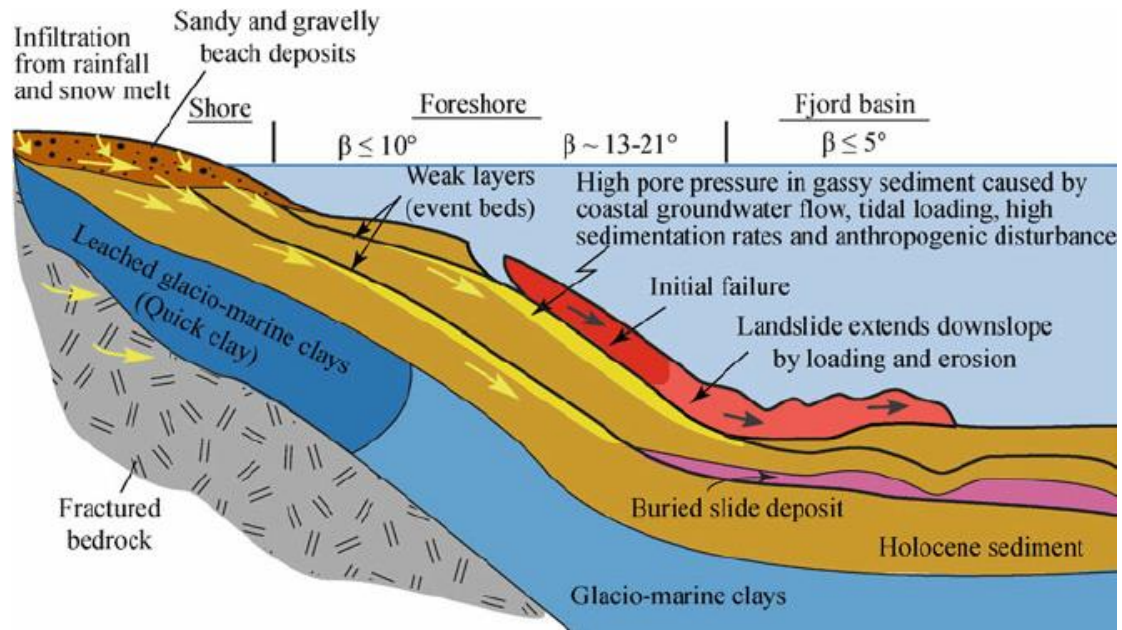
Figure 1.2: Schematic presentation of a submarine landslide (after L'Heureux et al. 2012)

Earthquake-induced submarine landslides are a major issue in offshore environments. Most landslides in offshore environments are triggered by earthquakes. During an earthquake, an initial failure surface develops locally and then propagates further causing global failure of soil blocks. The failure occurs not only during the earthquake (co-seismic stage) but also after the earthquake (post-quake stage).

A wide range of failure patterns has been identified in submarine landslides that involve sensitive clay layers. Among them, the notable types are horsts and grabens, rotational slide, tabular block slide, formation of steep and high head scarps, multiple shear surfaces, or polished head scarp failures (Gee et al. 2005; Kvalstad et al. 2005a; Solheim et al. 2005; Locat et al. 2009; Dey et al. 2016). For example, Fig. 1.3 shows the bathymetry and seismic profile of the Storegga Slide. The horsts (Λ-shaped blocks) and grabens (V-shaped blocks) in this slide are similar to those observed in typical onshore landslides in sensitive clay slopes in Eastern Canada and Scandinavia.
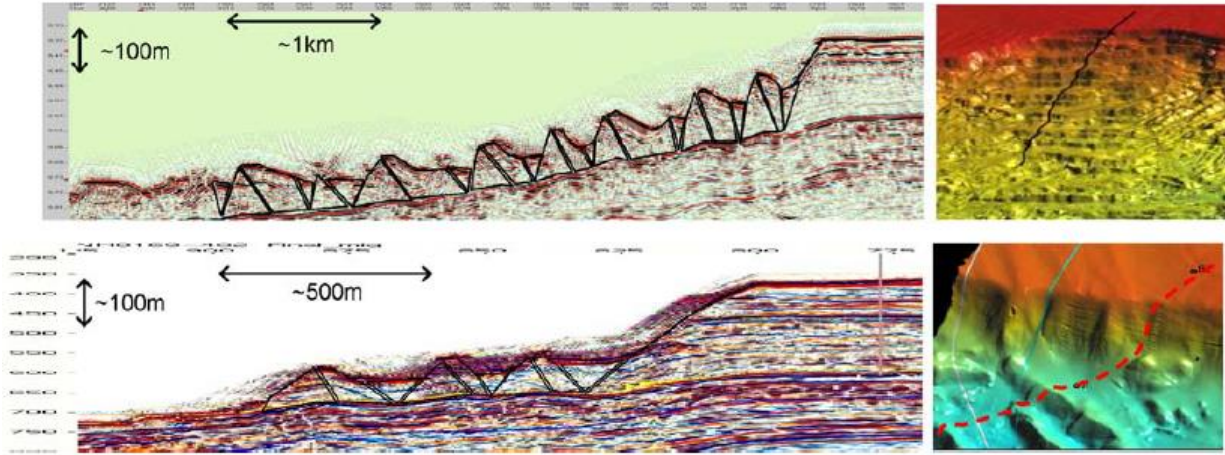
Figure 1.3: Bathymetry and seismic profiles of the Storegga Slide (Kvalstad et al. 2005a)

1.2   Scope of the research

The stability of a slope is commonly assessed using the traditional Limit Equilibrium (LE) method. For an earthquake loading, the LE method uses the pseudostatic approach, where an equivalent static horizontal force due to an earthquake is applied at the center of the sliding mass, in addition to static loads. The LE analysis provides a factor of safety (F_s); however, it cannot calculate the displacement of the failed soil mass and progressive failure, as commonly occurs in large-scale landslides, especially when the failure involves soils with strain-softening behaviour.

Over the past couple of decades, different computer programs have been developed for modeling of soil behaviour in boundary value problems, and some of them are available in commercial software packages (e.g., Abaqus, PLAXIS). Most of the FE modeling tools are developed on a Lagrangian framework. Unfortunately, numerical modeling of large deformation problems—including the modeling of sensitive clay slope failures, as considered in the present study—cannot be performed properly using the typical Lagrangian-based FE programs because of mesh distortion

issues at large strains. To capture large deformations in sensitive clay slope failures, an advanced FE modeling technique is required.

In the present study, in order to accommodate large deformations, FE analyses are performed using Abaqus/Explicit Version 6.14.2 FE software. The soil is modeled as an Eulerian material such that it can flow through the fixed mesh without causing any mesh distortion issue and can simulate a large deformation of failed soil in a landslide.

Numerical analyses are performed for large-scale submarine landslides. As mentioned above, many factors could trigger a submarine landslide. In the present study, two triggering factors are considered: (i) the formation of a weak zone through the sensitive clay layer, and (ii) earthquake loading. For the latter, the failure during the earthquake (co-seismic) and its continuation after the earthquake (post-quake) are simulated. Note that many studies showed a predominant post-quake failure as compared to co-seismic failure (Ambraseys and Srbulov 1995; Nadim and Kalsnes 1997; Dadson et al. 2004; Suito and Freymueller 2009; Zhuang et al. 2010).

The mechanisms of submarine landslides have been discussed in previous studies using the concept of shear band propagation. It has been shown that a relatively short initial slip surface—termed "shear band" in the present study—can cause a gigantic landslide (Puzrin and Germanovich 2005; Puzrin 2016). If the length of the initial shear band is greater than the critical length, the shear band can propagate catastrophically in the upslope and/or downslope directions. Although mild, varying seabed slope angles have been observed in the field. If the failure of a large slab of seabed sediment occurs in the steeper part of a submarine slope due to the formation of a failure plane parallel to the seabed, it could cause downslope progressive failure and upslope retrogressive failure. The displacement of a large failed soil block resulting from the steeper slope could create additional pressure on the soil where the seabed profile changes from steep to mild (or even flat).

7

This additional pressure could cause a ploughing type failure in the milder section of the seabed profile, as inferred from seabed mapping (Gee et al. 2006; Puzrin 2016; Puzrin et al. 2016). On the other hand, downslope movement of the failed soil mass reduces the support on upslope soil, which could cause retrogressive failure (Azizian and Popescu 2003; Martinez et al. 2005; Puzrin et al. 2016, 2017). A very limited number of numerical models are available in the literature to explain the spreading, ploughing, and run-out mechanisms for a varying seabed slope angle under different triggering conditions, as most of the previous studies have proposed analytical equations and criteria for idealized conditions. In this study, numerical simulations are performed using an advanced FE tool to explain these processes.

1.3   Objectives

The main purpose of this study is to simulate submarine slope failures that involve sensitive clays using an advanced numerical tool to explain possible mechanisms of spreading, ploughing, and run-out. Analyses are performed using Abaqus FE software, where the soil is modeled as an Eulerian material to simulate a large deformation. As the failure occurs very quickly, analyses are performed for an undrained loading condition. The following steps are taken to achieve this objective:

- Conduct FE simulation of submarine slope failure triggered by the existence of a weak zone in the seabed sediment. For the stress–strain behaviour of sensitive clay, implement a soil model considering the post-peak degradation of undrained shear strength including very low shear strength for a large strain.

- Conduct dynamic FE analyses by developing models with appropriate boundary and loading conditions, including the earthquake acceleration time history.

- Investigate progressive and retrogressive failure of slopes in a varying seabed profile and their relationship to spreading, ploughing, and run-out.

- Develop an FE model with the pseudostatic method and identify the similarities and differences between the failures simulated using pseudostatic and full dynamic analyses.

- Develop a simplified approach for modeling the co-seismic failure of a slope that could be used without conducting computationally expensive and complex dynamic analyses.

1.4   Outline of thesis

This thesis is organized into five chapters. The outline is as follows:

Chapter 1 explains the background, scope and objectives of the research.

Chapter 2 contains a literature review related to submarine landslides, including the effects of strain-softening behaviour of offshore sediments, mechanisms of failure, and numerical modeling.

Chapter 3 presents FE simulations of offshore slope failures triggered by a weak zone.

Chapter 4 describes the FE modeling of submarine slope failures triggered by an earthquake. Analyses are performed using earthquake acceleration time history (dynamic FE modeling) and pseudostatic loading.

Chapter 5 presents the conclusions of the study and some recommendations for future studies.

1.5 Contributions

The following are the main contributions:

- Explains the progressive and retrogressive failure mechanisms of submarine slopes due to weakening of a thin zone of soil that might result from gas hydrate dissociation and/or strain-softening of marine clays

- Explains the failure patterns (e.g., spreading, ploughing, and run-out) as observed in the field

- Proposes methods for modeling co-seismic and post-quake failure of offshore slopes.

CHAPTER 2

Literature Review

2.1 General

Submarine landslides occur in shallow to deep water depths through varying soils and seabed profiles. Submarine landslides can be a significant threat to offshore structures located in the areas from where the landslide initiates, and also, on the way the failed soil mass can travel over a large distance. Interest in the assessment of risks associated with submarine mass movements has increased with the increase in offshore oil and gas activities around the world. High-resolution bathymetry and profiler data collected during site investigations have identified the presence of weak layers in the seabed. Notably, the presence of a geotechnically weak soil layer has been identified as being one of the preconditions for the initiation of submarine mass movements (Norwegian Geotechnical Institute 1997; L'Heureux et al. 2012; Rodríguez-Ochoa et al. 2015; Bryn et al. 2003; Haflidason et al. 2003; Longva et al. 2003; Laberg et al. 2003; Lindberg et al. 2004; Laberg and Camerlenghi, 2008).

The initiation of a submarine landslide can occur due to a softened thin shear band in a strain-softening weaker material, which can cause catastrophic failure of an infinite slope. The strain-softening behaviour of a weak layer could cause a large deformation failure triggered by gas hydrate dissociation or an earthquake. Different numerical modeling techniques are available in the literature, but most of the techniques cannot explain the mechanisms of large deformable slope failures. The primary focus of the present research is to simulate large-deformation submarine landslides in sensitive clays through advanced finite-element analyses. The simulations are

performed in an undrained condition using shear strength reduction, dynamic, and pseudostatic methods.

The literature review presented in this chapter mainly focuses on submarine slope failures with sensitive clay layers having strain-softening behaviour. The chapter is divided into five sections. Section 2.2 primarily focuses on the history of submarine slope failures. The behaviour of weak sensitive clay layers and the failure mechanisms of submarine landslides are discussed in Sections 2.3 and 2.4, respectively. Finally, Section 2.5 discusses the submarine slope stability analyses using different methods.

2.2   Brief review of historical submarine landslides in offshore environments

Major submarine landslides in the past have involved massive mass movements of 4,000 – 5,000 km^3, and even up to 20,000 km^3 (Hampton et al. 1996; Azizian 2004). Submarine landslides are very frequent both in active and passive continental margins (Mienert et al. 2002; Leynaud et al. 2004), and these landslides may even cause devastating tsunamis (Frydman and Talesnick 1988; Puzrin 1996; Puzrin and Germanovich 2005). Continental slopes are generally steeper part of the margin, where the effects of gravity on the downslope sediments are high (Leynaud et al. 2004).

The presence of a weak soil layer and other external triggering factors are the main reasons for many submarine landslides. Among them, gas hydrate dissociation (Sultan et al. 2004; Bryn et al. 2005; Zhang et al. 2015), erosion (Lebuis et al. 1983; Quinn et al. 2007; Locat et al. 2008, 2013), and earthquake shaking (Locat and Lee 2002; Bardet et al. 2003; Wright and Rathje 2003; Biscontin et al. 2004; Rodríguez-Ochoa et al. 2015; Puzrin et al. 2016) are considered as the causes of many failures. Other common triggering factors can be rapid sedimentation, salt diapirism, sea level fluctuations, magma volcanoes, and over-steepening.

Historical evidence suggests that earthquakes are one of the most important external triggering factors for a submarine slope failure. The Grand Banks slope failure occurred due to an earthquake of magnitude 7.2 on November 18, 1929, at the southern edge of the Grand Banks, 280 km south of Newfoundland (Piper et al. 1999; Fine et al. 2005). The earthquake triggered a large (~ 150 km^3) underwater landslide, which produced a turbidity current of speeds of about 60 – 100 km/h, with the distance between the scar rim and the most distal deposit being more than 850 km (Piper et al. 1999; Canals et al. 2004). This slope failure affected many coastal communities, killing 28 people and breaking 12 telegraph cables (Fine et al. 2005).

A submarine landslide off Papua New Guinea (PNG) occurred on July 17, 1998, likely triggered by an earthquake magnitude of 7.0, representing one of the recent earthquake-induced submarine landslides. The landslide occurred 25 km from the coast near Aitape, PNG and caused a large tsunami with waves up to 15 m high, and killed more than 2,200 people (Kawata et al. 1999; Tappin et al. 1999; McSaveney et al. 2000).

The Gebra Slide, located on the Antarctic margin, may have been triggered by an earthquake. Its mass movement was about 20 km^3, with a slide scar of ~30 km long and ~12 km wide (Imbo et al. 2003; Canals et al. 2004). The Trænadjupet, Cape Fear, and Humboldt slides were also triggered by either one large or a series of smaller earthquakes (Embley 1980; Gardner et al. 1999; Laberg and Vorren 2000; Lee et al. 2002). Also, as noted in the previous chapter, the Storegga Slide was the result of a combination of earthquakes and gas hydrate dissociation.

The morphologies of most of the large continental submarine landslides indicate failures along 'weaker' sediment layers of particular low-strength properties (Masson et al. 2006; Locat et al. 2014a; Talling et al. 2014), and therefore, the presence of existing weak layers and external triggering forces can signify a possible landslide event. These external triggering forces not only

increase the driving force but also reduce the shear strength in a thin layer of sediment through strain-softening or by increase in excess pore water pressure, thereby creating a sliding surface in the form of a thin shear band. The thin shear band can propagate progressively and retrogressively along the slope, and can take the form of rotational or translational failure (ploughing, spreading, slab slide, and run-out) depending upon the slope gradients, seafloor morphology, and external triggering factors. In the present study, the mechanisms and triggering factors involved in the initiation of a submarine slope failure in sensitive clay and the forms of different failures are investigated using the concept of soil mechanics.

2.3 Behaviour of sensitive clay

The behaviour of sensitive clays in onshore environments has been investigated by many researchers (Tavenas et al. 1983; Thakur 2007). Compared to highly sensitive onshore clays in eastern Canada and Scandinavian countries, offshore marine sediments are relatively less sensitive. For example, during the Ormen Lange gas field development in the Norwegian Sea, a comprehensive geotechnical investigation was carried out. In the Storegga Slide areas, the soil profile consists of interbedded sensitive marine and/or glaciomarine clay sediments and relatively strong insensitive or slightly sensitive glacial clay layers (Kvalstad et al. 2005a, 2005b). Marine clays are generally normally or lightly overconsolidated and sensitive, and have high water content, a high plasticity index, and high clay content. Typical behaviour of marine clay and glacial debris is shown in Fig. 2.1(a). As shown, the shear strength decreases with shear strain (strain-softening). Moreover, the percentage of the decrease of strength is higher in marine clay than glacial debris.
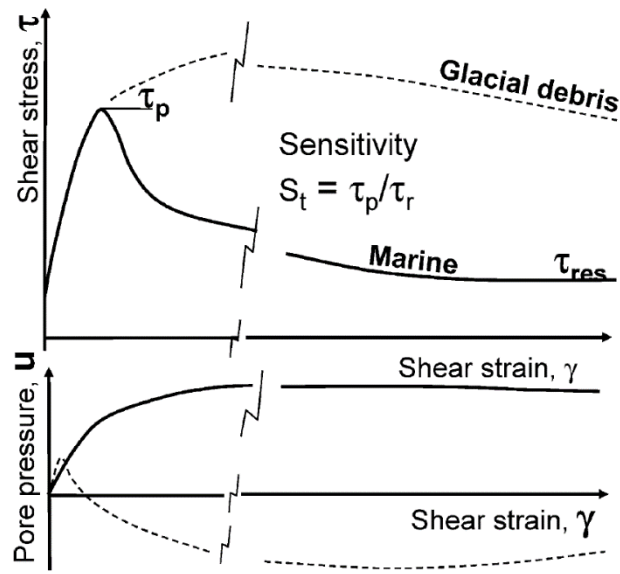
(a)
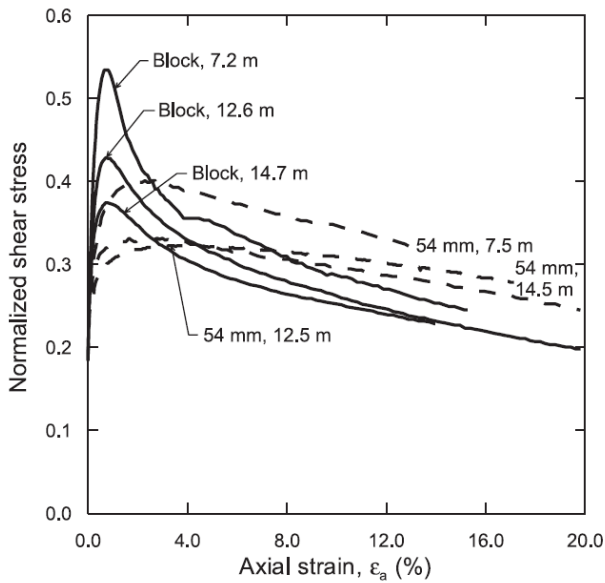
(b)
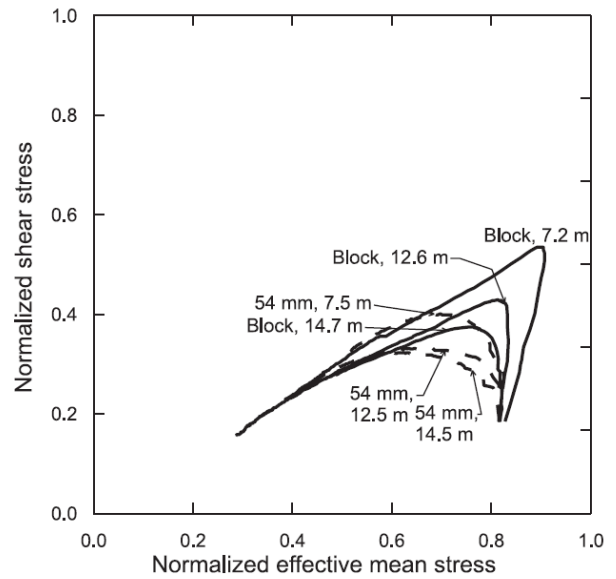
(c)

Figure 2.1: Behaviour of marine clay: (a) typical behaviour of marine and glacial debris (Kvalstad et al. 2005a); (b) and (c) behaviour of Onsøy clay ((Lunne et al. 2006)

Strength reduction with shearing was also found in other marine clays for different modes of shearing. For example, Figs. 2.1(b) and 2.1(c) show a significant loss of undrained shear strength for Onsøy clay in consolidated anisotropically undrained compression tests. As shown in Fig.

2.1(b), the triaxial tests could be continued only up to a certain strain level (maximum 20% in this case). However, the shear strain in the failure planes in a landslide is significantly higher than this value. Therefore, alternative tests, such as ring shear or cyclic T-bar tests, could be used for large-strain shear strength behaviour.

Dey et al. (2016) provided a detailed discussion on the degradation of undrained shear strength, including response at very large strains. They also used an exponential equation for modeling strain-softening, which has been also calibrated against the results of specially designed laboratory tests on sensitive clays conducted by Tavenas et al. (1983).

2.4   Submarine landslide failure mechanism

Different approaches have been used to understand the mechanisms of submarine landslides through strain-softening clay layers, and most of the studies concluded that the failure initiation could develop locally from a section of a weak zone and then propagate (Puzrin and Germanovich 2005; Dey et al. 2016a; Puzrin et al. 2016). The weak zone might have formed because of various reasons; however, gas hydrate dissociation and earthquakes have been considered as the major triggering factors of submarine landslides (Embley 1980; Lee et al. 1981; Lykousis 1991; Piper et al. 1999; Pauli et al. 2000; Sultan et al. 2003, 2004; Maslin et al. 2004; Fine et al. 2005; Nadim et al. 2007).

The presence of gas hydrates (ice-like substances) in the seabed may cause a submarine landslide when the hydrates dissociate and release natural gas bubbles due to a temperature increase or a pressure decrease (Whelan et al. 1977; Kvenvolden and McMenamin 1980; Hampton et al. 1982; Locat and Lee 2002). The release of natural gas degrades the shear strength of the sediments and

can cause slope failure. Similarly, earthquake motion could decrease the shear strength of a strain-softening layer if it generates plastic shear strains.

During gas hydrate dissociation and earthquake, a weak zone (called a "discontinuity" by Puzrin et al. 2004) experiences shear stress greater than the shear strength of the soil, and the stress is transferred into nearby soil elements. If the soil elements have strain-softening behaviour, the shear band will be propagated further. A shear band is a narrow zone where a significantly high plastic shear strain is localized (Gylland et al. 2014).

Palmer and Rice (1973) studied the progressive failure of overconsolidated London clay based on the concept of linear elastic fracture mechanics. Puzrin and Germanovich (2005) applied the fracture mechanics concept to submarine slope stability and distinguished progressive and catastrophic failures in infinite slopes. In a progressive failure, the propagation of a shear band is stable, while it is unstable in catastrophic failures once the length of the initial failure zone exceeds the critical length. In a catastrophic failure, when the initial shear band reaches the critical length, it develops partially softened process zones at both ends of the initial failure zone where the shear strength reduces from the peak to a residual value. The shear band propagates dynamically and can rupture the upward soil above the weak layer, and after rupturing the upward soil, it can cause active failure upslope and passive failure downslope.

Puzrin and Germanovich's (2005) approach does not explain the propagation of shear bands in stable parts of a slope. Puzrin et al. (2016) proposed improved shear band propagation criteria to identify different stages of a submarine landslide, including the propagation of a shear band in the stable parts.

The initiation of a submarine slope failure occurs due to external triggering factors, and even a thin zone with weaker material can produce a catastrophic failure in both the upslope and downslope regions (Puzrin et al. 2004, 2015; Puzrin and Germanovich 2005; Andresen and Jostad 2007; Viesca et al. 2008; Garagash and Germanovich 2012; Viesca and Rice 2012a; Zhang et al. 2015). Depending upon the location of the initial failure surface, the shear band can propagate upslope, downslope, or both upslope and downslope simultaneously (Dey 2015).

Puzrin et al. (2015, 2016) proposed some analytical equations and a framework for submarine spreading and ploughing failure criteria in the upslope and downslope directions, respectively. When the initial shear band develops slab failure, it produces active pressure upslope which causes a retrogressive spreading failure, and passive pressure downslope which causes progressive ploughing failure. Depending upon the accumulated failed soil mass downslope, it can also develop run-out. Figure 2.2 shows the typical modes of a slab-type slide, ploughing, spreading, and run-out during a submarine landslide. A slab-type slide represents the displacement of a failed soil slab which is structurally intact, tabular and non-disintegrative slope failure. A complete slab failure in the steeper part of a submarine slope could also cause progressive failure downslope and retrogressive failure upslope. During the progressive failure downslope, the accumulated soil near the toe of the slope develops additional pressure, which could cause ploughing failure, and depending on the height of the accumulated failed soil mass downslope, this could cause run-out. Similarly, the progressive failure downslope reduces the support on upslope soil, which leads to retrogressive failure and causes a spread failure.
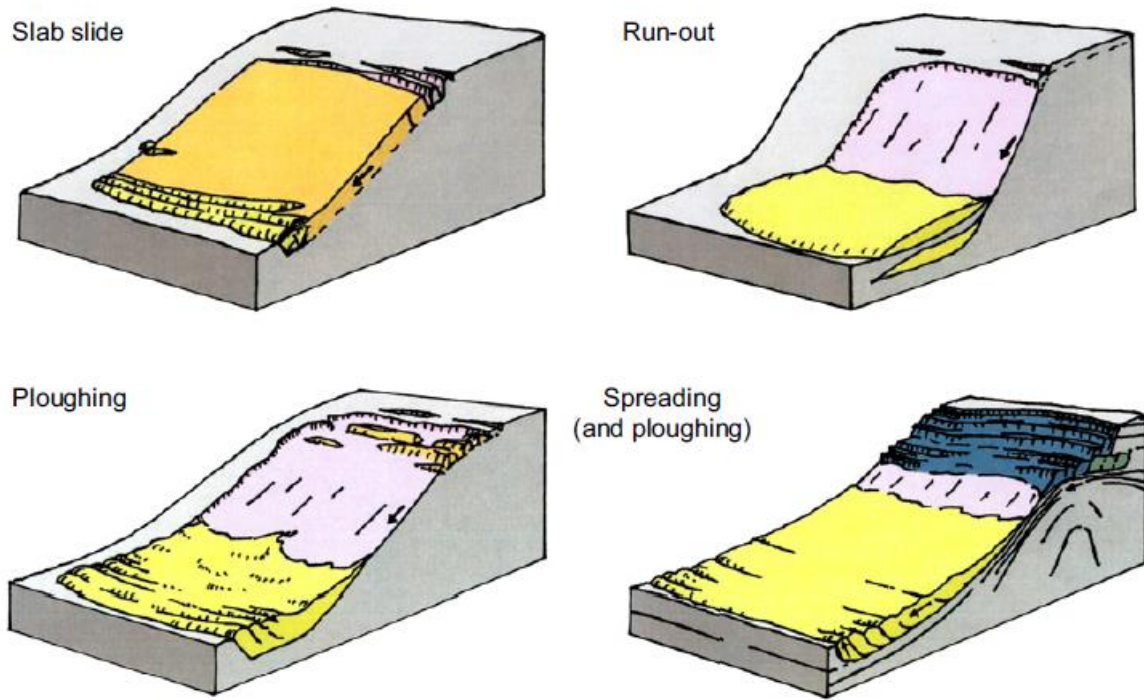
Figure 2.2: Typical failure modes of slab slide, ploughing, spreading, and run-out during a submarine landslide (after Puzrin et al. 2016)

An initial shear band in the marine sensitive clay layer is sufficient to cause a large deformation landslide. Fig. 2.3 shows the propagation of a shear band in a submarine landslide for a varying slope angle. The shear band propagates to both the upslope and downslope stable zones. Puzrin et al. (2016) explained spreading and ploughing failures using block failure mechanisms, and proposed analytical equations and criteria for the formation of horsts and grabens. Note that horst and graben-type failure mechanisms have also been reported in other studies (Bryn et al. 2005; Gauer et al. 2005; Kvalstad et al. 2005a; Micallef et al. 2007; Wang et al. 2013). The failure patterns can be different depending on the geometry and soil properties. The analytical equations proposed by Puzrin et al. (2016) cannot be used for modeling different types of progressive and retrogressive failure properly, but they can be modeled using advanced FE techniques such as the one presented in the present study.
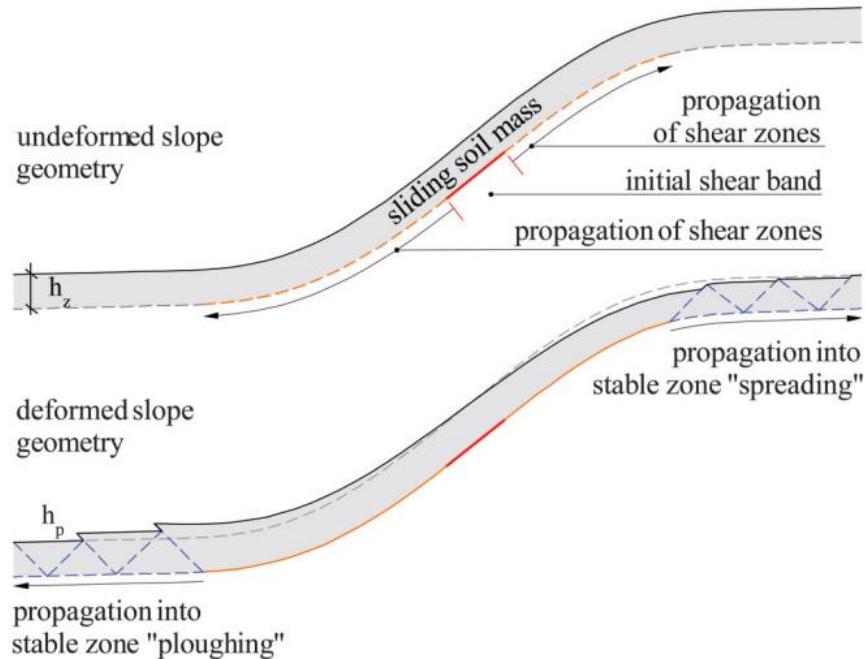
Figure 2.3: Submarine landslide processes (Puzrin 2016)

2.5 Submarine slope stability analyses

2.5.1 Limit equilibrium method

The limit equilibrium method is one of the widely used methods for slope stability analysis, and has been used for the stability analysis of submarine slopes for both static and dynamic loading conditions. As the seabed slope mild, most of the analyses have been performed for infinite slopes (Mello and Pratson 1999; Dimakis et al. 2000; Leynaud et al. 2004; Kvalstad et al. 2005b; Nixon and Grozic 2007). For dynamic loading conditions, in addition to static force, a pseudostatic horizontal force of $k_h W$ is considered, where k_h ($= a_h/g$) is the pseudostatic earthquake coefficient, W is weight of the failed soil mass, a_h is the horizontal ground acceleration, and g is the gravitational acceleration. The guidelines for the selection of a pseudostatic coefficient (k_h) are shown in Table 2.1.

Table 2.1: Selection of a pseudostatic coefficient

k_h	Description	References
0.1	Severe earthquakes	Terzaghi 1950; Seed 1979; Corps of Engineers 1982; California Division of Mines and Geology 1997; Melo and Sharma 2004; Ghobrial et al. 2015
0.1 – 0.15	$M_M = 6.5 – 8.25$, displacement of earth dams < 1.0 m	
0.2	Violent earthquakes	
0.5	Catastrophic earthquakes	
$0.5k_m/g$	$F_s > 1$, Strength reduction of 20%, displacement of earth dams <1 m	Hynes-Griffin and Franklin 1984
$0.65k_m/g$	For intermediate slide mass	Matsuo et al. 1984; Taniguchi and Sasaki 1985; Melo and Sharma 2004
$(0.33$ to $0.5)k_m/g$	$F_s > 1$	Marcuson 1981; Marcuson and Franklin 1983
	A chart for k_h/k_m as a function earthquake magnitude M	Pyke 1991
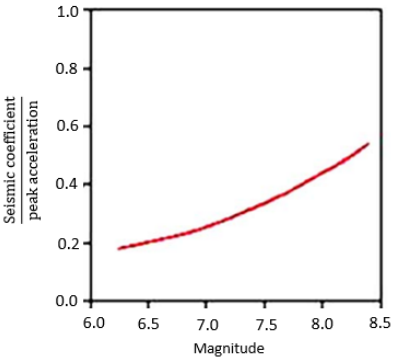
The factor of safety (F_s) for dynamic loading condition can be calculated as the ratio between resistance and driving force that include both static and dynamic components. The slope is stable if $F_s > 1$. The value of k_h that gives a factor of safety equal to one is commonly known as the critical seismic coefficient, k_c ($= a_c/g$) (Sarma 1975; Li 2007; Jibson 2011; Nadi et al. 2014). Ground displacement occurs when the horizontal acceleration exceeds the critical acceleration (a_c). While the F_s can be calculated using the limit equilibrium method, it cannot quantify the displacement of the slope. Moreover, the limit equilibrium method significantly overestimates the F_s when the failure involves shear band propagation, as happens in sensitive clay slopes (Bernander 2000; Locat et al. 2011; Dey et al. 2016b).

2.5.2 Sliding block methods

Sliding block methods have been developed to estimate the displacement of a failed soil block due to an earthquake. In Newmark's (1965) sliding block approach, the soil mass is considered as a rigid block, and lateral displacement takes place when the ground acceleration exceeds the critical acceleration. For a given acceleration time history, the displacement of a sliding block can be calculated by integrating twice with time for those portion of the acceleration–time curve above the critical acceleration. After Newmark (1965), several authors proposed different empirical equations and charts to calculate earthquake-induced displacements. As summarized in Table 2.2, the main parameters required for displacement calculations are: the maximum seismic coefficient (k_m), critical seismic coefficient (k_c), maximum velocity (v_m), and predominant period of the acceleration (T). Cai and Bathurst (1996) categorized sliding block methods into two main groups: one group used k_m and v_m, and the other group proposed equations bases on k_m and T. In addition, the root mean square of acceleration (A_{RMS}), duration for which acceleration is greater than yield acceleration ((Dur)$_{ac}$) and spectral acceleration with 5% damping at 1 s (S_a) have been used in

some studies (Watson-Lamprey and Abrahamson 2006). Most of the proposed methods are based on permanent displacement of dams and embankments (e.g., Makdisi and Seed 1977; Yegian et al. 1991) and landslides in natural slopes (Wilson and Keefer 1983; Pradel et al. 2005). However, none of these methods can capture large displacements of failed soil in sensitive clay slopes with strain-softening soil behaviour. Therefore, an advanced technique is required to model this process.

Table 2.2: Parameters required in predictive models for permanent displacement

Reference	Parameters	Main Applications
Newmark 1965	k_m, v_m, k_c	Dam or embankment
Sarma 1975	k_m, k_c, T, α	Earth dam or embankment
Franklin and Chang 1977	v_m, k_m, k_c	Earth embankments
Makdisi and Seed 1977	k_m, k_c, T	Earth slopes
Richards and Elms 1979	v_m, k_m, k_c	Gravity wall
Wong 1982	v_m, k_m, k_c	Gravity retaining walls
Nadim and Whitman 1983	v_m, k_m, k_c	Retaining wall
Whitman and Liao 1985	v_m, k_m, k_c	Gravity retaining wall
Hynes-Griffin and Franklin 1984	k_m, k_c	Earth dams
Ambraseys and Menu 1988	k_m, k_c	Ground and slopes
Yegian et al. 1991	k_m, k_c, T, N_{eq}	Earth dams and embankments
Cai and Bathurst 1996	v_m, k_m, k_c and $\quad k_m, k_c, T, \alpha$	Earth structures
Watson-Lamprey and Abrahamson 2006	k_m, k_c, Dur_{ac}, $S_a(T = 1 \text{ s}), A_{RMS}$	Earth slopes
Jibson 2007	k_m, k_c and $\quad k_m, k_c, M_M$ and $\quad I_a, k_c$ and $\quad I_a, k_m, k_c$	Natural slopes
Saygili and Rathje 2008	v_m, k_m, k_c	Natural slopes

2.5.3 Finite-element methods

While the limit equilibrium methods are widely used in industry, finite-element methods have also been used by many researchers for slope stability analysis. In a state-of-the-art paper, Duncan (1996) discussed the advantages of finite-element methods over limit equilibrium methods for slope stability analysis. One of the main advantages of FE methods is that a priori location of the failure plane is not required to be defined in FE analysis, and the computer program identifies the highly stressed zone where failure occurs. Moreover, the progressive formation of the failure plane can be simulated by FE analysis.

Most of the FE slope stability analyses available in the literature have been conducted using FE programs developed on the Lagrangian framework (Matsui and San 1992; Ugai and Leshchinsky 1995; Griffiths and Marquez 2007; Nian et al. 2012; Ho 2014). Analyses are performed for homogenous and layered soil profiles, however limited to small strains level.

The large deformation of sensitive clay slope failures cannot be modeled using the Lagrangian FE program because of excessive mesh distortion and convergence issues. To overcome these issues, some advanced numerical techniques have also been used, for example, the Arbitrary Lagrangian–Eulerian (ALE) formulation (Nazem et al. 2008, 2009), Smooth Particle Hydrodynamics Method (SPH) (Monaghan 1988), Particle Finite Element Method (PFEM) (Idelsohn et al. 2004; Oñate et al. 2004), and Material Point Method (MPM) (Sulsky et al. 1995). An Eulerian-based finite-element formulation can overcome mesh distortion issues in large deformation problems. The pure Eulerian approach and the Coupled Eulerian–Lagrangian (CEL) approach (when highly deformable materials interact with less deformable Lagrangian body) have been used in previous studies (Dey et al. 2015; Trapper et al. 2015; Dey et al. 2016a). Further details on mathematical formulations of the Eulerian FE and CEL approach are available in Benson (1992). Soga et al.

(2016) provided a review of large deformation numerical modeling techniques available in the literature.

Dey et al. (2016a) conducted large deformation finite-element analysis of an infinite offshore slope by modeling the soil as an Eulerian material. They modeled a 1.2 km-long submarine slope having a thin weak strain-softening clay layer at a depth of 19 m below a glacial clay layer. Two strong soil blocks existed at the ends of the slopes. The failure of the slope was triggered by reducing the undrained shear strength of soil in a segment of the weak layer near the middle of the domain. Figure 2.4 shows the progressive formation of the shear band with time. The failure created a V- and Λ-shape wedge failure both in the upslope and downslope areas. A considerable heave occurs downslope, while significant settlement occurs in the upslope area.
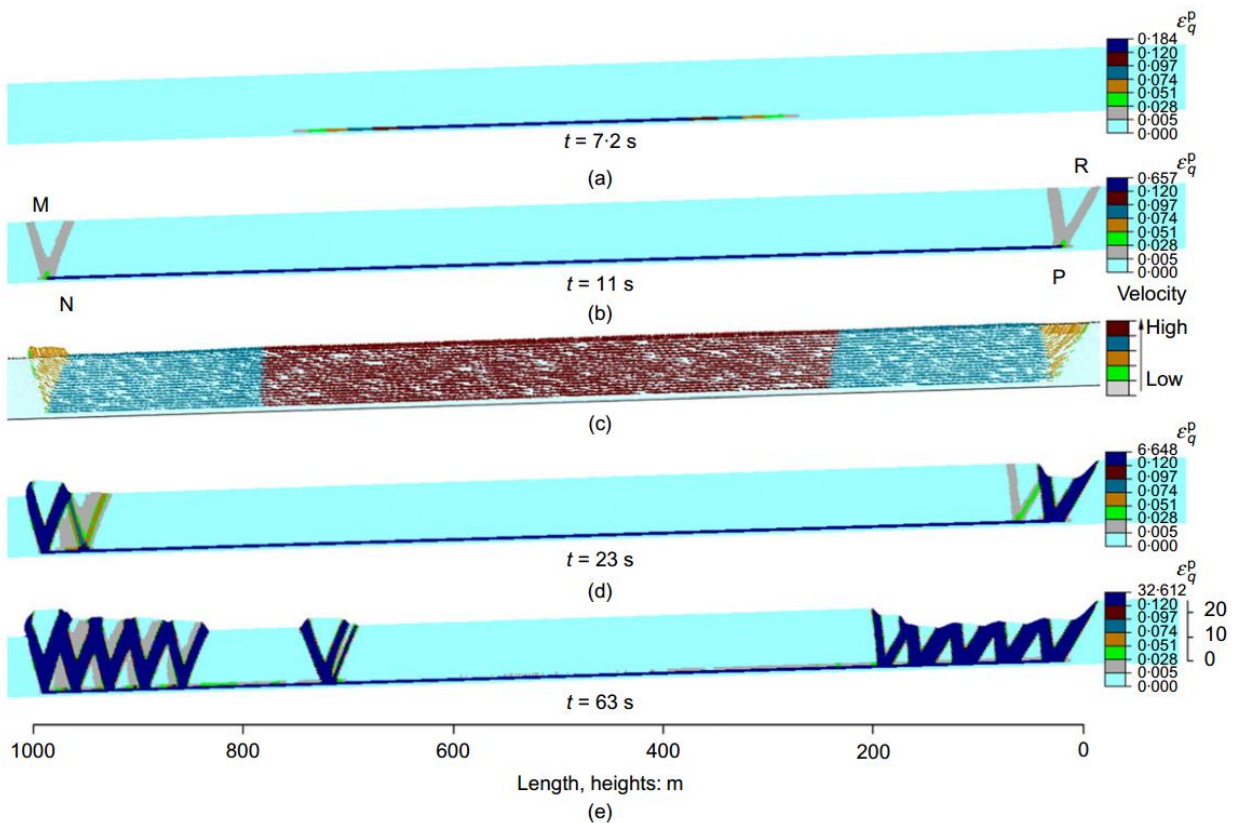
Figure 2.4: Development of failure surface in a mild submarine slope (Dey et al. 2016a)

2.5.3.1 Modeling of earthquake-induced submarine landslides

As mentioned in previous sections, many offshore slope failures are triggered by earthquakes. FE modeling of earthquake-triggered offshore slope failure is very limited; however, a considerable number of FE slope stability analyses for earthquake loading have been performed for onshore slopes. Two approaches are commonly used for earthquake-triggered slope stability analysis. Firstly, the earthquake effects are calculated in the soil elements in the form of horizontal acceleration, based on a pseudostatic coefficient. Secondly, a complete dynamic analysis is performed where the earthquake loading is given as an acceleration time history.

A considerable number of studies have used the first approach to FE modeling, where the horizontal acceleration of the soil elements increases until the failure of the slope (Woodward and Griffiths 1996; Loukidis et al. 2003; Sarma and Tan 2008; Khosravi et al. 2013). However, pseudostatic slope stability analysis will provide reasonable results if the degradation of the shear strength is low (Bray and Travasarou 2007, 2009; Puzrin et al. 2016). For example, Kramer (1996) suggested that the pseudostatic slope stability method is applicable for shear strength reduction of up to 15%.

Based on the second approach, Kourkoulis et al. (2010) presented FE simulations of earthquake-triggered landslides and their effects on foundations on the upslope areas. The strain-softening behaviour of soil is modeled by decreasing the shear strength parameters (cohesion and friction angle) linearly with plastic shear strain. A horizontal seismic excitation (the Kobe 1995 earthquake) is given at the base of the model, which caused the progressive failure of the slope. Dynamic slope stability analyses based on Lagrangian-based FE methods have also been presented by number of researchers (e.g., Chen et al. 2001, 2013; Nichol et al. 2002; Ghosh and Madabhushi 2003; Leynaud et al. 2004; Azizian and Popescu 2006; Sigarán-Loría et al. 2007;Wang et al. 2009;

Taiebat and Kaynia 2010; Kourkoulis et al. 2010). Most of the FE analyses have been focused on dams, reinforced soil walls, and natural slopes.

Azizian (2004) developed 2D and 3D retrogressive submarine slope failure models using a multi-yield surface plasticity model to simulate seismic triggering of landslides in sand. Rodríguez-Ochoa et al. (2015) showed the importance of a weak layer for failure initiation in a submarine slope during a seismic event based on numerical simulations using PLAXIS 2D software. They showed that the displacements in the weak layer model, particularly above the weak layer horizon, are higher than in the slope model with no weak layer. They also discussed the influence of a weak layer of sensitive clay.

2.6   Summary

The literature review shows research that a large-scale submarine landslide can be initiated locally in a weak soil layer. The failure surfaces then develop progressively in the form of shear band propagation, causing global failure of a large number of soil blocks. This type of failure cannot be explained using the limit equilibrium methods or typical Lagrangian-based FE modeling because of the large deformation of failed soil blocks. In addition, a seabed profile could have varying slope angle. In many cases, failure initiates from a steep slope and then propagates in the stable upslope and downslope areas, resulting in widespread mass movement.

Two approaches can be used for the FE modeling of slope failures triggered by an earthquake. Full dynamic modeling of a slope, considering an acceleration–time history, is more challenging than with pseudostatic analysis. A simplified approach might be therefore used to define the earthquake effect because the post-quake deformation is significantly larger than co-seismic displacement, as reported from some onshore histories.

CHAPTER 3

Finite-Element Modeling of Progressive and Retrogressive Failure of Submarine Slopes for Varying Angle of Inclination

3.1 General

A submarine landslide might be initiated from the steeper part of the seabed profile and then extend over the less-sloped areas. The initiation of failure due to existence of a weak layer is modeled in this chapter. This chapter has been published as Roy and Hawlader (2017) in the 70th Canadian Geotechnical Conference.

3.2 Introduction

Submarine landslides are one of the major concerns in offshore oil and gas development activities. Offshore slopes are typically very mild (<10°) (Hadj-Hamou and Kavazanjian 1985); however, the occurrence of many large-scale landslides has been reported—for example, the 1929 Grand Banks Slide in offshore Newfoundland and the Storegga Slide in offshore Norway (Piper and Aksu 1987; Piper et al. 1999; Haflidason et al. 2005; Kvalstad et al. 2005a). Based on post-slide investigations, a number of hypotheses or conceptual models have been proposed to explain the dynamics of such large-scale landslides. Among the different triggering factors identified in the past, the presence of weak strain-softening clay layers has been considered as one of the primary causes of many landslides (Dan et al. 2007; Sultan et al. 2010; L'Heureux et al. 2012; Locat et al. 2014b).

Generally, the seabed slope angle (β) is not constant over a large distance. Therefore, it has been assumed that a failure might be initiated from the steeper part of a slope and then propagate to

28

more stable zones both in the upslope and downslope directions, where β is smaller than in the steeper section, or even zero.

Starting from a relatively small segment of an initially weakened zone, which might develop due to excess pore water pressure generation and/or gas hydrate dissociation, the propagation of the failure plane over a wide area can be explained using the concept of shear band propagation —the zone of highly localized plastic shear strain (Puzrin and Germanovich 2005; Puzrin et al. 2016). Shear band propagation occurs only when the soil has strain-softening behaviour. Field evidence suggests that in many cases, slab failure occurs due to the formation of a long shear band (i.e., failure plane) almost parallel to the slope.

A slab failure in the steeper part of a submarine slope could also cause progressive failure in the more stable zones around it. If the failed soil mass in the steeper zone moves a sufficiently large distance, that could reduce support on the existing soil in the upslope stable zone, which could cause a spreading-type failure (Puzrin et al. 2016). One the other hand, the accumulation of soil near the toe of the slope could create additional pressure on the soil in the stable zone, which could cause ploughing (Puzrin 2016; Puzrin et al. 2017). In addition, if a large volume of soil accumulates in the downslope stable zone, it might displace over the seabed (i.e., run-out occurs).

Using the concept of shear band propagation, Puzrin and his co-workers developed analytical solutions to explain the mechanisms of slab failure, spreading, ploughing, and run-out for simplified submarine slope geometries (Puzrin et al. 2017). These studies also provide criteria for initiation of the above-mentioned failures. However, the mechanisms of these types of failure could be better explained using advanced numerical tools.

The limit equilibrium method (LEM) is commonly used to assess the stability of a slope. However, the LEM cannot explain the progressive failure of a slope. The finite-element (FE) method has been used by many researchers and shows the advantages over the LEM (Duncan 1996). However, the traditional FE technique developed in the Lagrangian framework cannot be used for this type of large-scale submarine landslide analysis because the failed soil mass displaces over a large distance and extremely large strains are generated in the shear bands, which causes numerical instability due to mesh distortion. Dey et al. (2015) provided a detailed discussion on the numerical modeling of large deformation slope stability problems.

The objective of the present study is to conduct large-deformation FE modeling of submarine slopes with clay layers having strain-softening behaviour. The mechanisms of failure and their extent are examined. Some of the conditions required for different types of progressive failure in the stable zones, such as spreading, ploughing, distributed shear surface formation, and run-out, are identified.

3.3   Problem definition

Figure 3.1 shows the geometry of the slope modeled in the present study. The length of the model (L) is 1,500 m. The middle part of the model has a steep slope ($\beta_1 = 10°$), while the left and right stable sides of the steep slope are inclined at β_2 ($<\beta_1$) and β_3 ($<\beta_1$), respectively. Analysis is also performed for $\beta_2 = \beta_3 = 0$.
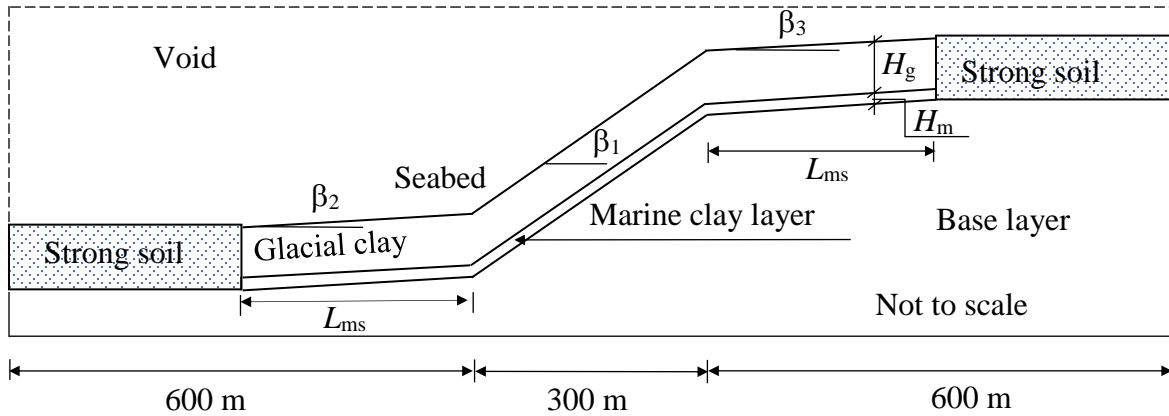
Figure 3.1: Geometry of the slope used in the FE analysis

The seabed profile contains a glacial clay layer of thickness H_g followed by a marine clay layer of thickness H_m. The base layer below the marine clay layer is considered as a strong soil and is modelled as an elastic material. The base layer does not have a significant effect on the failure of the slope. The length of the marine clay layer in the stable zone, measured from the toe or crest of the steep slope, is L_{ms}.

The geometry considered in this study is similar to an idealized section of the Palaeo-landslide area of the Caspian Sea (Gray et al. 2015; Puzrin et al. 2016). Analyses are performed for four cases, as shown in Table 3.1. In all the analyses, $\beta_1 = 0°$ is used. The left and right boundaries are placed at a sufficiently large distance from the steep section such that the failure is not affected by these boundaries. The analyses are performed for an undrained loading condition.

Table 3.1: Geometry of different cases used in the FE analysis

Case	H_g (m)	H_m (m)	β_2	β_3	L_{ms} (m)
I	20	1	0°	0°	300
II	15	6	0°	0°	300
III	20	1	5°	5°	300
IV	20	1	5°	5°	600

3.4   Finite-element modeling

Abaqus 6.14.2 FE software is used in the present FE analysis. The soil is modeled as an Eulerian material. One of the main advantages of this type of modeling is that the Eulerian material (soil) flows through the fixed mesh, and therefore numerical issues related to mesh distortion are not encountered. Further details of the mathematical formulations and its applications for slope stability problems are available in previous studies (Benson and Okazawa 2004; Dey et al. 2015, 2016a, 2016b; Trapper et al. 2015).

Abaqus CEL allows only three-dimensional modelling. Therefore, to simulate a plane strain condition, the analysis is performed with only one element length in the out-of-plane direction. Cubical elements having dimensions of 0.5 m are used. The soil is modeled as an Eulerian material using the EC3D8R elements in Abaqus, which are eight-node linear brick elements with reduced integration and hourglass control. A void space is created above the seabed to accommodate the displaced soil mass, and the Eulerian volume fraction (EVF) tool available in Abaqus is used to create the soil and voids for the initial condition.

Zero-velocity boundary conditions are applied along the bottom and all vertical faces, which implies no movement of soil particles next to these boundaries. No boundary condition is applied along the soil–void interface such that soil can move into the void space when needed. The von Mises criterion is adopted in this study.

The numerical analysis consists of three steps. First, in the geostatic step, the gravity load is applied in 2 s to bring the soil to an in-situ stress condition. As will be shown later, the slope is stable under the gravity load. In the second step, a weak zone is created at the middle of the steep slope in the marine clay layer by reducing s_u linearly from the peak value (s_{up}) at t = 2 s to the residual value (s_{uR}) at t = 4–7s. Previous studies have shown that a catastrophic failure is triggered only if the length of the weak zone exceeds a critical length (L_{cr}) (Puzrin and Germanovich 2005; Dey et al. 2016b). Based on those analytical studies and for the soil parameters used in the present study, L_{cr} is calculated. In order to trigger the failure, the length of the weak zone created in this step is greater than L_{cr}. Finally, in the third step, the analysis is continued until t = 50 s without any change in loading or soil properties by the user.

3.5   Undrained shear strength of soil

The strength–deformation behaviour used in the present study is shown in Fig. 3.2. The line oa represents the elastic behaviour, which is defined using the undrained Young's modulus and Poisson's ratio. The mobilized undrained shear strengths (s_u) of the glacial and marine clay layers are defined as a function of accumulated plastic shear strain and sensitivity in Eq. (3.1). A detailed discussion of sensitive clay behaviour and the use of the following exponential function is available in Dey et al. (2016a).
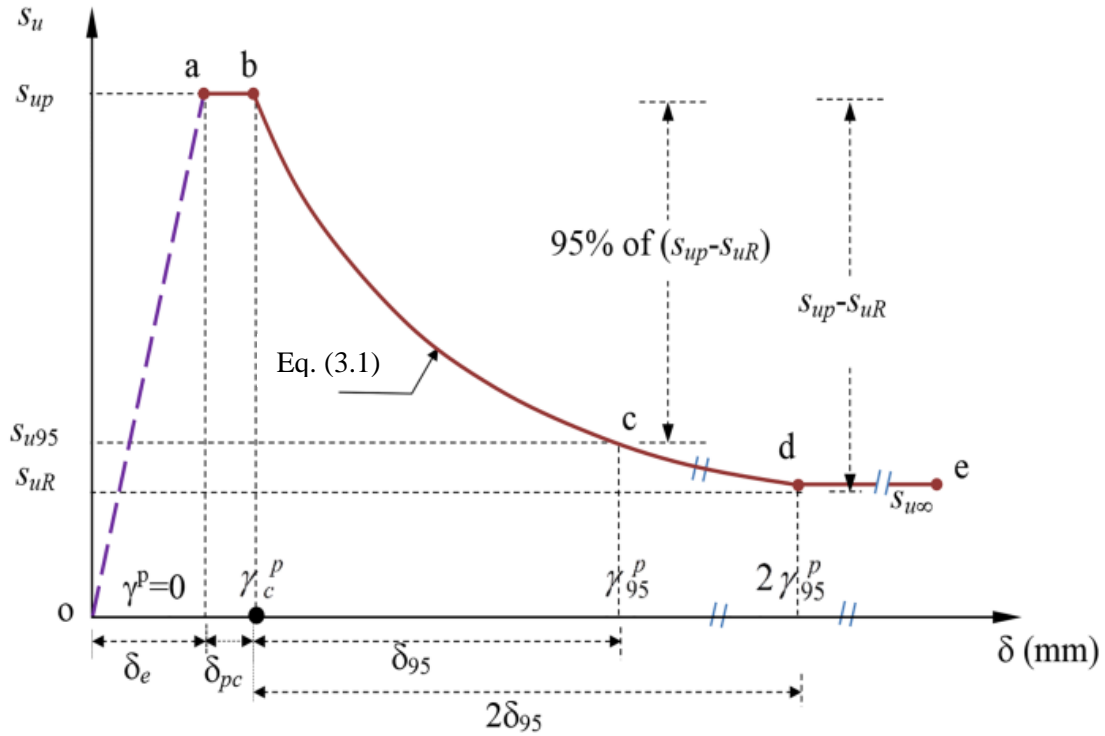
Figure 3.2: Strength-deformation behaviour used in the FE modelling (after Dey et al. 2016a)

$$s_u = \left[\frac{1}{S_t} + \left(1 - \frac{1}{S_t} \right) e^{-3\delta/\delta_{95}} \right] s_{up} \qquad (3.1)$$

where s_u is the mobilized undrained shear strength at displacement δ; S_t is the sensitivity of the soil; $\delta = \delta_{total} - \delta_p$ where δ_p is the displacement required to attain the peak undrained shear strength (s_{up}), s_{uR} is the residual shear strength that mobilizes at very large δ, and δ_{95} is the value of δ at which the undrained shear strength of the soil is reduced by 95% of (s_{up}-s_{uR}). Equation [3.1] is a modified form of a strength degradation equation proposed by Einav and Randolph (2005) but in terms of displacement. If the shearing occurs through only one row of elements, the plastic shear strain (γ^p) can be related to the finite-element thickness (t_{FE}) as $\gamma^p = \delta/t_{FE}$, assuming a simple shear condition.

The geotechnical parameters used in the FE analyses are listed in Table 3.2. These parameters have been estimated based on the typical geotechnical properties of offshore sediments and sensitive clays reported in previous studies (Tavenas et al. 1983; Stark and Contreras 1996; Gauer et al. 2005; Kvalstad et al. 2005a, 2005b; Lunne and Andersen 2007; Thakur 2007; Quinn 2009). In general, marine clays have a high clay content (45–65%), plasticity index (PI>25%), and sensitivity (3–6) as compared to glacial clay having a clay content of about 30–40%, PI of 12 to 25%, and sensitivity (1.5–3.0).

Table 3.2: Parameters used in the finite-element modelling

Parameters	Glacial Clay layer	Marine clay layer	Base & strong layers
Undrained Young's modulus, E_u: MPa	30	15	200
Poisson's ratio, v_u	0.495	0.495	0.495
Peak undrained shear strength, s_{up}: kPa	37.5	33.5	-
Plastic shear displacement for initiation of softening, δ_{pc}: mm	3	3	-
Plastic shear displacement for 95% degradation of soil strength, δ_{95}: mm	90	90	-
Sensitivity, S_t	3	6	-
Submerged unit weight of soil, γ': kN/m^3	10	8	11

3.6 Finite-element results

The process of failure of the slope is examined based on the formation of shear bands—the zone of localized plastic shear strain PEEQVAVG obtained from Abaqus. Note that PEEQVAVG is related to the commonly used plastic shear strain γ^p $(= \int_0^t \sqrt{\frac{3}{2}\left(\dot{\epsilon}_{ij}^p \dot{\epsilon}_{ij}^p dt\right)}$), where $\dot{\epsilon}_{ij}^p$ is the plastic deviatoric strain rate tensor as $\gamma^p = \sqrt{3}$PEEQVAVG. When PEEQVAVG > 0, the soil element reaches the yield strength and plastic deformation occurs.

3.6.1 Case-I

Figure 3.3 shows the failure of the slope for Case-I. Note that at the end of the geostatic step ($t =$ 2 s), no plastic strain develops in the slope, which implies that the slope is stable under in-situ stress. In the second step, a weak zone is created in the marine clay layer at the middle of the slope by reducing s_u from s_{up} to s_{uR}. Because of this weak zone, a shear band propagates parallel to the slope, as shown in Fig. 3.3(a). At this stage, the shear stress parallel to the slope due to the gravitational load in this zone is greater than the shear strength of the soil (s_{up}). The propagation of shear band AB in Fig. 3.3(a) occurs very quickly. In reality, this propagation causes catastrophic failure (Puzrin 2016), although in the FE simulation it has been done over a finite time period. The continuation of shear band formation in the third step is shown in Figs. 3.3(b) and 3.3(d).

Although the loading or boundary conditions are not changed by the user, the self-propagation of shear bands continues over this period, resulting in the formation of a number of failure blocks. After reaching the end of the slope, two curved failure planes form at the ends (AC and BD), resulting in global failure of a long slab (CABD). With time, two inclined failure planes also form at the ends (AE, BF), which results in the formation of two graben-type wedges (CAE and FBD).
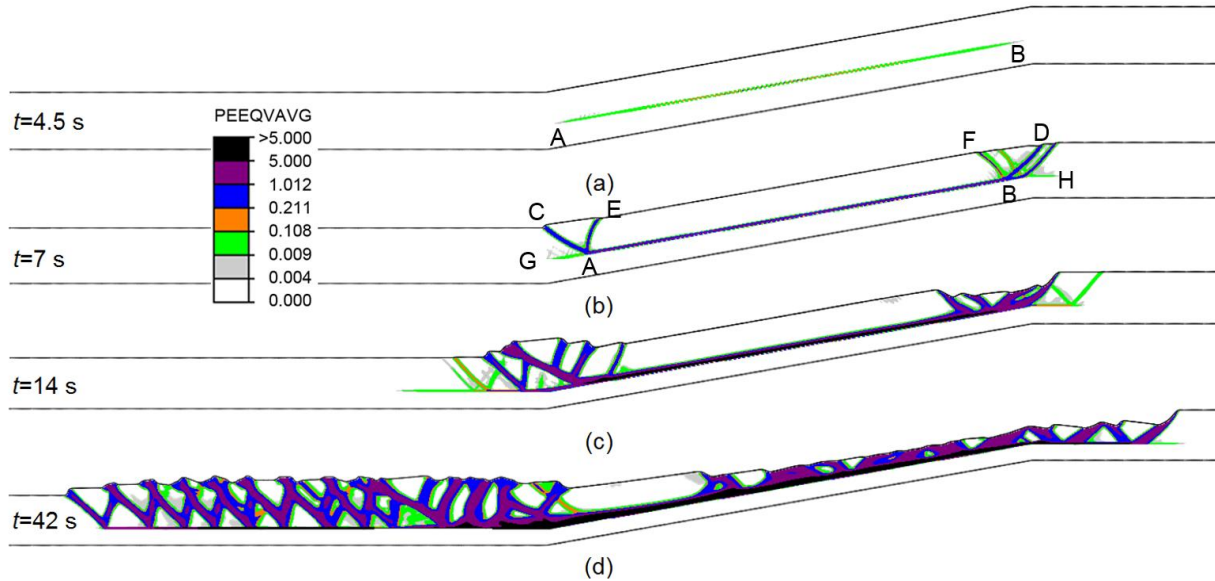
Figure 3.3: Formation of shear bands in Case-I

The failure of the slope does not stop after the slab failure and formation of two grabens in the sloped area. The horizontal propagation of two additional shear bands occurs with time: one downslope (AG) and one upslope (BH). This is because of the downslope movement of the failed soil mass CABD, which creates an additional load downslope (left side of point A) due to accumulation of soil at the toe. On the other hand, the displacement of the soil mass CABD causes a reduction of support on the soil in the right side of B (active loading). With time, the horizontal shear band BH propagates further right and a number of inclined shear bands form, resulting in formation of Λ-shaped horst and V-shaped grabens. This type of failure is known as "spreads," and is also commonly observed in sensitive clay slope failures near river banks triggered by toe erosion that reduces support on the remaining soil (Locat et al. 2011; Dey et al. 2015).

In the downslope areas, the increase in horizontal load resulting from the accumulated soil (passive loading) causes the propagation of the horizontal shear band AG. Similar to the upslope area, a number of horsts and grabens form in this area. This type of failure is known as "ploughing."

It is to be noted that the formation of horsts and grabens occurs by the progressive development of shear bands where the force increases or decreases gradually, and in this case it is due to displacement of the failed soil block. Progressive shear band propagation is different from catastrophic shear band propagation (e.g., the formation of AB in Fig. 3.3(a)), where the shear band propagates under constant load—constant shear stress along the shear band, AB in this case (Puzrin et al. 2016).

Onshore, upslope spreading and downslope progressive failures have been observed in many situations as separate phenomena. For example, toe erosion near a river bank can cause spreading (Locat et al. 2008), and upslope loading could cause downslope progressive failure or ploughing (Bernander 2000). However, offshore, both phenomena can be observed in the same slope.

Significantly large strains develop in the shear bands (Fig. 3.3(d)), and therefore this type of progressive failure and shear band formation cannot be simulated using typical FE methods developed in a Lagrangian framework for small strain analysis because of numerical issues related to mesh distortion. However, as the mesh remains fixed in the CEL approach, as used in the present study, numerical issues due to mesh distortion are completely avoided, and large displacements of failed soil blocks, together with the accumulation of significantly high strains in the shear bands, can be successfully simulated. No significant change in shear strain in the shear bands or formation of additional shear bands occurs after $t = 35$ s, which implies that the failed soil blocks come to an equilibrium at the end of the analysis.

The extent of failure in the upslope area due to spread is 91 m, which measures the distance between the crest of the slope before the initiation of failure (e.g., at the end of geostatic step) to the location where the last inclined shear band intersects the seabed. Similarly, the extent of downslope ploughing—the distance from the toe of the slope to the point where the last inclined

failure plane reaches the seabed— is 295 m. Figure 3.3(d) also shows a significant reduction of the thickness of the failed soil slab from the initial state (Fig. 3.3(a)), especially near the crest.

The maximum height of accumulated soil due to ploughing from the stable seabed is ~11 m. Note that when the height of the accumulated soil is sufficiently large, it might fail again, resulting in run-out under some favourable conditions (e.g., low shear strength of accumulated material and/or inclined downslope area); however, that did not happen in this simulation. On the other hand, the maximum settlement of horst and grabens in the upslope area, measured from the initial horizontal seabed profile, is 10 m, which occurs near the crest of the slope.

Whether a slab failure in the steeper part could cause upslope spreading and downslope ploughing depends on the geometry of the slope and the soil properties. Puzrin (2016) discussed the ploughing in a downslope area of a seabed in an Azerbaijani sector of the south Caspian Sea, located at 130 km to the southeast of Baku in water depths of 95–435 m. Based on shear band propagation criteria, Puzrin and his co-workers developed analytical solutions for the initiation of spreading, ploughing, and run-outs (Puzrin et al. 2016). The present FE analysis could also simulate the elasto-plastic deformation of the failed soil mass during the process of failure.

3.6.2 Case-II

Here, the effect of thickness of the marine sensitive clay layer is examined. In this case, the thickness of the marine clay layer is 6 m; however, the total thickness of the soil above the base layer (i.e., glacial plus marine clay layer) is the same as for Case-I ($15.0 + 6.0 = 21.0$ m). Except for this change in marine clay layer thickness, all the other conditions, including geotechnical properties, are the same as for Case-I.
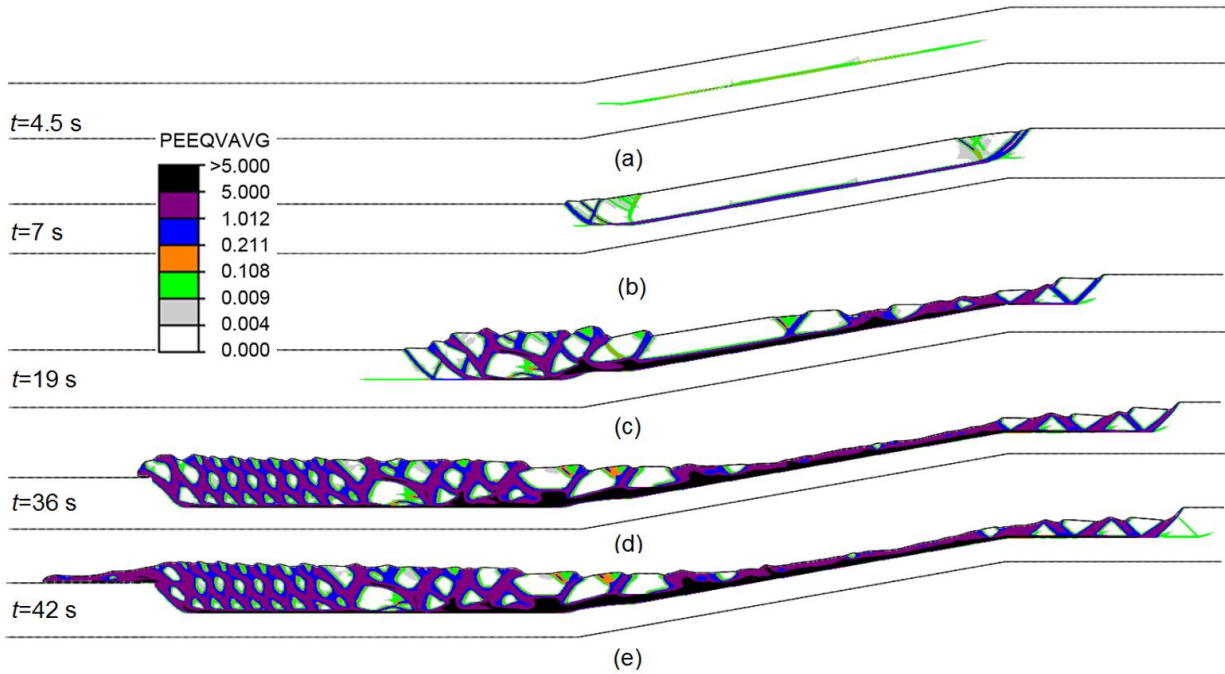
Figure 3.4: Formation of shear bands in Case-II

Figures 3.4(a) and 3.4(e) show that the failure pattern in this case is similar to Case-I. However, because of a thicker marine clay layer, the failed soil blocks displace faster than Case-I. At $t \sim 36$ s, the height of the accumulated soil in the ploughing area above the seabed (h_p) is considerable (maximum h_p is ~ 17 m), which cannot stand unsupported and therefore starts crumbling and causes run-out over the top of the stable zone. At $t = 42$ s, the front of the crumbled material moves ~ 79 m over the stable seabed, which represents the maximum run-out distance at this time.

3.6.3 Case-III

Case-III is similar to Case-I, except for the slope angles in the upslope and downslope areas ($\beta_2 = \beta_3 = 5°$), which are zero in Case-I. The marine clay layer is parallel to the slope.
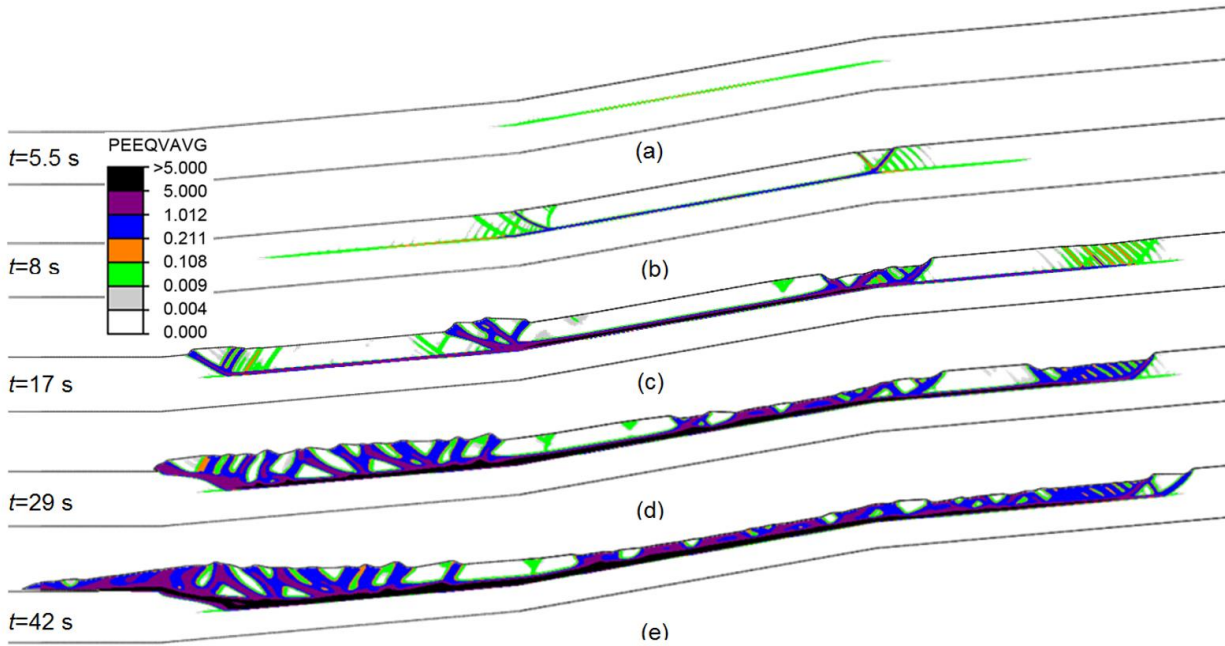
Figure 3.5: Formation of shear bands in Case-III

The slope is stable after the geostatic step. Due to the weak zone formation in Step 2, a long shear band generates parallel to the steeper slope (Fig. 3.5(a)). In addition, curved failure planes form at the ends, resulting in a global slab failure of this steep slope. In the third step of the simulation, the shear bands first propagate parallel to the slopes in the stable zones through the marine clay layer both in upslope and downslope areas until they reach close to the strong zone, where the sensitive marine clay layer does not exist.

During this time, a number of inclined shear surfaces also form in the glacial clay layer. With time, curved failure planes also form through the glacial clay layer. With continuation of the analysis, the failed soil from the upslope area moves downslope and creates additional pressure, which causes a number of rotational failures of the soil downslope. At $t \sim 29$ s, the height of the accumulated soil in the ploughing areas over the stable seabed is considerable (maximum h_p is $\sim$ 18 m), which cannot stand unsupported and therefore causes run-out. The maximum run-out

distance of the crumbled material at $t = 42$ s is ~ 120 m. The movement of the failed soil blocks does not stop at this time, although the analysis has been stopped.

3.6.4 Case-IV

Case-IV is similar to Case-III, except that Case-IV does not have strong layers; instead, the glacial and marine clay layers extend over the entire length of the domain (from left to the right boundary).
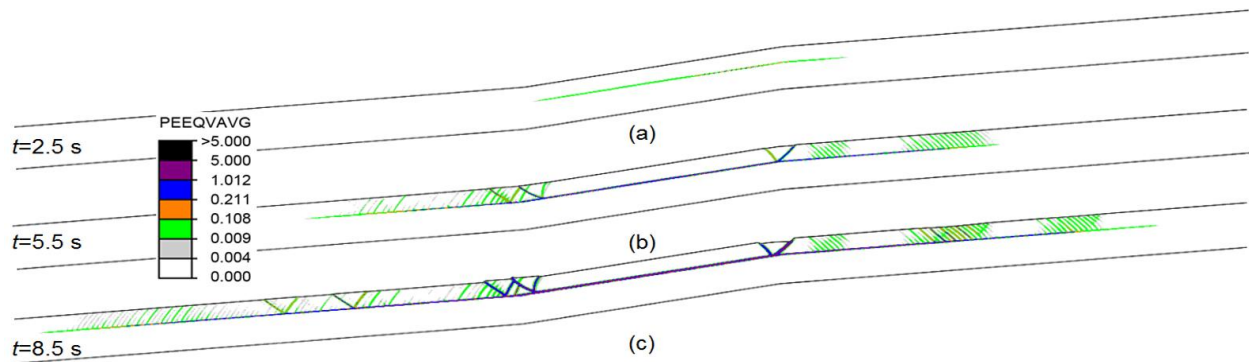
Figure 3.6: Formation of shear bands in Case-IV

In addition, the same slope angle is considered for the upslope and downslope stable zones ($\beta_2 = \beta_3 = 5°$). The main purpose of this simulation is to model the failure pattern when a steep slope exists between two long mild stable slopes. However, as the simulation is computationally expensive, a very long slope is not modeled. Figures 3.6(a) and 3.6(c) show the simulation results until the shear band parallel to the slopes reaches close to the boundary.

As in the previous cases, the weak zone could cause shear band propagation through the marine clay layer, in addition to global failures. Compared to Case-III (Fig. 3.5), the height of the accumulated soil above the seabed in the downslope areas is small because the displaced soil has been spread over a large distance. Therefore, run-out of the accumulated soil is not found in this case. Moreover, a number of inclined shear surfaces form both in the upslope and downslope areas.

42
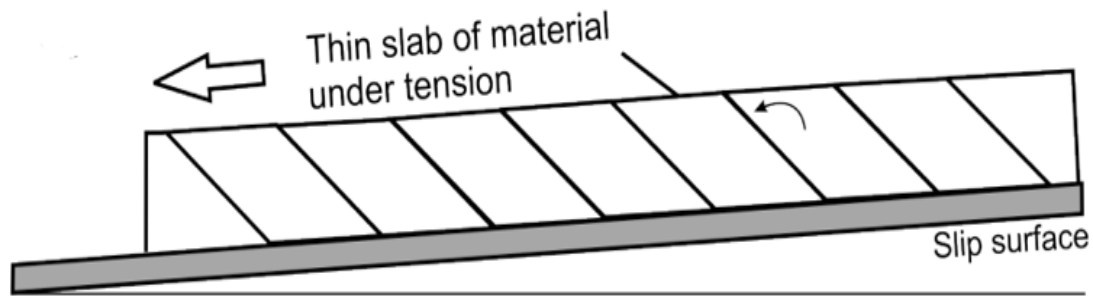
Figure 3.7: Slab extension and rupturing spreading failure (after Micallef 2007)

Based on the morphology and internal structure of the ridges within the Storegga Slide, Micallef (2007) proposed a model for the failure dynamics of spreading, considering slab extension and rupturing, as shown in Fig. 3.7. In this model, when a thin slab slides over a weak layer, the variation of extensional force and basal resistance could create a number of inclined shear surfaces. The present FE analysis shows a similar failure pattern (compare the right side of Fig. 3.6 with Fig. 3.7). Similar shear surfaces are simulated in the downslope area; however, the inclination of the shear surfaces is in the other direction because these surfaces develop due to compression.

3.7   Summary

This chapter has presented large deformation finite-element simulations of submarine slope failures. It is shown that a small weak zone could cause a large-scale submarine landslide by propagation of shear bands through strain-softening clay layers. The weak zone could cause a slab failure in the steeper section, which could then extend in the upslope and downslope stable zones. Upslope, because of reduction of support, spreading might occur, and downslope, the increase in soil pressure could cause ploughing and run-out of the accumulated soil. When the downslope area has no inclination, ploughing results in the formation of horst and grabens. When the upslope and downslope stable zones are inclined at an angle, a slab failure might also occur in these zones together with the formation of a number of shear surfaces in the failed soil. Run-out occurs when

the height of the accumulated soil above the seabed in the downslope areas is high. The present finite-element method can successfully simulate the large deformation process in submarine landslides.

CHAPTER 4

Modeling of Submarine Landslides in Sensitive Clay due to Earthquake

4.1   Introduction

A large number of small- and large-scale submarine landslides are triggered by earthquakes. Among the earthquake-induced large-scale submarine landslides, the Grand Banks Slide in offshore Newfoundland and Storegga Slide in the Norwegian Sea are well documented. In the Grand Banks, the slide was triggered by an earthquake of magnitude $M = 7.2$. The debris originating from this landslide broke twelve transatlantic telegraph cables located along the continental slope.

The Storegga Slide has been well studied to identify potential risks associated with submarine landslides in this area on the Ormen Lange gas field located at 850–1,100 m water depth. The Storegga Slide was most likely triggered by a strong earthquake (Bryn et al. 2005). The slide was initiated locally from relatively steep slopes ($\sim 10° - 20°$) and then retrogressed over a large area (Bryn et al. 2005). Figure 4.1 shows the process of the slide inferred from post-slide investigations.

Figure 4.2 shows the soil profile inferred from post-slide geotechnical investigations in the Storegga Slide area (Bryn et al. 2005). The red arrows in the inset of this figure represent soil units of marine sensitive clays which have significant strain-softening behaviour (Kvalstad et al. 2005a). The failure shown in Fig. 4.1 represents the progressive failure through the marine sensitive clay layer S2 in Fig. 4.2 (Bryn et al. 2005).
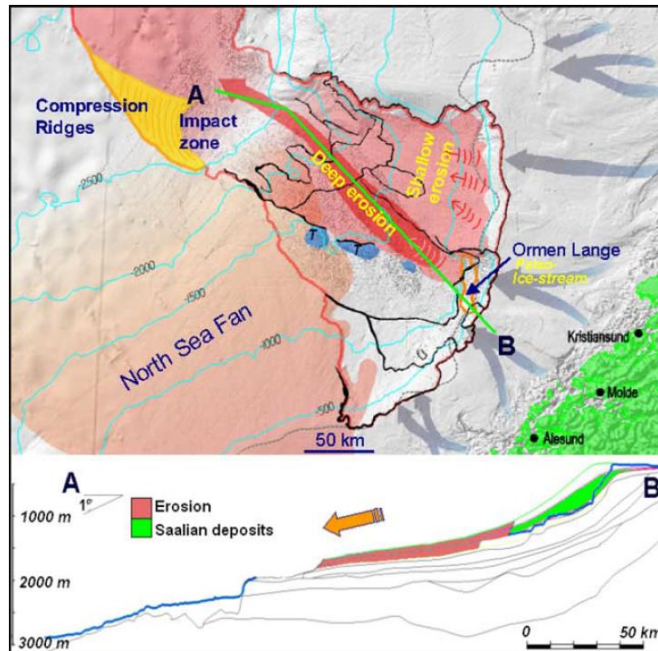
Figure 4.1: Storegga Slide development process (Bryn et al. 2005)
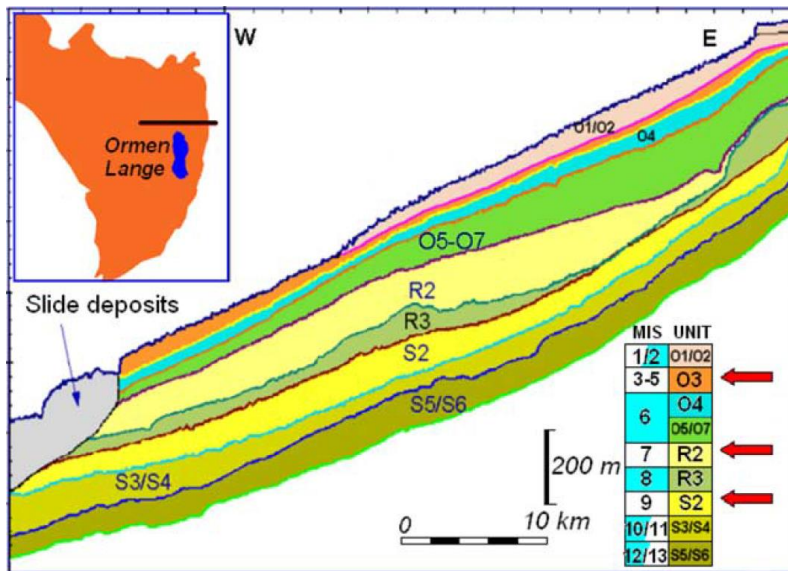
Figure 4.2: Stratigraphic layers in the Storegga Slide area (Bryn et al. 2005)

As reported in many onshore landslides, failure of a slope could occur during an earthquake (co-seismic failure) and also after the end of earthquake shaking (post-quake failure) (Ambraseys and Srbulov 1995; Sarma and Chlimintzas 2001; Dadson et al. 2004; Suito and Freymueller 2009; Grelle et al. 2011; Martino 2016). Underwater submarine slope failures might also have similar failure stages. Using the limit equilibrium method, however, as used in previous studies (e.g., Leynaud et al. 2004; Kvalstad et al. 2005a; Strasser et al. 2007; Rodríguez-Ochoa et al. 2015), co-seismic and post-quake failure stages cannot be analyzed properly.

Figure 4.3 shows the soil profiles of two sections of the Caspian seafloor (Gray et al. 2015; Puzrin et al. 2017). It has been interpreted that the failure initiates from the steep section of seabed and propagates. The blocks upslope are similar to horsts and grabens, as commonly observed in spreads in onshore sensitive clay slope failures (Locat et al. 2011). On the other hand, compression ridges/thrusts suggests ploughing of the sediments downslope (Gray et al. 2015).
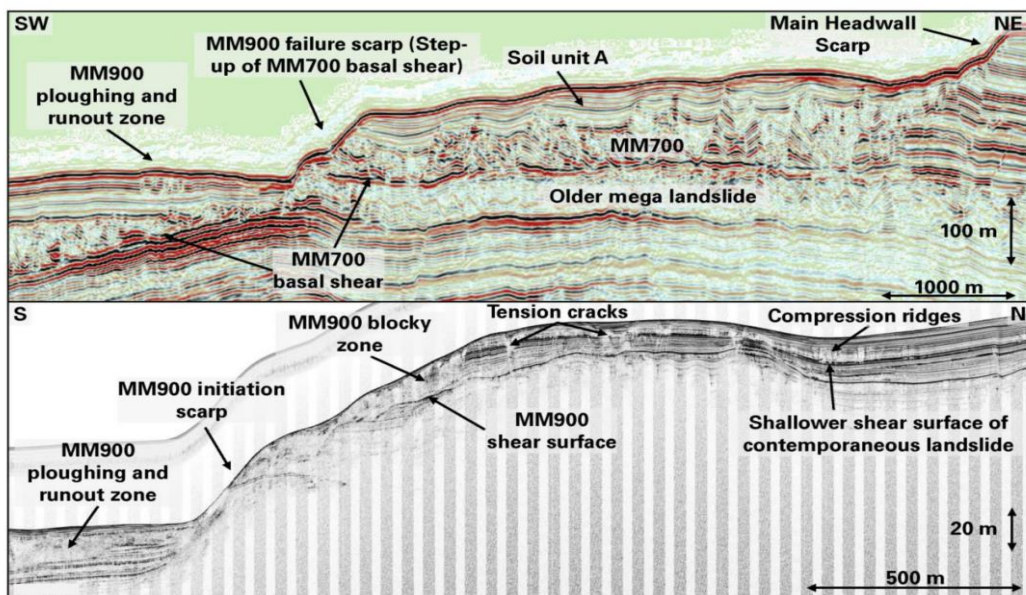
Figure 4.3: Seismic profile of two sections (Gray et al. 2015)

47

Based on the literature review on earthquake induced submarine landslides, the following knowledge gaps have been identified:

i. Whether an earthquake could decrease the shear strength of a marine sensitive clay layer to initiate failure by the formation of shear bands

ii. If a shear band forms in a relatively steep slope, how far it will propagate in the upslope and downslope directions

iii. Whether the propagation of a shear band will continue even after the earthquake (post-quake) as soil has strain-softening behaviour

iv. Whether the shear band propagation will continue in mild (even flat) upslope and downslope areas; and if it occurs, what would be the failure pattern and also the retrogression and downslope propagation distances

v. Whether runout will occur if a large volume of soil accumulates in the downslope areas

vi. Whether a complete dynamic analysis is required for modeling the failure process, or whether a simplified method could be used for practical purposes

In this chapter, the above issues are investigated for an idealized slope geometry by conducting large-deformation FE analysis where the strain-softening behaviour of soil is implemented.

4.2   Problem Definition

Figure 4.4 shows the geometry of the slope analyzed in the present study. A large soil domain of 1.5 km long is modeled in order to avoid boundary effects, especially during earthquake-loading and to accommodate upslope retrogression and downslope runout. A main slope angle β_1 of 10°, together with flat upslope and downslope angles ($\beta_2 = \beta_3 = 0°$), are considered.

The seabed profile consists of a 20-m thick low-sensitive glacial clay layer followed by a 1-m thick high-sensitive marine clay layer. At the upper and lower ends, a 300-m strong soil layer without any sensitivity is considered at a distance L_{ms} from the crests and toe, respectively, as shown in Fig. 4.4. To study the effects of these strong layers on failure, analysis is performed for two cases: $L_{ms} = 300$ m for Model-I and $L_{ms} = 800$ m for Model-II. Below the marine sensitive clay and strong layers, a base layer of very strong material is considered.
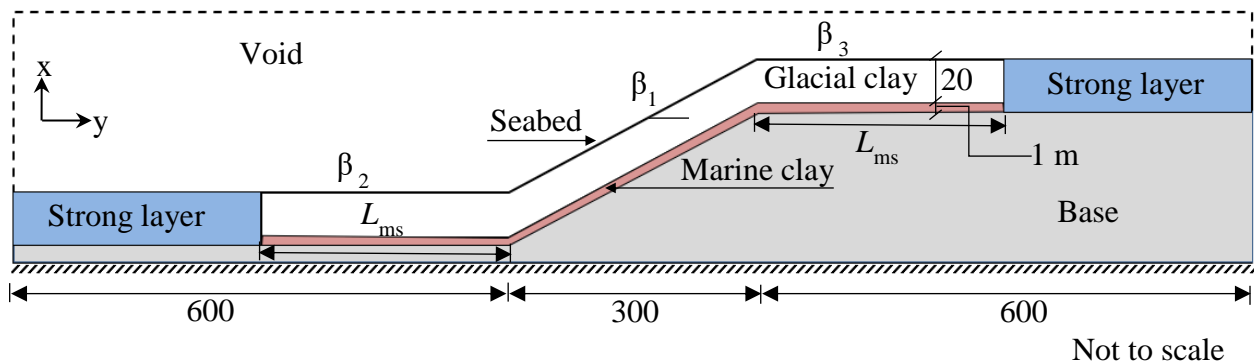
Figure 4.4: Geometry of the slope used in the finite-element analysis

4.3   Finite-element modeling

Abaqus 6.14.2 finite-element software used for numerical analyses. Similar to Chapter 3, the soil is modeled as a Eulerian material such that large deformation of soil after failure can be simulated without mesh distortion. The FE model in Abaqus consists of two parts: soil and void (Fig. 4.4). Three-dimensional FE modeling is performed considering only one element in the out-of-plane direction in order to simulate the plane strain condition. The domain is discretized using 8-noded linear brick elements with reduced integration (EC3D8R). To create the seabed and slope geometry, a Eulerian Volume Fraction (EVF) equal to 1 is assigned to the elements below the seabed. However, for the elements above the seabed, the EVF = 0 (i.e., void).

A zero-velocity boundary condition is applied normal to the bottom and two out-of-plane vertical faces in order to make sure that the Eulerian material remains within the domain. No boundary condition is applied at the soil–void interface so that the deformed soil mass can move to the void space when needed. For the left and right vertical faces, a zero-velocity boundary condition is applied for pseudostatic FE analysis, while a non-reflecting boundary condition is used for dynamic FE analyses.

4.4   Loading steps

Finite-element modeling consists of the following steps. First, the gravitational acceleration (g) is increased slowly to create geostatic stresses, maintaining the ratio between lateral and vertical effective stress equal to 1.0. No plastic shear strain is generated at the end of the gravitational loading step, which implies that the slope is stable before the earthquake. In the dynamic FE analysis, the earthquake loading is applied by applying a horizontal excitation (acceleration–time) at the base of the model (Fig. 4.4). Simulations are also performed for pseudostatic loading (the application of an earthquake load for that conditions are discussed later) (Section 4.8). Finally, after the completion of the earthquake loading, the analysis is continued for a period to understand the post-quake response.

4.5   Earthquake motion

In the dynamic FE analyses, the acceleration–time history of the Whittier Narrows Earthquake shown in Figure 4.5(a) is applied at the base of the model.
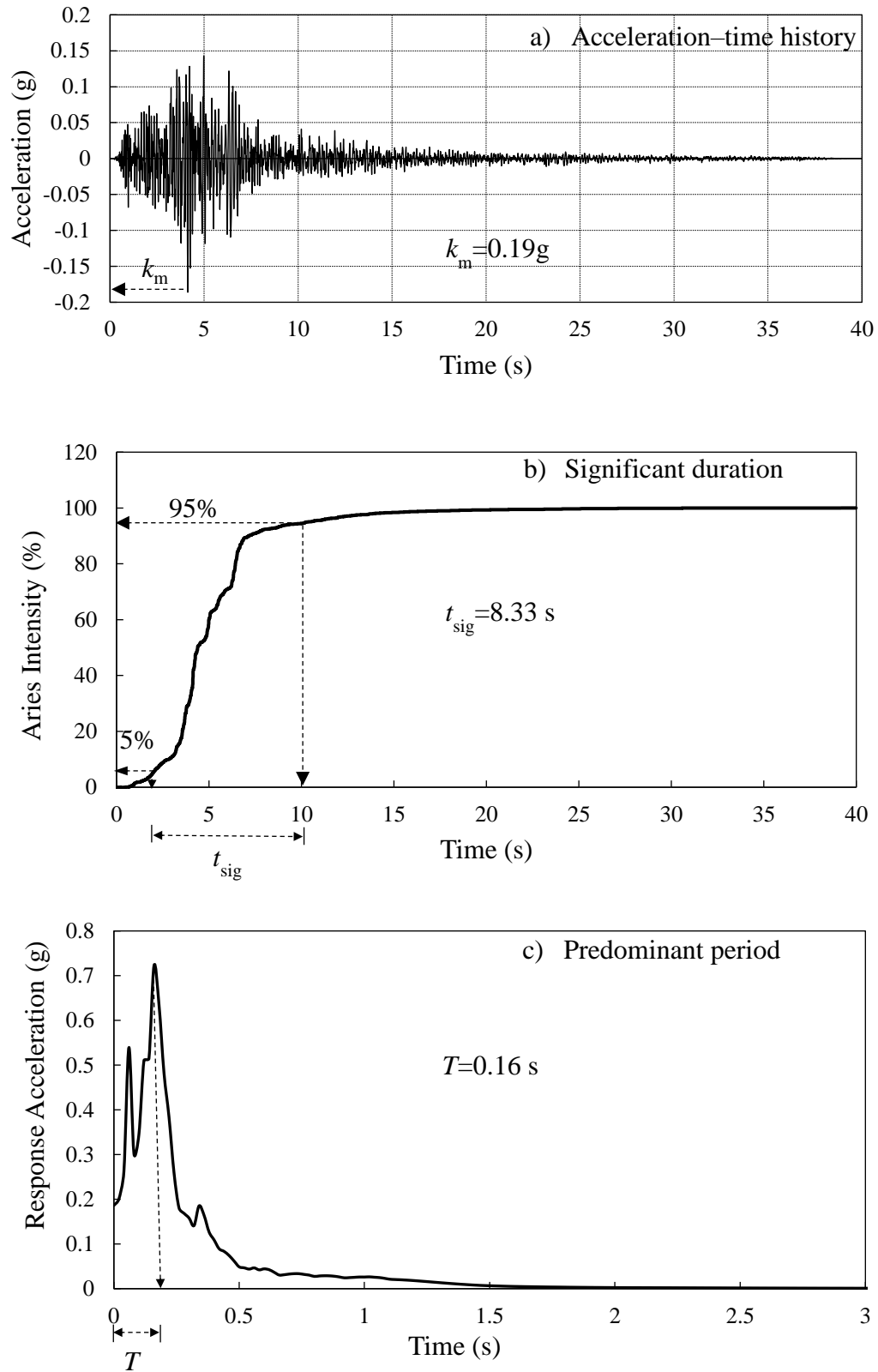
Figure 4.5: Input motion used in finite-element analysis: the Whittier Narrows Earthquake

The data for acceleration–time were obtained from the Pacific Earthquake Research center (PEER) ground motion database (PEER 2010). Analyzing the acceleration–time data using Seismsignal software (Seismosignal 2016), the significant duration of t_{sig} = 8.33 s and the predominate period T of 0.16 s are calculated. This information will be used to calculate the pseudostatic coefficient (k_h) of this earthquake, as discussed later.

4.6   Modeling of soil

Glacial and marine/glacimarine clays are commonly observed in many offshore environments. In general, the sensitivity of marine clays is higher than that of glacial debris (Tjelta et al. 2002; Laberg et al. 2003; Kvalstad et al. 2005b; Yang et al. 2006). For the Ormen Lange gas field development project, comprehensive field and laboratory tests were conducted for geotechnical characterization of the sediments in order to check the stability of the slope (Kvalstad et al. 2005b). The cone penetration tests showed layers of sensitive weak clays through which failure might occur. Laboratory tests included index tests (e.g., liquid limit, plastic limit) and shear strength tests. In addition to monotonic triaxial and direct simple shear (DSS) tests, a number of cyclic DSS tests were conducted to investigate earthquake loading effects, and it was shown that the undrained shear strength decreases with increases in accumulated shear strain. The cyclic response of normally consolidated and lightly overconsolidated clays and its relationship to submerged slope stability have also been investigated through dynamic DSS testing (Pestana and Nadim 2000; Pestana and Biscontin 2001).

In addition, many field investigations have been conducted for the geotechnical characterization of different seabed sediments, using cone penetration, cyclic T-bar and ball, and vane shear tests (Stewart and Randolph 1994; Randolph et al. 1998; Watson et al. 1998; Randolph 2004; Low and

Randolph 2010). Randolph and his coworkers showed that the undrained shear strength of seabed sediments decreases with accumulated plastic shear strain, and proposed a model (exponential equation) for strain-softening behaviour (Einav and Randolph 2005). Calibrating against cyclic T-bar and ball test results, they also identified the parameters required for the strain-softening model (Einav and Randolph 2005; Pinkert and Klar 2016). Nadim (1998) considered a linear degradation of undrained shear strength with accumulated shear strains during cyclic loading.

In the present study, nonlinear degradation of undrained shear strength (Eq. 3.1 & Fig. 3.2) is used. However, in this case, the accumulated shear strain is calculated by summing up the plastic shear strains generated in the loading and unloading phases during earthquake loading. The soil parameters used in finite-element modeling are listed in Table 4.1. The marine and glacial clays have strain-softening behaviour, while the base and strong layers are assumed to be elastic. The material damping is incorporated using Rayleigh damping, assigning a proportional stiffness damping (β') of 0.000375. In Abaqus, mass proportional damping is ignored in Eulerian materials, and the geotechnical parameters are estimated based on a comprehensive review of the geotechnical properties of seabed sediments presented in previous studies, as discussed above.

Similar to the weak layer case, as discussed in Chapter 3, the yield strength ($= 2s_u$) is given as a function of the equivalent plastic shear strain ϵ_q^p ($=$ PEEQVAVG in Abaqus), adopting the von Mises yield criterion.

Table 4.1: Parameters used for finite-element modeling

Parameters	Values		
	Glacial clay	Marine clay	Base & strong layers
Undrained Young's Modulus, E_u (MPa)	30	15	200
Poisson's ratio, ν_u	0.495	0.495	0.495
Peak undrained shear strength, s_{up} (kPa)	37.5	33.5	-
Residual undrained shear strength, s_{uR} (kPa)	$s_{up}/3$	$s_{up}/6$	-
Plastic shear displacement for initiation of softening, δ_{pc} (m)	0.01	0.003	-
Plastic shear displacement for 95% degradation of soil strength, δ_{95} (m)	0.18	0.09	-
Unit weight of soil, γ' (kN/m^3)	10	8	11
Rayleigh damping parameter (β')*	0.000375	0.000375	-

*Damping parameter considered for dynamic analysis only

4.7   Dynamic finite-element analysis results

Figure 4.6 shows the process of slope failure with time. The gravitational loading is completed at $t = 2$ s. No plastic shear strain is generated at the end of this step (not shown in Fig. 4.6). As shown in Figure 4.5(a), the earthquake loading mainly occurs in the first 8.33 s. The earthquake loading creates a shear band in the marine clay layer parallel to the slope, as shown in Fig. 4.6(a) for $t = 8$ s. The length of the shear band at this stage is 375 m. Although the magnitude of the earthquake

acceleration decreases after $t \sim 8$ s, the shear band propagation continues with time in both the upslope and downslope directions. A $t \sim 9.5$ s, the shear band reaches the end of the slope (below the toe and crest). As a large slab of soil moves downward parallel to the slope, the unloading upslope and increase in pressure downslope cause circular failures of the soil above the shear band near the crest and toe, respectively. This causes a global failure of the soil mass CABD (Fig. 4.6(c)). With the displacement of this soil mass, two V-shaped wedges (CAE & FBD) form near the crest and toe. With displacement of the large soil slab, the shear band propagates horizontally along the marine clay layer both in the upslope and downslope areas, as shown in Figs. 4.6(c–i). With time, additional shear bands inclined at ~ 45° to the horizontal form because of the unloading in the upslope and pressure increase in the downslope areas. This results in the formation of a series of V-shaped grabens and Λ-shaped horsts. The retrogressive failure in the upslope area is similar to spreading, as commonly observed in onshore sensitive clay slope failures (Locat et al. 2011). This type of failure has also been observed in offshore environments, for example in the upper headwall in the Ormen Lange area (Kvalstad et al. 2005a). Moreover, Puzrin et al. (2016) showed this type of spreading failure in mild upslope areas for a varying seabed angle.

The formation of inclined shear bands in glacial clay (see Fig. 4.4) due to passive failure of soil, together with horizontal shear band propagation in the marine clay layer, represents "ploughing" downslope as observed in offshore environments (Gray et al. 2015; Puzrin et al. 2016).

The lateral extent of the landslide (L_E) can be calculated as the sum of upslope "retrogression distance (L_R)", "slope length L_S", and downslope "ploughing distance (L_P)" (Fig. 4.6(i)). In this study, L_R and L_P measure the horizontal distance from the crest and toe of the steep slope, respectively, to the furthest location of the shear band, which might be at the seabed surface or at the tip of a local shear band in the marine clay (e.g. Fig. 4.6(i)). In the present simulation, the

maximum L_E = 625 m, where L_R = 69 m and L_P = 256 m, which occurs at t > 51 s when the instantaneous velocity of the failed soil blocks is negligible.
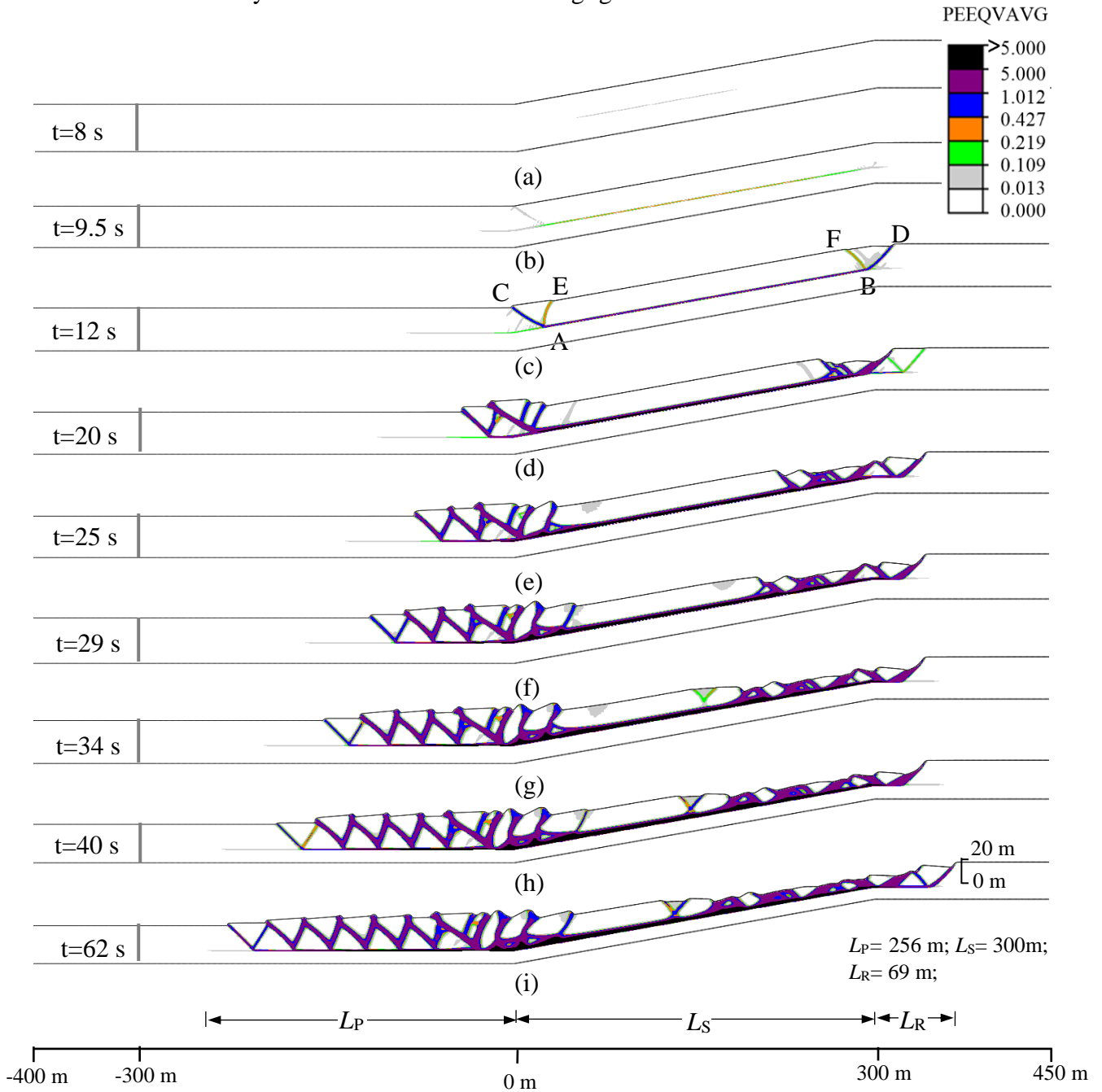
Figure 4.6: Model-I: Formation of shear surface and corresponding slope failure during the dynamic FE analysis

The height of the glacial clay is significantly reduced in the upper part of the slope. For example, the thickness of clay above the marine clay layer near the crest at t = 62 s is ~ 11 m (initially 20

m). This implies that the reduction in soil height due to large deformation needs to be considered in the development of shear band propagation criteria.

Significant heaving occurs in the downslope areas. For example, the maximum heave at $t = 62$ s is ~ 10 m. However, as it distributed over a large area (~ 256 m length, see Fig. 4.6(i)), the heaved soil mass does not move over the original seabed. It is to be noted that if the downslope profile is inclined downward, there is a high possibility of run-out of this material.

Figure 4.7 shows the development of the shear band with time for Model-II, where the upslope and downslope strong layers are located far from the toe and crest ($L_{ms} = 800$ m) as compared to Model-I ($L_{ms} = 300$ m, Fig. 4.6). Similar to Fig. 4.6 for Model-I, the earthquake creates a shear band in the steep slope through the marine clay layer and causes a global failure of the slope. After that, retrogression and ploughing continue in the upslope and downslope areas, respectively, at failure process stops at t ~ 46 s (negligible instantaneous velocity). The extent of the landslide (L_E) in this case is 654 m, where $L_R = 70$ m and $L_P = 284$ m, which is slightly greater than the L_E for Model-I (= 625 m, Fig. 4.6).
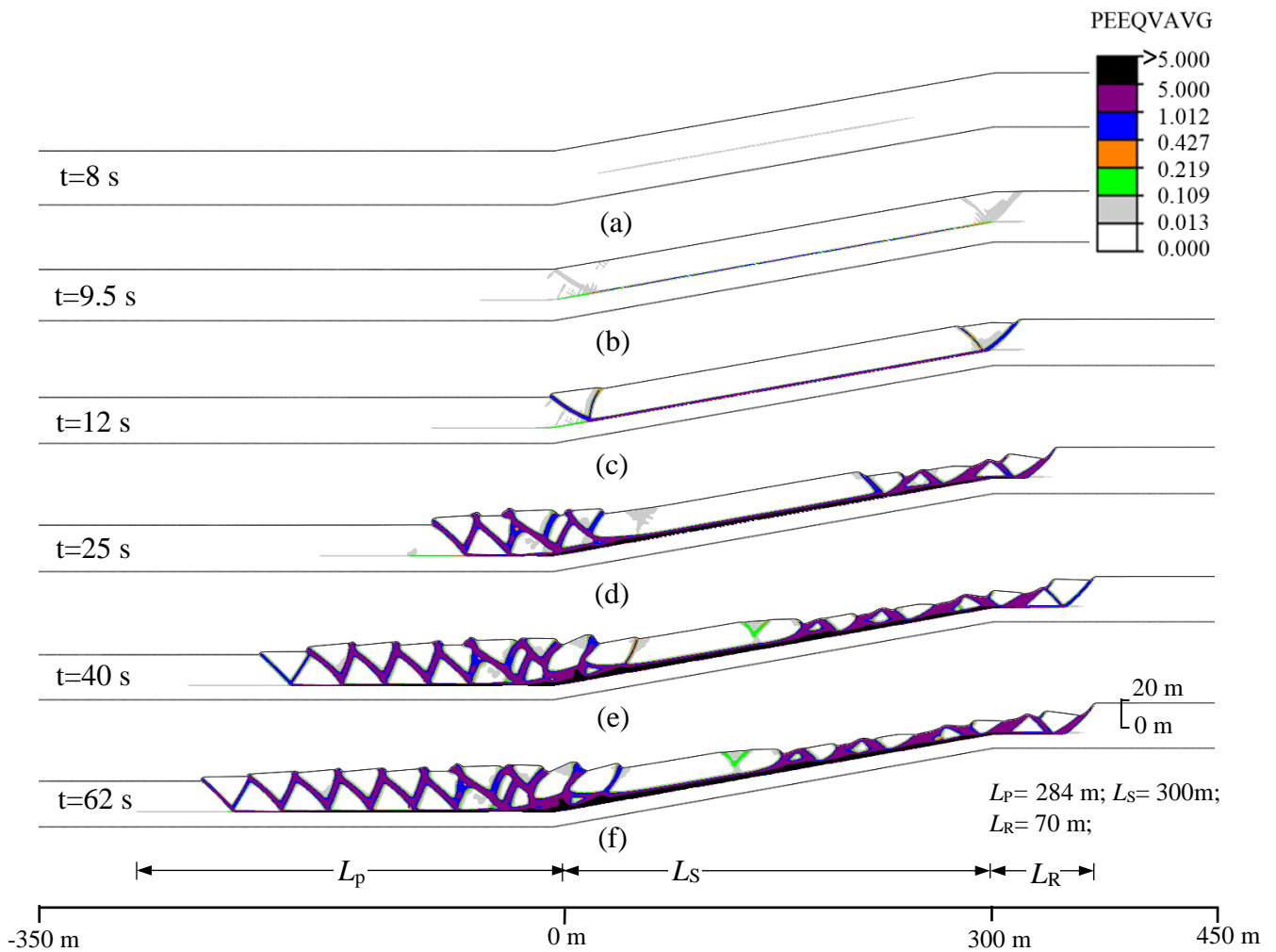
Figure 4.7: Model-II: Formation of shear surface and corresponding slope failure during the dynamic FE analysis

In summary, the present dynamic FE analysis can successfully simulate the large deformation of soil mass in a large-scale landslide triggered by an earthquake. Although extremely large shear strains are generated in the shear bands, the analysis continued without any numerical issues related to mesh distortion. The present dynamic FE analysis can also simulate the processes of upslope spreading and downslope ploughing.

4.8   Modified pseudostatic analysis

A large deformation dynamic finite-element analysis, as presented in the previous sections, is difficult in terms of FE model development, application of earthquake load, and setting appropriate boundary conditions. Therefore, a simplified approach is presented in this section for earthquake loading instead of conducting a complete dynamic FE analysis.

Newmark's rigid block method (Newmark 1965) and modified Newmark methods (Kramer and Smith 1997) are commonly used to calculate the displacement of a failed soil mass due to an earthquake. Sarma (1975) proposed a method to calculate the displacement of a failed soil block from earth dams or embankments, idealizing the process as a rigid body sliding over a plane surface. Moreover, instead of using the full acceleration time history, the earthquake load is applied using a single pulse of rectangular, triangular and half-sine curve. The maximum acceleration for these simplified pulses is assumed as the maximum acceleration of the acceleration time history (k_mg). Moreover, the duration of loading (i.e., existence of acceleration) is equal to half of the predominant period of the earthquake (T). Comparing the field data for dams and embankments, Sarma (1975) showed that the triangular pulse is more effective for $k_c/k_m > 0.5$ while the rectangular pulse is better for $k_c/k_m < 0.5$, where k_c is the critical seismic coefficient at which slope failure occurs (i.e., factor of safety is equal to 1.0).

In the present study, an approach similar to that proposed by Sarma (1975) is used. For the Whittier Narrows Earthquake considered in this study, $k_m = 0.19$, $T = 0.16$ s (Figs. 4.5(a) & 4.5(c)). Rectangular (Approach-1) and triangular (Approach-2) pulses are used to apply the earthquake load, as shown in Figs. 4.8(a) & 4.8(b), respectively.

Pseudostatic slope stability analysis is one of the methods commonly used to calculate the factor of safety of a slope for earthquake loading. Although it has not been developed to calculate the

displacement of the failed soil mass, the recommended values of pseudostatic coefficient (k_h) has been calibrated for a maximum seismic displacement of 1.0 m (Seed 1979; Bray and Travasarou 2009). In finite-element analysis, the value of k_h is gradually increased to the targeted value to evaluate the critical value of the pseudostatic coefficient that initiates failure (Loukidis et al. 2003; Sarma and Tan 2008). In the Lagrangian-based FE formulation, when the velocity of the failed soil suddenly increases, or a complete shear band develops, it is considered as a failure of the slope (e.g., Sarma and Tan 2008).

A similar approach is also used in the present FE analyses (Approach-3 in Fig. 4.8(c)). However, as the numerical instability related to mesh distortion is not an issue in the present FE formulation, the k_h can be maintained over a longer period of time even when progressive failure at large deformation occurs. Pyke (1991) developed a chart for the estimation of k_h as a function of the earthquake magnitude and peak acceleration. For the Whittier Narrows Earthquake (Fig. 4.5(a))—magnitude of 6.0 and peak acceleration of 0.186g—the estimated k_h is 0.032 based on Pike (1991), which is applied gradually with time as shown in Fig. 4.8(c). As the k_h is maintained as constant, even after earthquake, care should be taken in the interpretation of this simulation results.

Finally, based on 81 simulation results using FLAC, Melo and Sharma (2004) recommended an equivalent triangular variation of k_h having the maximum value as a weighted average value (~ $0.5k_m$) and the duration equal to the significant duration of the earthquake. Note, however, that Melo and Sharma (2004) did not consider strain-softening of the soil. For the Whittier Narrows Earthquake considered in this study (k_m = 0.19, t_{sig} = 8.33 s, as shown in Figure 4.5(b)), the equivalent acceleration used in this approach (Approach-4) is shown in Fig. 4.8(d).
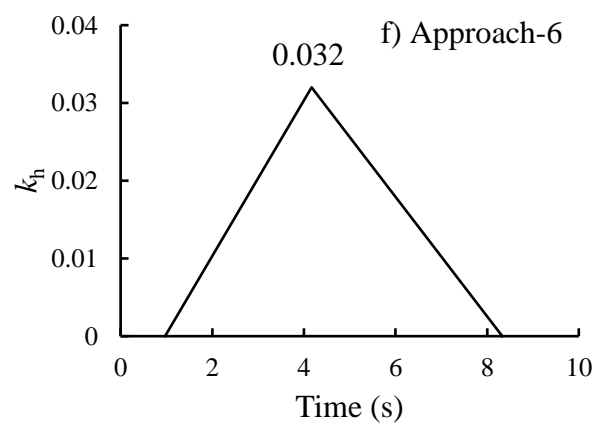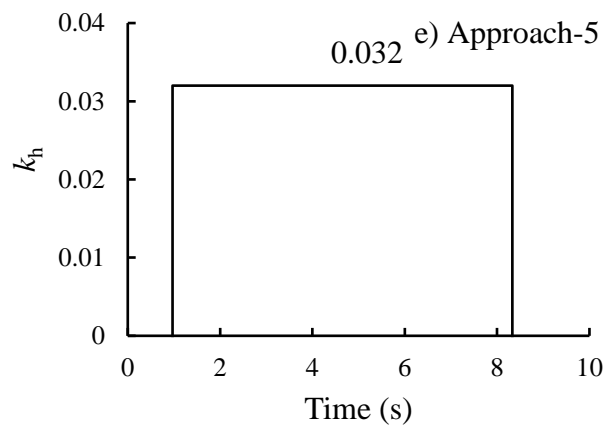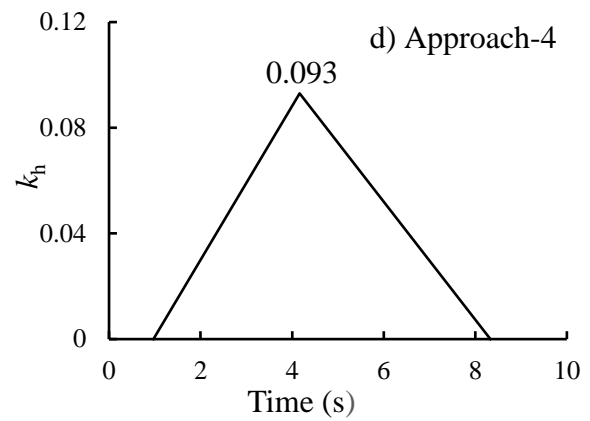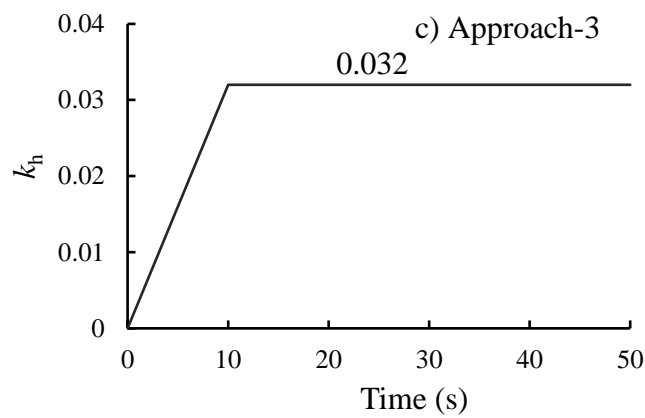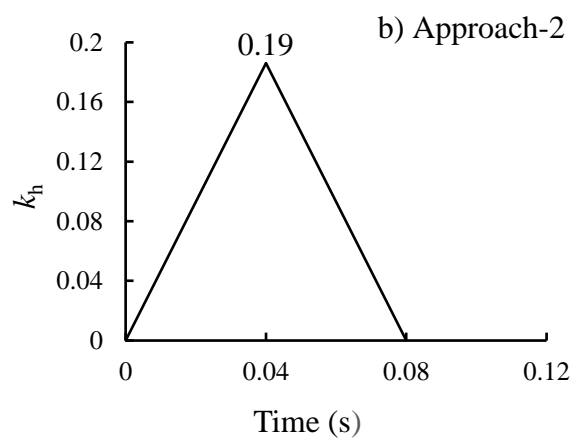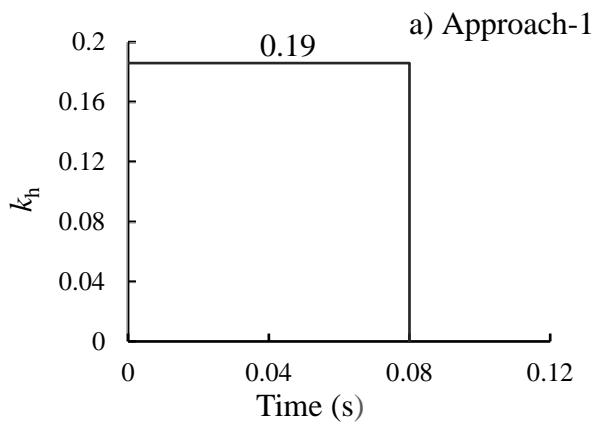
Figure 4.8: Pulses used for modified pseudostatic analysis

The author proposes two more approaches, as shown in Figs. 4.8(e) and 4.8(f). The total loading time is the same as in the previous approach ($t = t_{sig} = 8.33$ s), and the loading distributions are rectangular and triangular, having a peak value of $k_h = 0.032$.

<u>Loading and boundary conditions</u>

Similar to the loading steps discussed in Section 4.4 for dynamic FE modeling, the analysis is performed for three loading steps. However, in this case, the equivalent earthquake acceleration (Fig. 4.8) is applied as a body force in the horizontal direction in the soil elements, instead of applying the acceleration time history at the base of the model for the dynamic FE case. The gravitational loading and post-quake simulations are the same as for the dynamic FE analysis.

As cyclic loading is not applied in this case, the non-reflecting boundary condition is not required for the left and right vertical faces of the domain (Fig. 4.4). Instead, a zero-velocity boundary condition is applied to these faces for the simulations.

4.9   Modified pesudostatic FE simulation results

Figures 4.10 to 4.21 show the process of failure for the six approaches used for equivalent earthquake loading. As discussed above in the dynamic FE simulation part, the slope is stable after the gravity load and there is no plastic shear strain in the soil.

In Approach-1 and Approach-2, the acceleration is applied for a very short period (0.08 s). In these cases, a shear band in the marine clay layer parallel to the seabed is generated during the application of the acceleration. As the area of the rectangular pulse is double that of the triangular pulse, the overall kinetic energy at the end of the earthquake loading period (t=0.08 s) for the rectangular pulse are greater than those calculated with the triangular pulse (Fig. 4.9). Also, the higher kinetic energy in Model-II is because of larger domain as compared to Model-I.
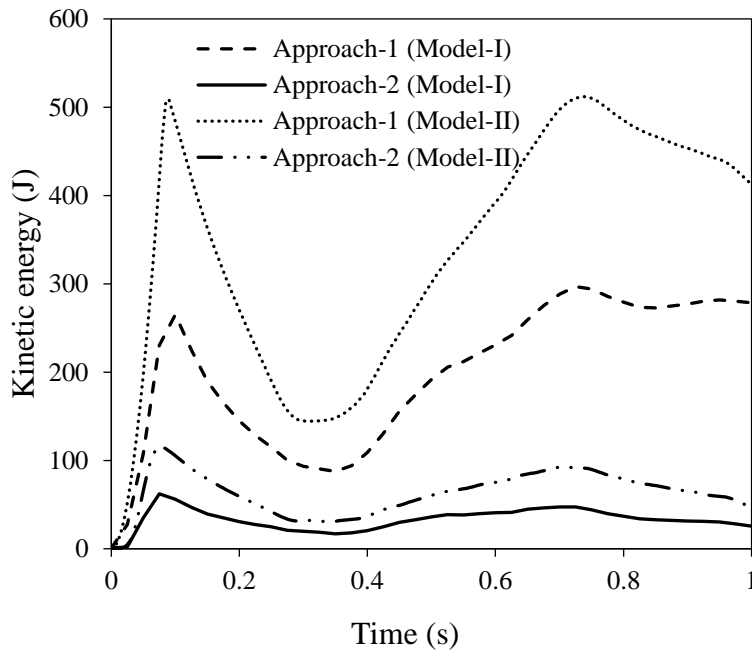
Figure 4.9: Comparison of kinetic energy based on Approaches-1 & 2

In the post-quake phase ($t > 0.08$ s), shear band propagation continues, and multiple soil blocks fail until the failed soil blocks come to equilibrium (Figs. 4.10(b–l) & 4.11(b–j)).

t=2.5 s

(a)

t=5 s

(b)

t=8 s

(c)

t=12s

(d)

t=17 s

(e)

t=20 s

(f)

t=22 s

(g)

t=25 s

(h)

t=29 s

(i)

t=34 s

(j)

t=40 s

(k)

t=62s

(l)

PEEQVAVG

> 5.000
5.000
1.012
0.427
0.219
0.109
0.013
0.000

20 m
0 m

L_P= 294 m; L_S= 300m;
L_R= 79 m;

L_p L_S L_R

-400 m   -300 m   0 m   300 m   450 m
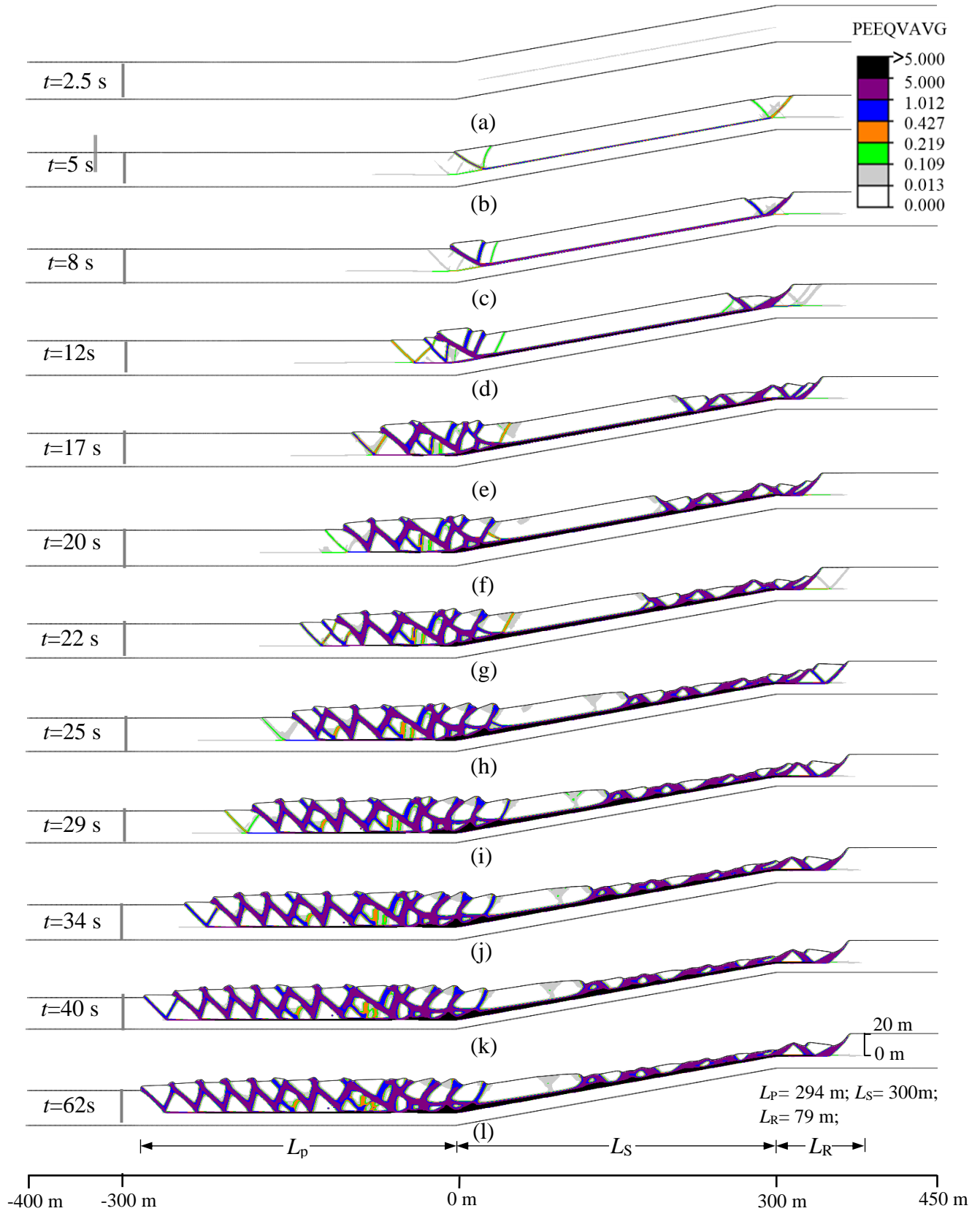
Figure 4.10: Model-I: Slope failure for equivalent earthquake based on Approach-1

64

Although the failure patterns are similar, the maximum lateral extents (L_E) of the landslides are slightly different: for the rectangular pulse $L_E = 673$ m, the $L_R = 79$ m and $L_P = 294$ m occur at $t > 41$ s, while for the triangular pulse $L_E = 681$ m, the $L_R = 94$ m and $L_P = 287$ m occur at $t > 45$ s.
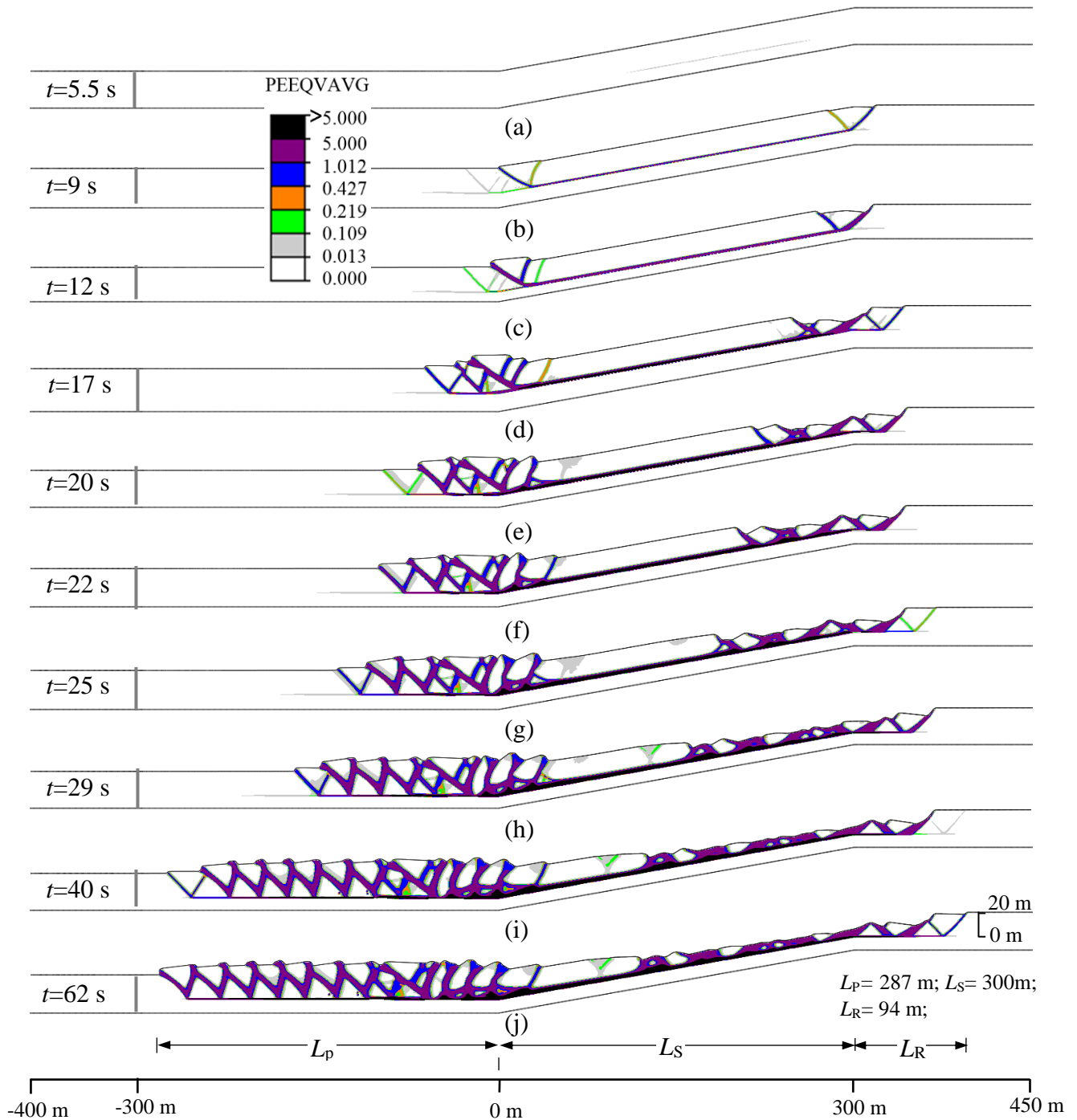
Figure 4.11: Model-I: Slope failure for equivalent earthquake based on Approach-2

The simulation results presented in Figs. 4.10 and 4.11 are for Model-I (L_m = 300 m, see Fig. 4.4). Figures 4.12 and 4.13 show the results for Model-II (L_m = 800 m) with Approache-1 (rectangular) and -2 (triangular pulse), respectively. The progressive formation of failure planes with time in these analyses are similar to Figs. 4.10 and 4.11. However, the maximum lateral extent (L_E) of the landslide is higher in the Model-II analyses (4.12 and 4.13) than those in the Model-I analysis (4.10 and 4.11), because the strong soil block is far from the steep slope in Model-II. The lateral extent for the Model-II simulations is 773 m for the rectangular pulse and 766 m for the triangular pulse, and occurs at ~52 s for both pulses.
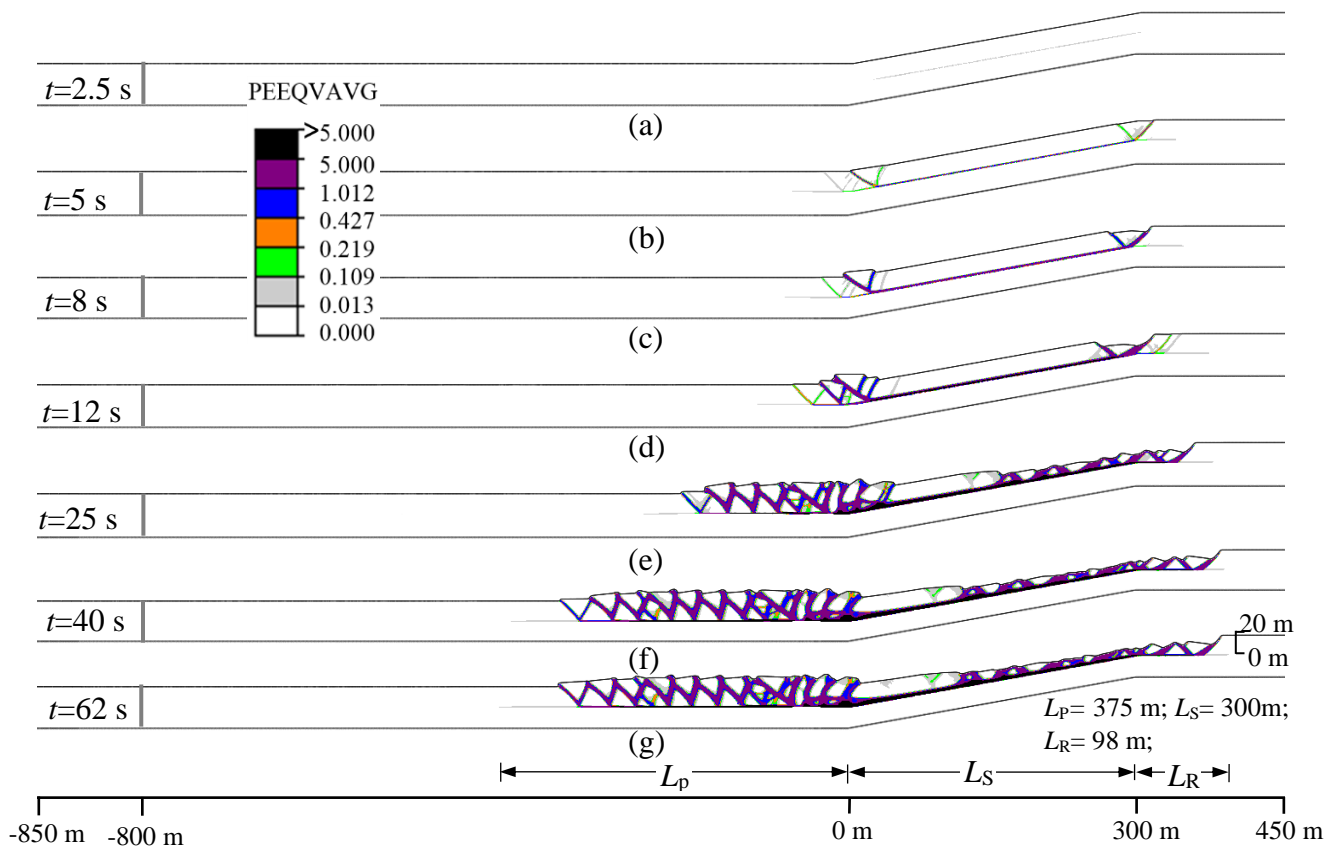
Figure 4.12: Model-II: Slope failure for equivalent earthquake based on Approach-1

66
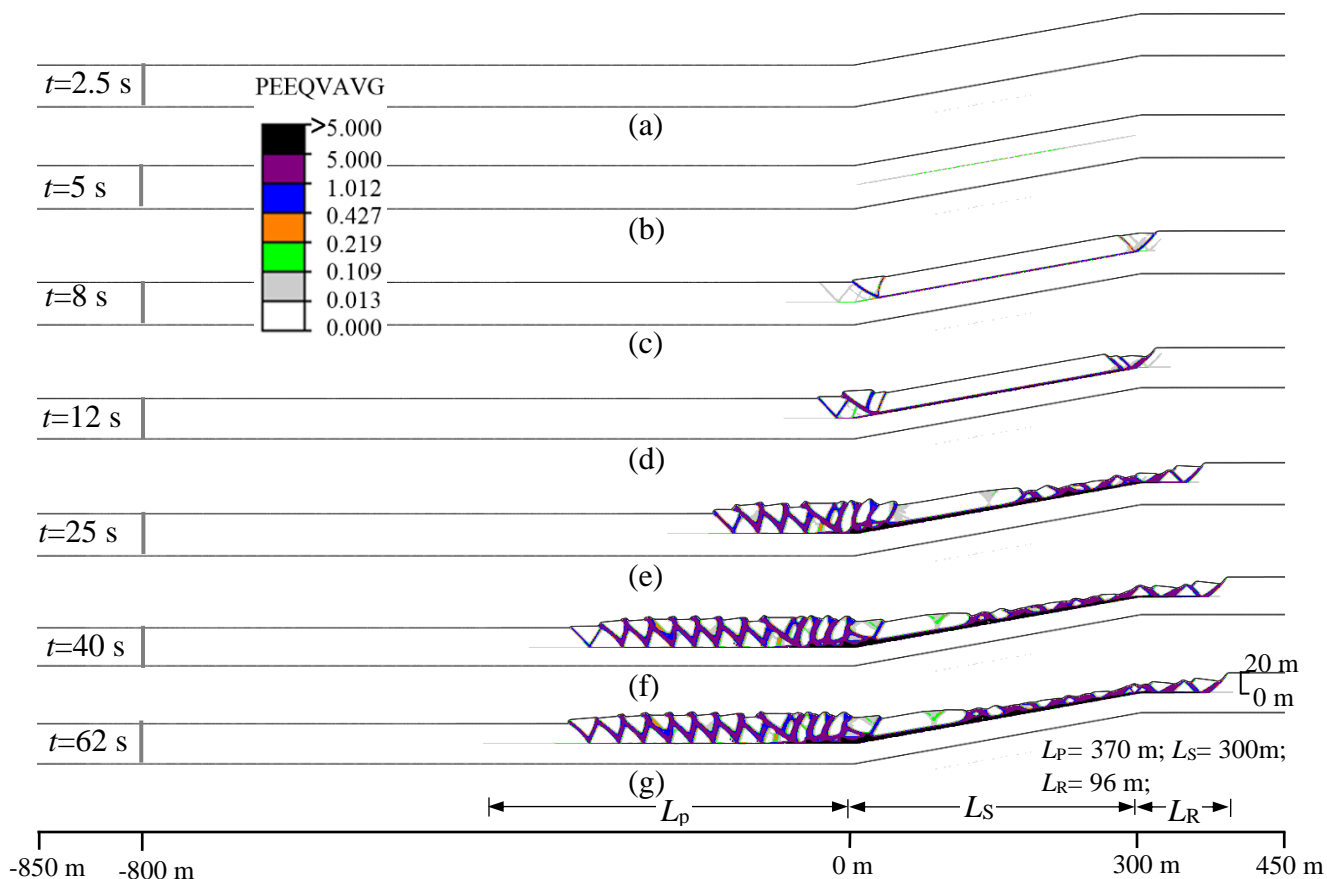
Figure 4.13: Model-II: Slope failure for equivalent earthquake based on Approach-2

In Approach-3, the acceleration is applied at a slower rate initially than for the rectangular and triangular pulse (Approaches-1 & -2). Moreover, the maximum acceleration in this case is smaller ($k_h = 0.032$) than for the rectangular and triangular pulses ($k_h = k_m = 0.19$). Therefore, the shear band generates slowly in this case (Fig. 4.14 & 4.15) as compared to Figs. 4.10–4.13. However, as the horizontal acceleration is kept constant after reaching the targeted value, the failure process continues with time.

With the Approach-3 earthquake loading, the simulations are performed for both Model-I and -II. For Model-I, the simulation was stopped by the user at $t = 44$ s, when the $L_E = 804$ m, $L_R = 147$ m, and $L_P = 357$ m (Fig. 4.14). In this model, the run-out of the soil over the seabed occurs when the

band reaches close to the strong soil layer. In contrast, when the strong soil block is placed farther away from the steep slope (Model-II), the run-out does not occur (Fig. 4.15); however, downslope ploughing over a large distance is found. The maximum lateral extent of the landslide with this approach is 1465 m, where L_R = 387 m and L_P = 778 m, and it occurs at t = 60 s.
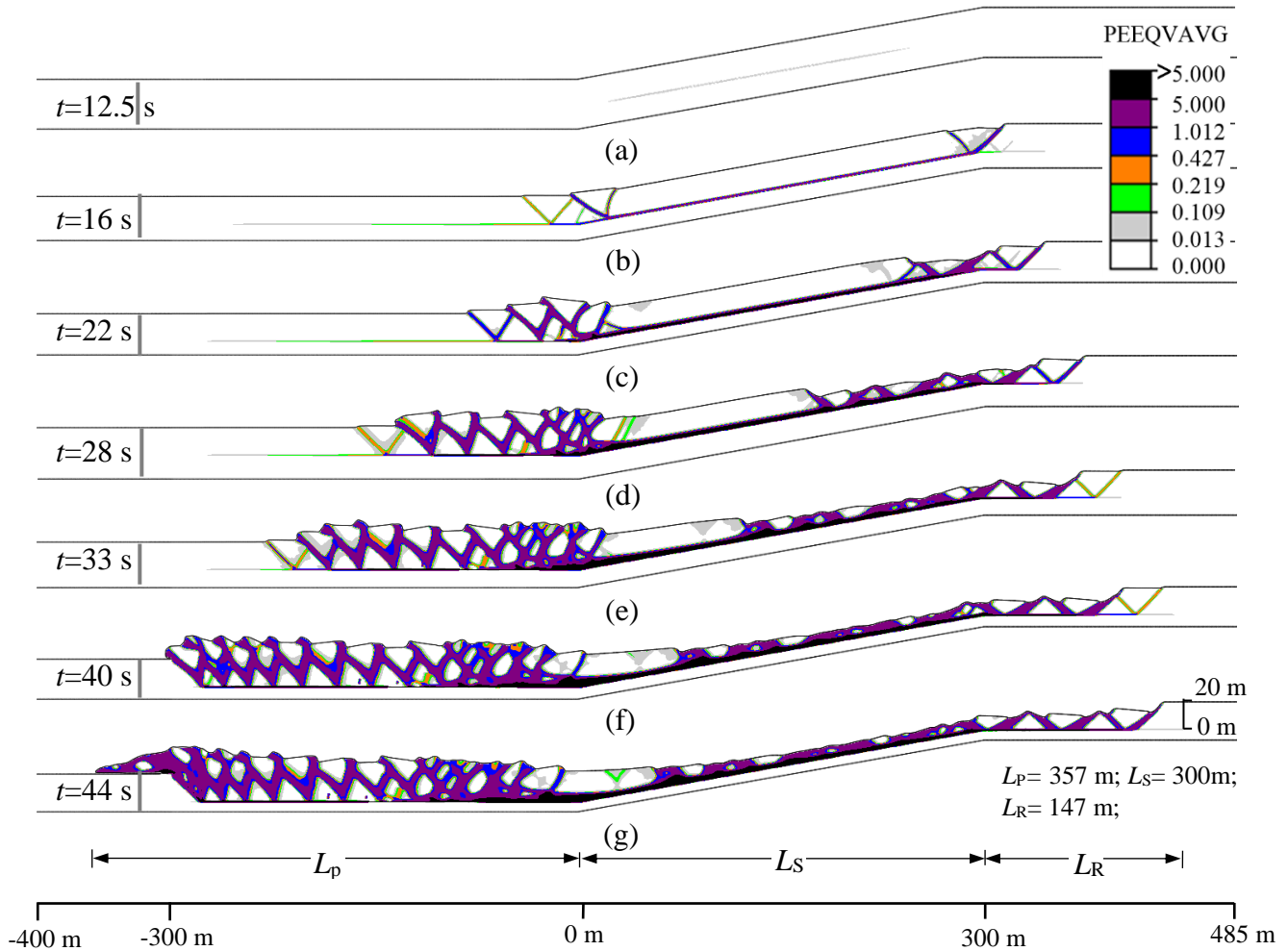
Figure 4.14: Model-I: Slope failure for equivalent earthquake based on Approach-3

68
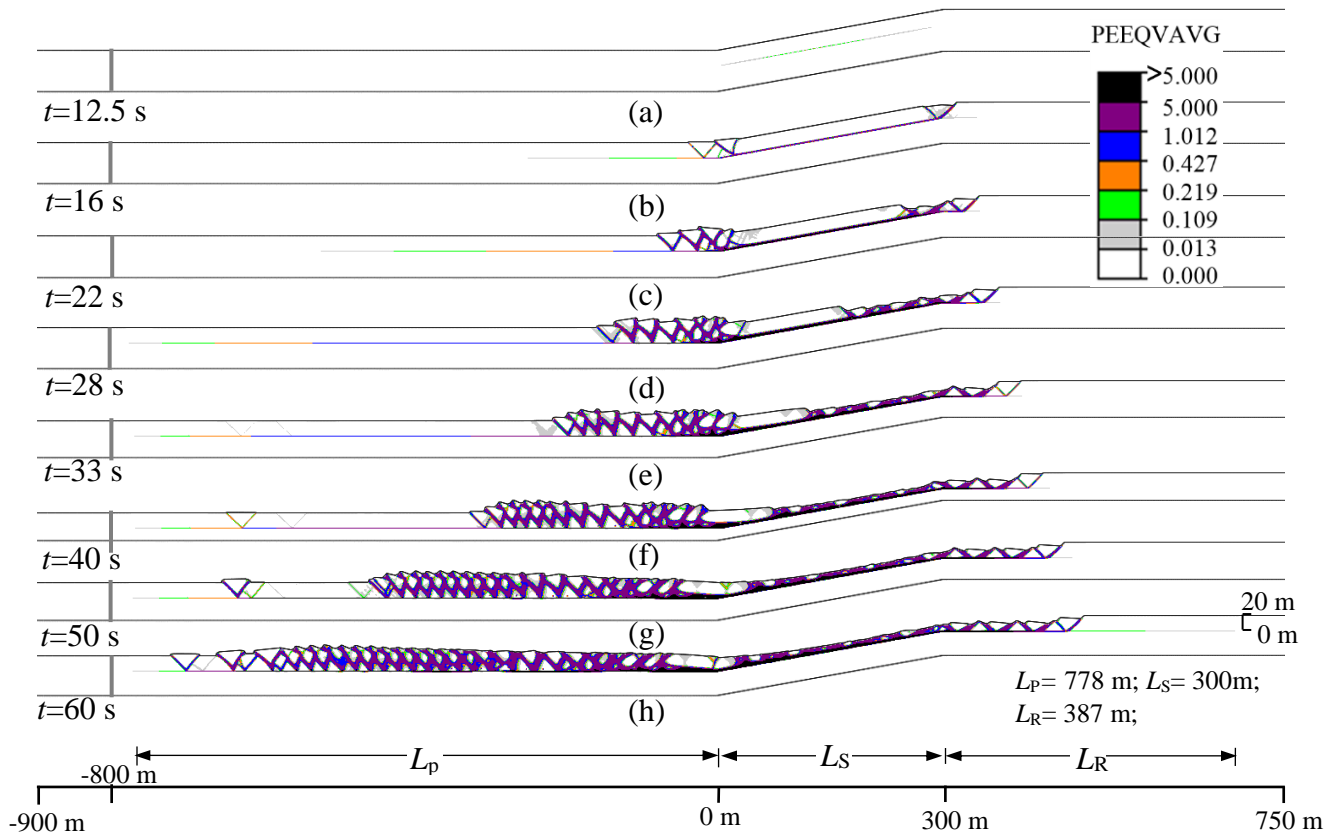
Figure 4.15: Model-II: Slope failure for equivalent earthquake based on Approach-3

In Approach-4, the acceleration is applied for a duration equal to the significant duration of the earthquake ($t_{sig} = 8.33$ s), which is significantly longer than the duration of the pulse in Approaches-1 and -2 ($t = 0.08$ s). However, the maximum seismic coefficient in this case is half of the peak ($\sim 0.5k_m$), which is also half of the seismic coefficient used in Approaches-1 and -2 ($= k_m$). Figures 4.16 and 4.17 show that shear bands generated quickly initially as compared to Figs. 4.10–4.13 for Approaches-1 and -2. For Model-I, the maximum lateral extent of the landslide (L_E) is 899 m, with $L_R = 294$ m and $L_P = 305$ m, and it occurs at $t = 52$ s. The shear bands propagate up to the strong layer both in upslope and downslope areas. The maximum accumulated soil over the original seabed is 11 m; however, run-out over the seabed does not occur, as is spread over a large horizontal distance.
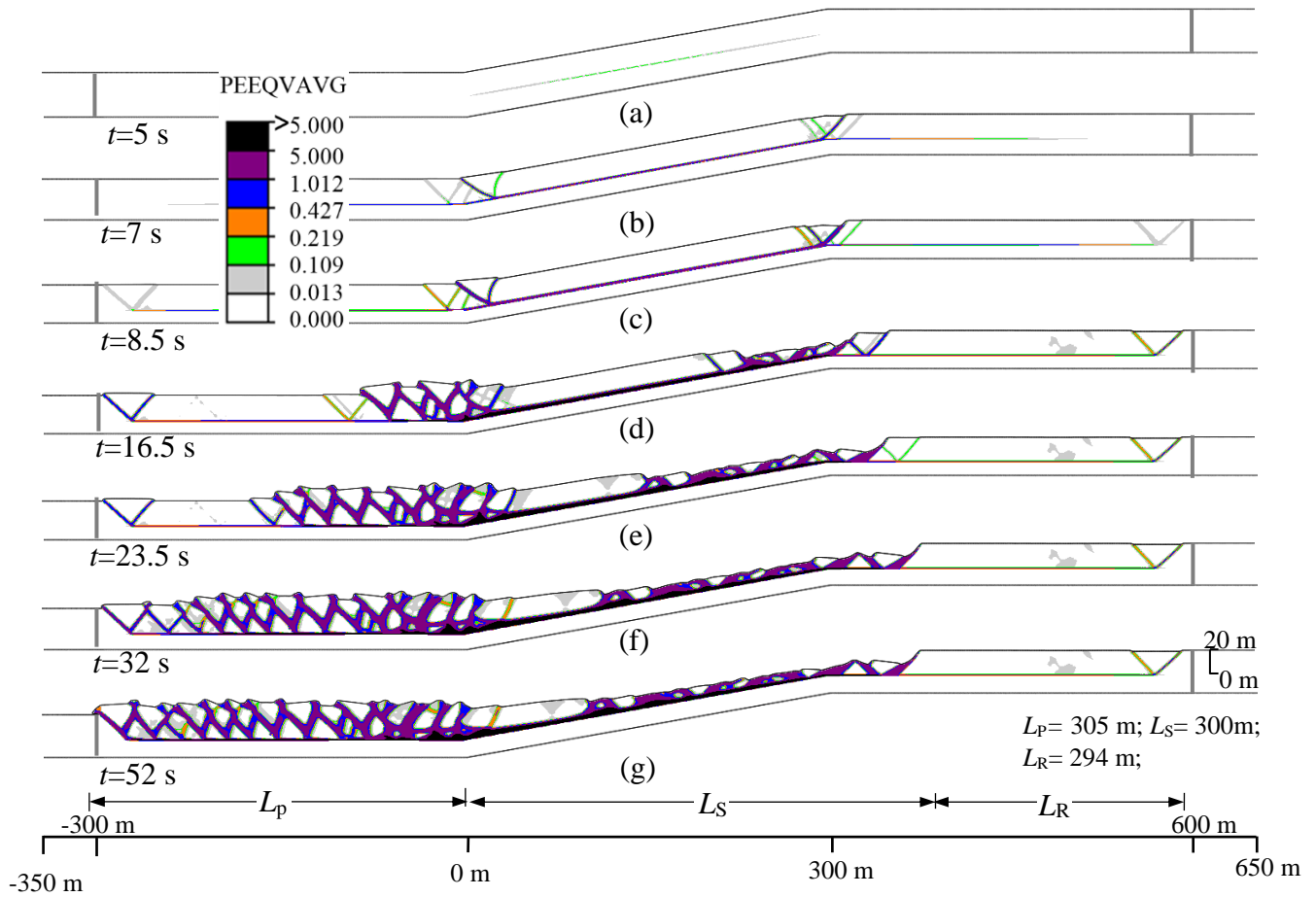
Figure 4.16: Model-I: Slope failure for equivalent earthquake based on Approach-4

For Model-II, the strong soil layers on the sides of the steep slope are 800 m from the toe and crest of the slope. Figure 4.17 shows the failure patterns with time. The maximum lateral extent (L_E) of the landslide was 1308 m, with L_R = 444 m and L_P = 564 m, and it occurs at t = 52 s. In this simulation also, run-out of the accumulated soil in the downslope does not occur.
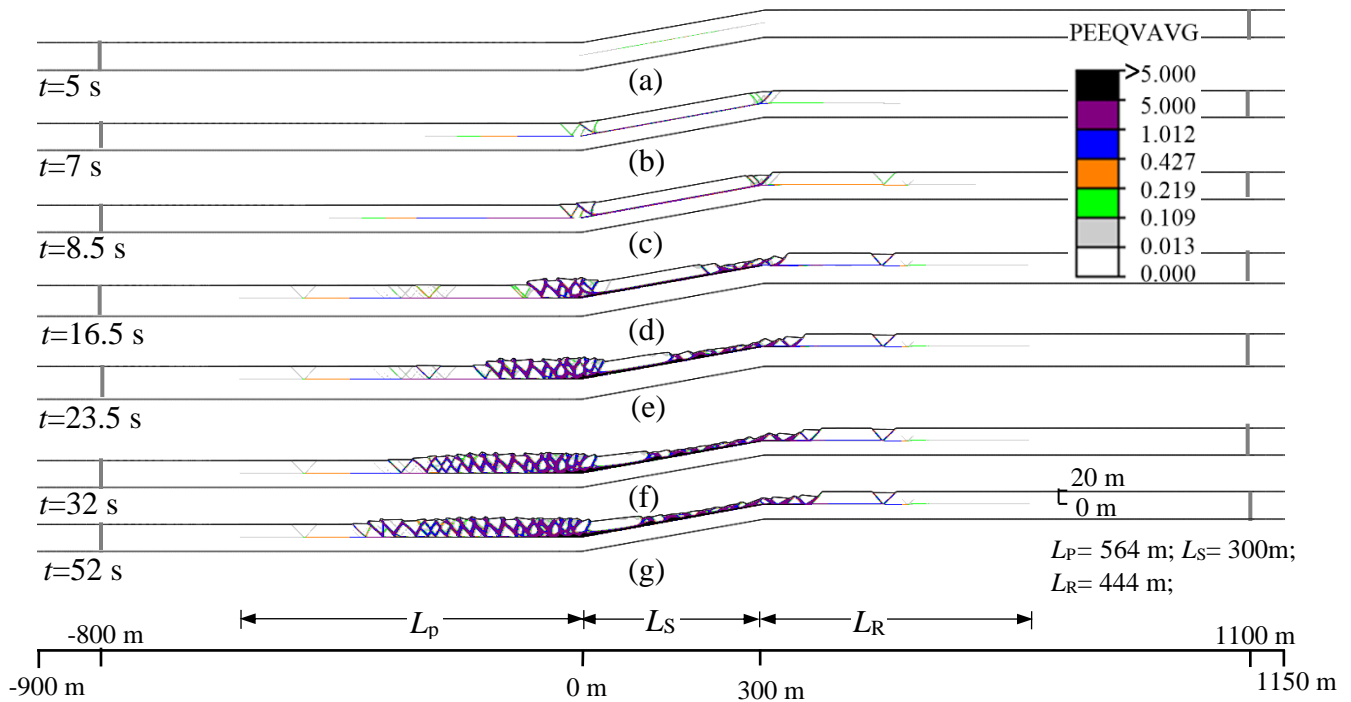
Figure 4.17: Model-II: Slope failure for equivalent earthquake based on Approach-4

In Approaches-5 and -6, the acceleration is applied for a long period ($t = t_{\text{sig}} = 8.33$ s); however, the maximum seismic coefficient is obtained from Pyke's chart (1991) (pseudostatic coefficient) is used with a rectangular (Approach-5) and triangular (Approach-6) variation with time, as shown in Figs. 4.8(e) and 4.8(f), respectively.

Figures 4.18–4.21 show the simulation results for Models-I and -II with Approaches-5 and -6. As the area of the rectangular variation (Approach-5) is double that of the triangular variation (Approach-6), the overall extent of failure at the end of the earthquake loading period ($t = 8.33$ s) for Approach-5 is greater than that for Approach-6 (see Figs. 4.18(b) & 4.20(c)). For Model-I, the maximum lateral extent (L_E) is 752 m and 676 m for Approaches-5 and -6, respectively. Similar failure patterns developed in Model-II (Figs. 4.19 & 4.21); however, the maximum lateral extent of the landslides were slightly different: for the rectangular pulse the $L_E = 884$ m,

71

L_P = 375 m, occurring at $t > 47$ s, while for the triangular pulse the L_E = 730 m, with L_R = 80 m and L_P = 350 m, occurring at $t > 47$ s.
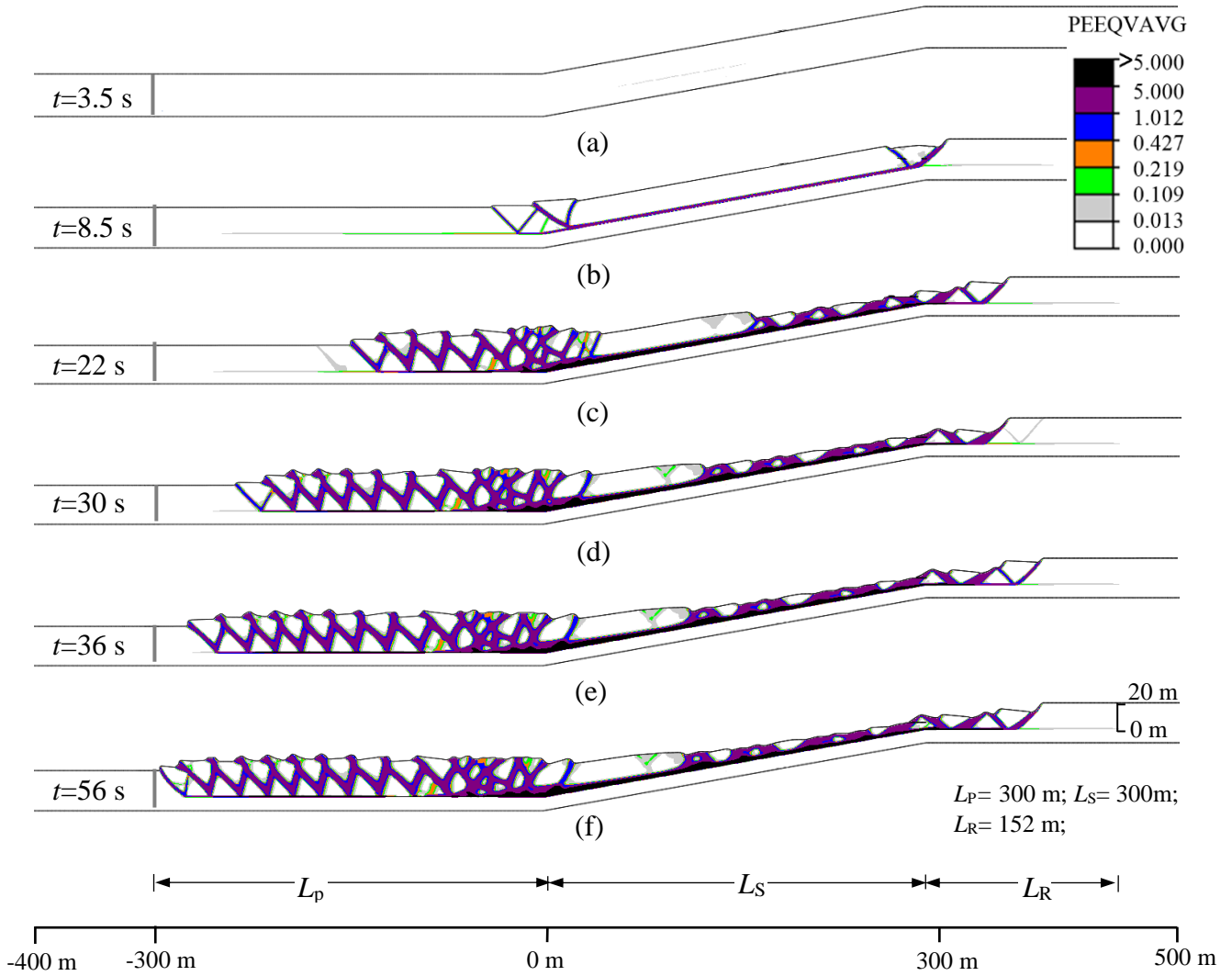
Figure 4.18: Model-I: Slope failure for equivalent earthquake based on Approach-5

PEEQVAVG

(black)	>5.000
(purple)	5.000
(blue)	1.012
(orange)	0.427
	0.219
(green)	0.109
(gray)	0.013
(white)	0.000

t=4.5 s (a)

t=8.5 s (b)

t=10.5 s (c)

t=20 s (d)

t=30 s (e)

20 m
0 m

t=40 s (f)

L_P= 375 m; L_S= 300m;
L_R= 209 m;

t=60 s (g)

-800 m

$\longmapsto L_p \longrightarrow|\longleftarrow L_S \longrightarrow|\longleftarrow L_R \longrightarrow|$

-900 m   0 m   300 m   750 m
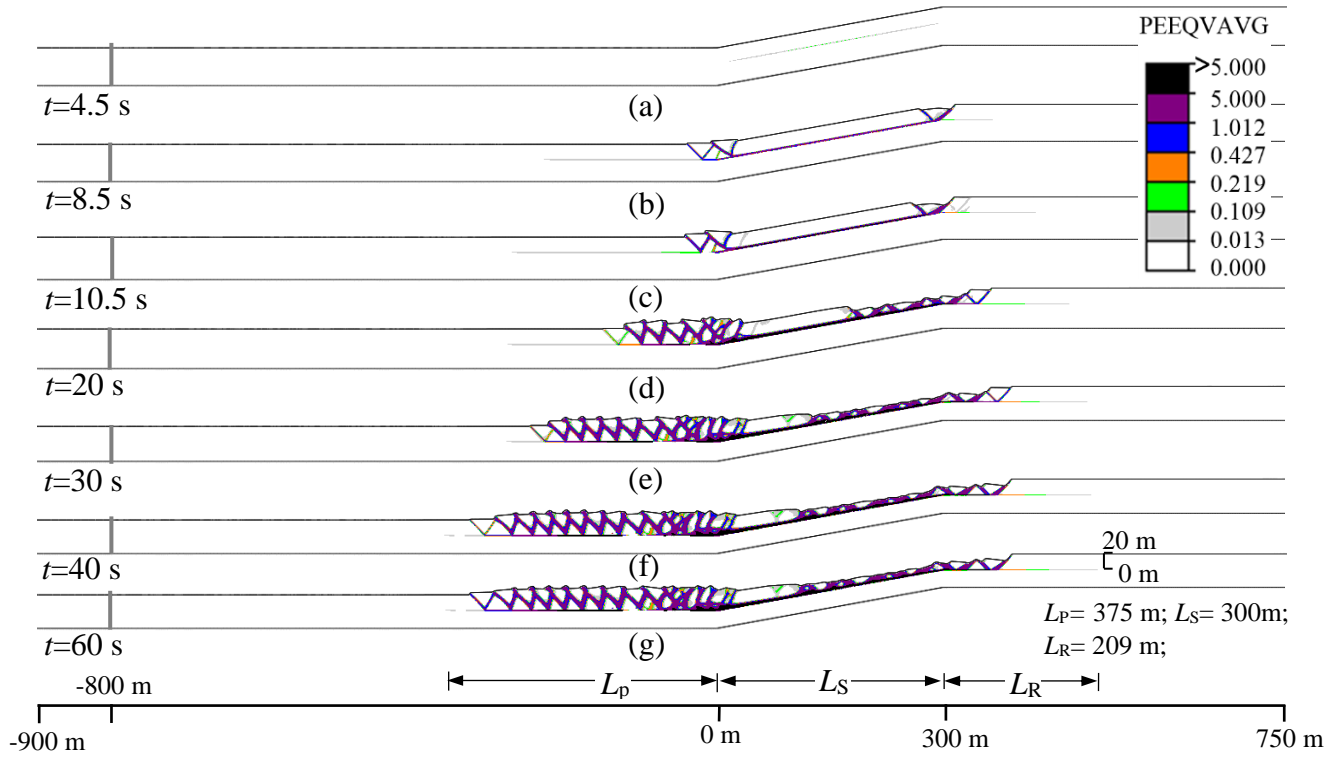
Figure 4.19: Model-II: Slope failure for equivalent earthquake based on Approach-5

73

Figure 4.20: Model-I: Slope failure for equivalent earthquake based on Approach-6
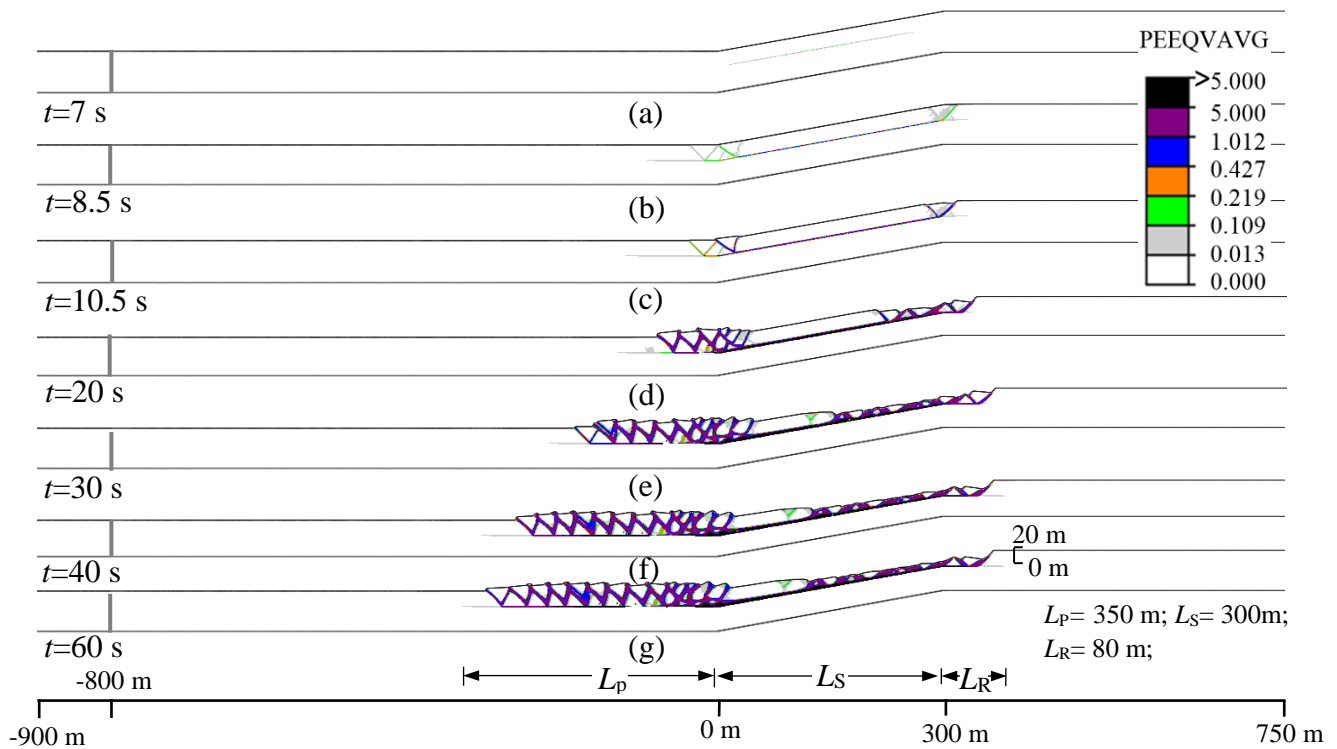
Figure 4.21: Model-II: Slope failure for equivalent earthquake based on Approach-6

4.10   Comparison between dynamic and modified pseudostatic FE analysis

Figures 4.22 and 4.23 show the comparison of the ploughing (L_p) and retrogression (L_R) distances, respectively, obtained from the dynamic and modified pseudostatic FE analyses with different earthquake loadings. As the slopes are stable under gravity loading, L_p and L_R are equal to zero, and therefore this segment is not shown in these figures. The horizontal axis of these figures represents the time starting from the application of earthquake loading, which is not the same, as shown in Fig. 4.8. However, it provides a better comparison because it shows the failure process starting from the earthquake loading.

The main objective of the comparison is to show the performance of the simplified pseudostatic approaches as compared to full dynamic analysis (solid lines versus other lines in Figs. 4.22 and 4.23) for retrogression and run-out modeling. Figures 4.22 and 4.23 show that Approaches-3, -4 and -5 give ploughing and retrogression distances very different from the values obtained from full dynamic analysis. Figure 4.22(a) shows that the L_p for Approaches -4 and -5 is significantly higher than dynamic analysis results, at least up to 35 s, which is because of the application of acceleration for a long period ($t = t_{sig} = 8.33$ s). At a given time, L_p is higher in Approach-4 than in Approach-5, which is because of the magnitude of the k applied (see Figs. 4.8(d) and 4.8(e)). In Approach-3, k is gradually increased with time (Fig. 4.8(c)) and then maintained as constant; therefore, L_p increases slowly at the initial stage as compared to the simulation results for Approaches-4 and -5. Figure 4.22(a) shows that the L_p is ~300 m for all the pseudostatic approaches except for Approach-3, because the ploughing reaches the downslope strong layer located at 300 from the toe. In Approach-3, $L_p > 300$ m is obtained after 38.5 s, which is because of the run-out of accumulated soil mass over the seabed, as shown in Fig. 4.14. Finally, the calculated L_p with Approaches-1, -2 and -6 is very comparable to the full dynamic analysis results for both Model-I and –II, although the dynamic model gives a slightly lower L_p at long time (Fig. 4.22).

Very similar pattern is found for upslope retrogression—the retrogression distances (L_R) obtained from Approaches-1, -2 and -6 are comparable to the dynamic analysis results, while Approaches-3, -4 and -5 give higher L_R than the dynamic analysis.
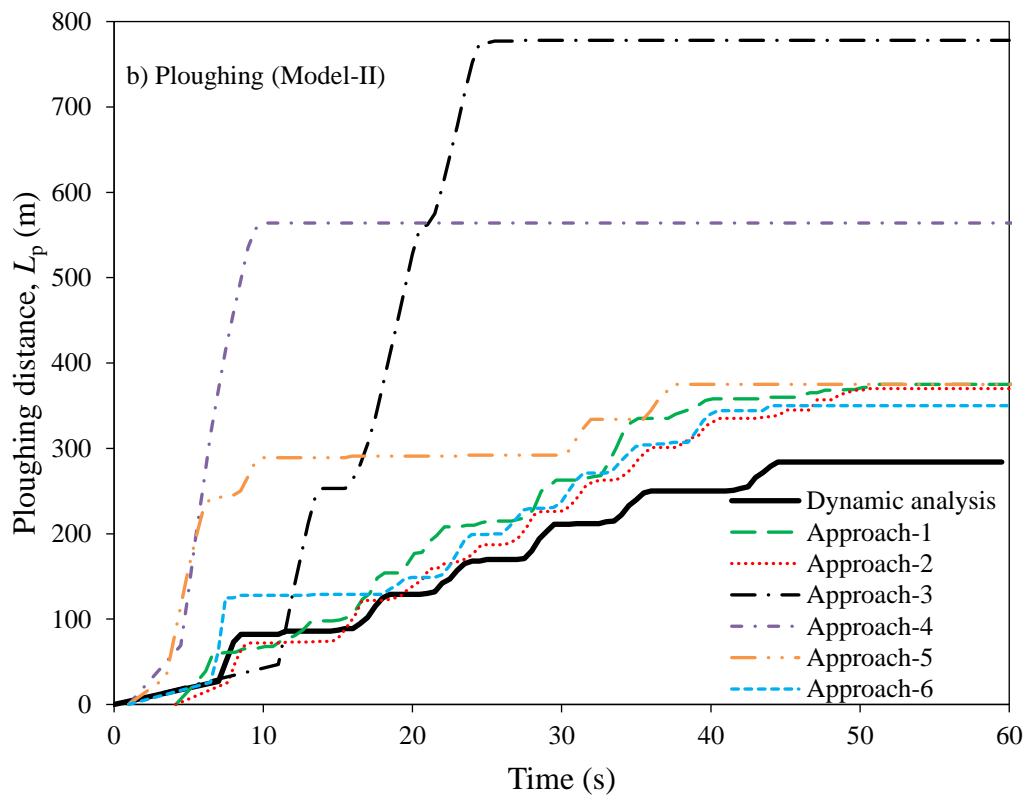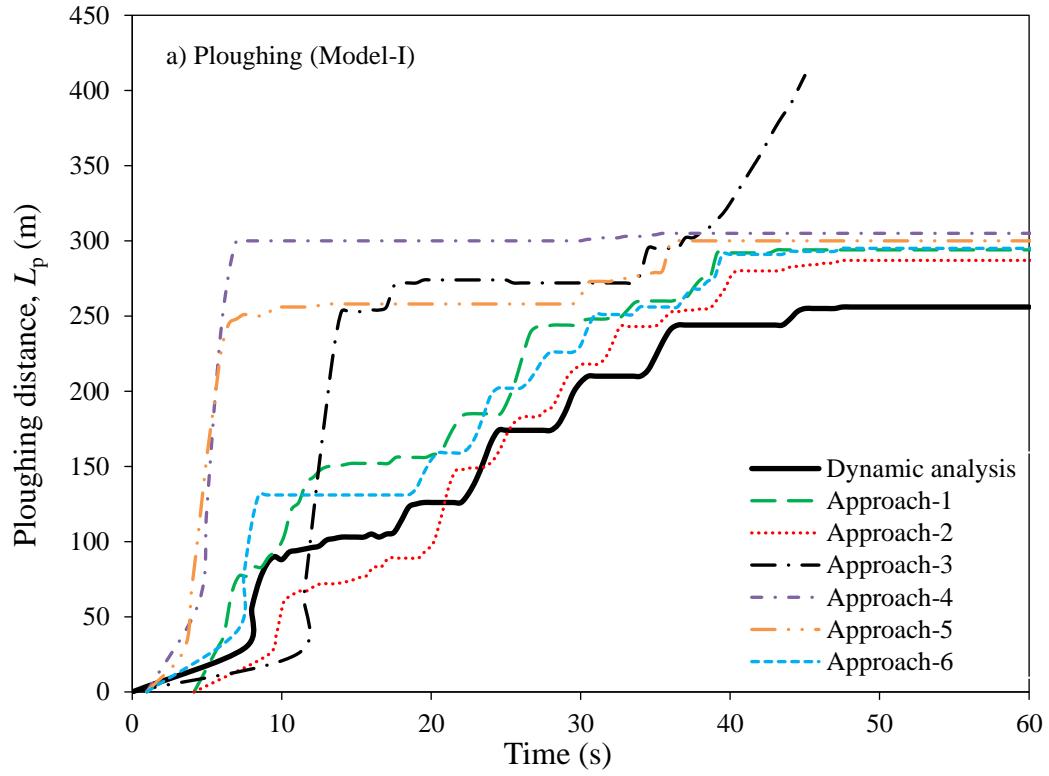
Figure 4.22: Comparison of ploughing failure length for different earthquake loadings
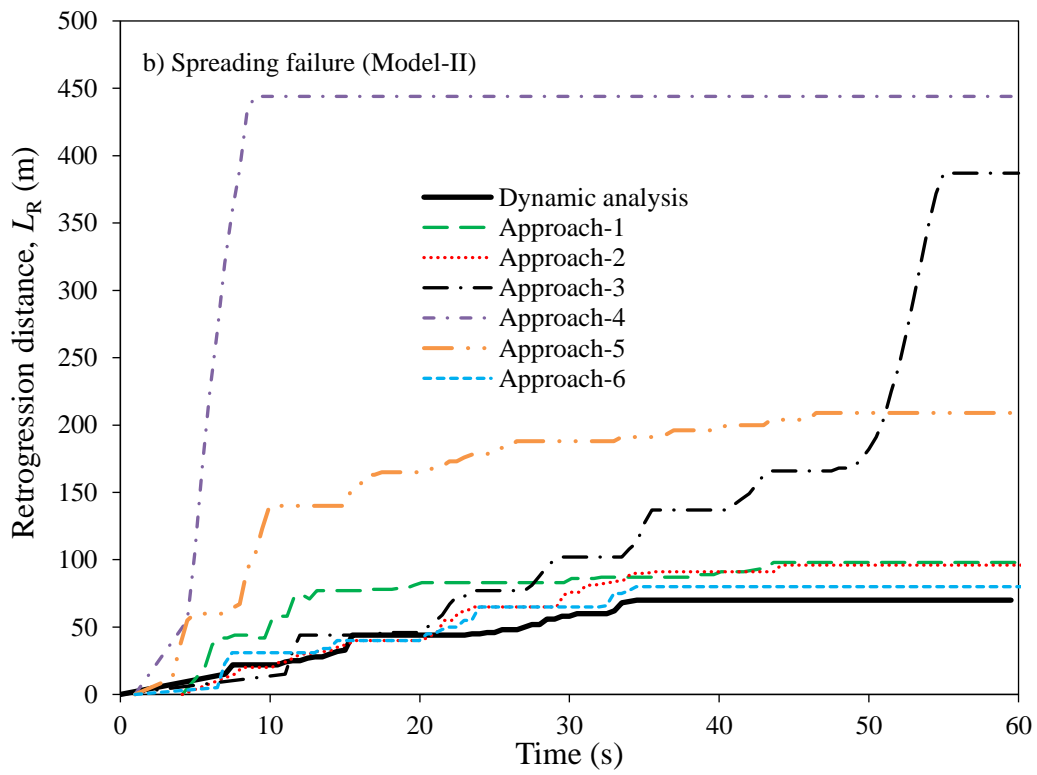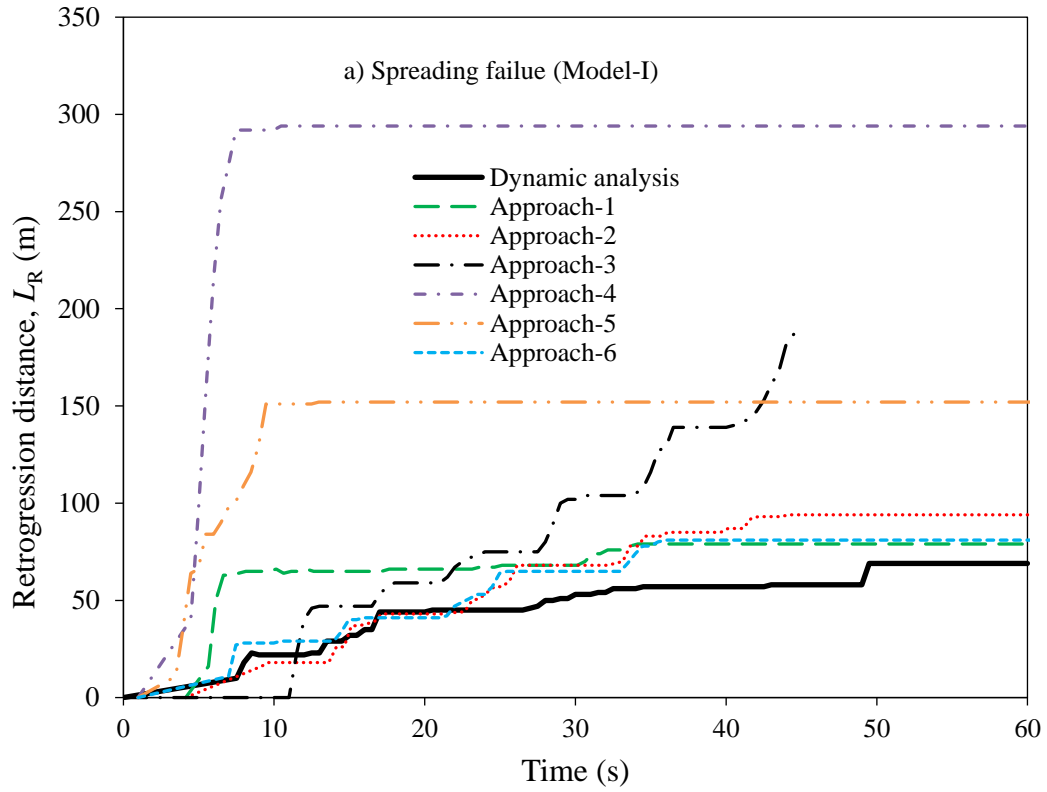
Figure 4.23: Comparison of upslope retrogression for different earthquake loadings

4.11 Summary

The main aim of this chapter is to study large-deformation offshore slope failures due to an earthquake, using dynamic FE analysis and modified pseudostatic FE analysis. In the dynamic FE analysis, an acceleration time history is applied at the base of the model, and in the modified pseudostatic FE analysis, six approaches are used with different pulse-like body forces to simulate the earthquake effect. Although the soil profiles and geotechnical properties are idealized, the present numerical analysis can explain the spreading, ploughing and run-out failure mechanisms. The following presents the summary of the findings of the numerical analyses presented in this chapter.

The large-deformation FE modeling technique in Abaqus can successfully simulate the combined progressive and retrogressive failure of a very long submarine slope during an earthquake. The Whittier Narrows earthquake acceleration time history is implemented to the base of the model in the dynamic analysis. Failure begins through the weak layer of sensitive marine clay in the steeper slope and then propagates in both the upslope and downslope directions. In the upslope spreading, failure happens due to a reduction of support, and downslope, ploughing-type failure occurs due to an increase in soil pressure. The failure patterns obtained from the current analysis are comparable to those from the field observations of Paleo-landslides in the Caspian Sea.

Comparison of the results obtained from the offshore submarine slope using dynamic FE analysis and modified pseudostatic FE analysis show that a triangular/rectangular pulse-like body force within half of the predominant period, or a triangular pulse over a significant duration (Approaches-1, 2 & 6), show comparable horst- and graben-type spreading and ploughing failure patterns, and the distances of spreading and ploughing are similar to the dynamic analyses. When the pseudostatic coefficient is higher, the duration should be lower, and vice versa.

CHAPTER 5

Conclusions and Future Recommendations

5.1   Conclusions

It has been inferred that many submarine landslides are triggered by gas hydrate dissociation and earthquake loading, and the existence of a weak marine sensitive clay layer(s) might be a prerequisite for large-scale landslides. The occurrence of such landslides poses a great threat to nearby offshore oil and gas facilities, and to save the billions of dollars in the cost of those facilities, a better understating of the failure processes and evaluation of their impact is necessary. This type of large-scale landslide cannot be analyzed using typical limit equilibrium methods, and so, in the present study, finite-element modeling of the seabed slope is performed in order to simulate the initiation of failure through a strain-softening clay layer and subsequent large deformation of the failed soil mass.

The soil is modeled as an Eulerian material that flows through the fixed mesh without causing any numerical issue related to mesh distortion. Gas hydrates dissociation is modeled by reducing the undrained shear strength of the soil in a small segment of a steeper slope. To study the earthquake-induced landslides, dynamic analysis is performed by applying the Whittier Narrows earthquake acceleration time history at the base of the model to initiate the failure of the slope through the strain-softening weak clay layer in the form of a thin shear band where significantly large strain concentration occurs. Propagation of the shear band causes downslope ploughing and upslope retrogressive failure of soil blocks. As large-deformation dynamic finite-element analysis is challenging, FE simulations are also performed based on simplified approaches for earthquake

loading using pulse-like body forces (modified pseudostatic method), and the results are compared with the dynamic FE analysis. The following conclusions can be drawn from this study.

➤ The present Eulerian-based FE model can successfully simulate large-deformation progressive and retrogressive failures due to weakening of a thin zone of soil, which could result from gas hydrate dissociation and earthquake loading.

➤ The dynamic FE analysis results are comparable with those of the proposed modified pseudostatic FE analysis if a higher value of body force is applied as a triangular pulse within half of the predominant period, or if a lower value of body force is applied as a triangular pulse within the significant earthquake duration.

➤ Failure initiation is the critical part of the landslide, and the initial failure can develop within a short period of time during an earthquake. Depending upon the peak acceleration of an earthquake and the earthquake-loading duration, the numerical simulation results could change.

➤ The formation and propagation of a shear band in a weak zone (e.g., a sensitive clay layer) can cause a slab-type failure in the steeper section if the shear-band propagation through the strain-softening clay layer is sufficiently long.

➤ After a global failure of the steep slope, the shear band propagates in the upslope and downslope stable zones. The lateral extent of the shear band depends on the lengths of the marine and glacial clay layers in the stable zone and the earthquake loading period and magnitude.

- Large deformation of soil above the failure plane in the steep slope causes upslope settlement and downslope heaving, and progressive downward propagation of shear bands causes ploughing failure with the formation of passive failure blocks.

- Run-out over the seabed occurs when the pile-up soil mass height is greater than the maximum sustainable height.

5.2   Future Recommendations

- Although the present numerical FE simulated failure patterns are similar to the interpreted failure patterns from field investigations (e.g., Paleo-landslides in the Caspian Sea), the analyses are performed for an idealized condition, including slope geometry, soil properties and earthquake loading.

- All the analyses are performed for an undrained loading condition, and the effects of shear strain rate on undrained shear strength are not considered.

- Analyses are performed for only one earthquake, and further study is required for different earthquake loadings. The applicability of the modified pseudostatic method needs to be verified for different earthquakes, slope geometries and soil properties. However, it should be noted that the finite-element analysis presented in this study is computationally very expensive.

- The uplift of the passive failure block downslope could develop a high breakoff velocity, which could generate a tsunami wave. Further study is required with water and soil models to simulate these processes.

➢ The downslope run-out distance could increase with the reduction of sediment strength, and the re-molded soil mass can develop slumping, debris/mud and turbidity currents. The impact force of those flows on offshore subsea pipelines needs to be investigated further.

REFERENCES

Ambraseys, N.N., and Srbulov, M. 1995. Earthquake induced displacements of slopes. Soil Dynamics and Earthquake Engineering, **14**: 59–71.

Ambraseys, N.N., and Menu, J.M. 1988. Earthquake-induced ground displacements. Earthquake Engineering & Structural Dynamics, **16**(7): 985–1006.

Andresen, L., and Jostad, H.P. 2007. Numerical modeling of failure mechanisms in sensitive soft clay-application to offshore geohazards. *In* Proceedings of the Offshore Technology Conference, April 30–May 3, Houston, Texas, USA, OTC 18640.

Azizian, A. 2004. Seismic analysis of submarine slopes: retrogressive and three-dimensional effects. Ph.D. thesis, Faculty of Engineering and Applied Science, Memorial University of Newfoundland, St John's, NL, Canada.

Azizian, A., and Popescu, R. 2003. Finite element simulation of retrogressive failure of submarine slopes. In Locat, J., Mienert, J., Boisvert, L. (eds.): Submarine Mass Movements and Their Consequences, Advances in Natural and Technological Hazards Research, Vol. 19.

Azizian, A., and Popescu, R. 2006. Three-dimensional seismic analysis of submarine slopes. Soil Dynamics and Earthquake Engineering, **26**(9): 870–887.

Bardet, J.P., Synolakis, C.E., Davies, H.L., Imamura, F., and Okal, E.A. 2003. Landslide tsunamis: recent findings and research directions. Pure and Applied Geophysics, **160**: 1793–1809.

Benson, D. J. 1992. Computational methods in Lagrangian and Eulerian hydrocodes. Computer Methods in Applied Mechanics and Engineering, **99**: 235–394.

Benson, D.J., and Okazawa, S. 2004. Contact in a multi-material Eulerian finite element formulation. Computer Methods in Applied Mechanics and Engineering, **193**: 4277–4298.

Bernander, S. 2000. Progressive landslides in long natural slopes: formation, potential extension

and configuration of finished slides in strain-softening soils. Licentiate thesis, Luleå University of Technology, Luleå, Sweden.

Bhandari, T., Hamad, F., Moormann, C., Sharma, K.G., and Westrich, B. 2016. Numerical modelling of seismic slope failure using MPM. Computers and Geotechnics, **75**: 126–134.

Biscontin, G., Pestana, J.M., and Nadim, F. 2004. Seismic triggering of submarine slides in soft cohesive soil deposits. Marine Geology, **203**(3–4): 341–354.

Bornhold, B.D., Fine, I. V, Rabinovich, A.B., Thomson, R.E., and Kulikov, E.A. 2003. The Grand Banks landslide-generated tsunami of November 18, 1929: analysis and numerical modeling. Geophysical Research Abstracts, **5**: 01775.

Bray, J.D., and Travasarou, T. 2007. Simplified procedure for estimating earthquake-induced deviatoric slope displacements. Journal of Geotechnical and Geoenvironmental Engineering, **133**(4): 381–392.

Bray, J.D., and Travasarou, T. 2009. Pseudostatic coefficient for use in simplified seismic slope stability evaluation. Journal of Geotechnical and Geoenvironmental Engineering, **135**(9): 1336–1340.

Bryn, P., Berg, K., Forsberg, C.F., Solheim, A., and Kvalstad, T.J. 2005. Explaining the Storegga Slide. Marine and Petroleum Geology, **22**: 11–19.

Bugge, T., Befring, S., Belderson, R.H., Eidvin, T., Jansen, E., Kenyon, N.H., Holtedahl, H., and Sejrup, H.P. 1987. A giant three-stage submarine slide off Norway. Geo-Marine Letters, **7**(4): 191–198.

Cai, Z., and Bathurst, R.J. 1996. Deterministic sliding block methods for estimating seismic displacements of earth structures. Soil Dynamics and Earthquake Engineering, **15**(4): 255–268.

California Division of Mines and Geology. 1997. Guidelines for evaluating and mitigating seismic hazards in California. California Division of Mines and Geology Special Publication, **117**: 74.

Canals, M., Lastras, G., Urgeles, R., Casamor, J.L., Mienert, J., Cattaneo, A., De Batist, M., Haflidason, H., Imbo, Y., Laberg, J.S., Locat, J., Long, D., Longva, O., Masson, D.G., Sultan, N., Trincardi, F., and Bryn, P. 2004. Slope failure dynamics and impacts from seafloor and shallow sub-seafloor geophysical data: case studies from the COSTA project. Marine Geology, **213**: 9–72.

Carlson, P.R., and Molnia, B.F. 1977. Submarine faults and slides on the continental shelf, northern Gulf of Alaska. Marine Georesources & Geotechnology, **2**: 275–290.

Chen, W., Li, T., and Qiu, T. 2013. Parametric study on earthquake-induced slope deformations. Geo-Congress 2013, March 3–7, San Diego, California, USA, pp. 1216–1225.

Chen, Z., Wang, J., Wang, Y., Yin, J. H., and Haberfield, C. 2001. A three-dimensional slope stability analysis method using the upper bound theorem Part II: numerical approaches, applications and extensions. International Journal of Rock Mechanics and Mining Sciences, **38**(3): 379–397.

Corps of Engineers. 1982. Engineering and design manual–slope stability. Engineering Manual, pp. 2–1110.

Dadson, S.J., Hovius, N., Chen, H., Dade, W.B., Lin, J.C., Hsu, M.L., Lin, C.W., Horng, M.J., Chen, T.C., and Milliman, J. 2004. Earthquake-triggered increase in sediment delivery from an active mountain belt. Geology, **32**(8): 733–736.

Dan, G., Sultan, N., and Savoye, B. 2007. The 1979 Nice harbour catastrophe revisited: trigger mechanism inferred from geotechnical measurements and numerical modelling. Marine

Geology, **245**: 40–64.

Dey, R. 2015. Analytical and numerical modeling of progressive failure of onshore and offshore slopes with sensitive clay layer. Ph.D. thesis, Faculty of Engineering and Applied Science, Memorial University of Newfoundland, St John's, NL, Canada.

Dey, R., Hawlader, B., Phillips, R., and Soga, K. 2015. Large deformation finite-element modelling of progressive failure leading to spread in sensitive clay slopes. Géotechnique, **65**(8): 657–668.

Dey, R., Hawlader, B.C., Phillips, R., and Soga, K. 2016a. Numerical modelling of submarine landslides with sensitive clay layers. Géotechnique, **66**(6): 454–468.

Dey, R., Hawlader, B.C., Phillips, R., and Soga, K. 2016b. Modeling of large deformation behaviour of marine sensitive clays and its application to submarine slope stability analysis. Canadian Geotechnical Journal, **53**(7): 1138–1155.

Dimakis, P., Elverhøi, A., Høeg, K., Solheim, A., Harbitz, C., Laberg, J.S., O. Vorren, T., and Marr, J. 2000. Submarine slope stability on high-latitude glaciated Svalbard-Barents Sea margin. Marine Geology, **162**(2–4): 303–316.

Dingle, R. V. 1977. The anatomy of a large submarine slump on a sheared continental margin (SE Africa). Journal of the Geological Society, **134**(3): 293–310.

Dingle, R. V. 1980. Large allochthonous sediment masses and their role in the construction of the continental slope and rise off southwestern Africa. Marine Geology, **37**: 333–354.

Duncan, M. 1996. State of the art: limit equilbrium and finite-element analysis of slopes. Journal of Geotechnical Engineering, **122**(7): 577–596.

Dutta, S., Hawlader, B., and Phillips, R. 2015. Finite element modeling of partially embedded pipelines in clay seabed using Coupled Eulerian–Lagrangian method. Canadian Geotechnical

Journal, **52**(1): 58–72.

Einav, I., and Randolph, M.F. 2005. Combining upper bound and strain path methods for evaluating penetration resistance. International Journal for Numerical Methods in Engineering, **63**(14): 1991–2016.

Embley, R.W. 1980. The role of mass transport in the distribution and character of deep-ocean sediments with special reference to the North Atlantic. Marine Geology, **38**: 23–50.

Fine, I. V., Rabinovich, A.B., Bornhold, B.D., Thomson, R.E., and Kulikov, E.A. 2005. The Grand Banks landslide-generated tsunami of November 18, 1929: Preliminary analysis and numerical modeling. Marine Geology, **215**: 45–57.

Franklin, A.G., and Chang, F.K. 1977. Permanent displacements of earth embankments by Newmark sliding block analysis. Earthquake Resistance of Earth and Rock Fill Dams, Rept. 5, Misc. Paper No. S-71-17, pp. 59.

Frydman, S., and Talesnick, M. 1988. Analysis of seismically triggered slides off Israel. Environmental Geology Water Science, **11**(1): 21–26.

Garagash, D.I., and Germanovich, L.N. 2012. Nucleation and arrest of dynamic slip on a pressurized fault. Journal of Geophysical Research: Solid Earth, **117**.

Gardner, J. V., Prior, D.B., and Field, M.E. 1999. Humboldt slide - A large shear-dominated retrogressive slope failure. Marine Geology, **154**: 323–338.

Gauer, P., Kvalstad, T.J., Forsberg, C.F., Bryn, P., and Berg, K. 2005. The last phase of the Storegga Slide: simulation of retrogressive slide dynamics and comparison with slide-scar morphology. Marine and Petroleum Geology, **22**(1–2): 171–178.

Gee, M.J.R., Gawthorpe, R.L., and Friedmann, J.S. 2005. Giant striations at the base of a submarine landslide. Marine Geology, **214**(1–3): 287–294.

Gee, M.J.R., Gawthorpe, R.L., and Friedmann, S.J. 2006. Triggering and evolution of a giant submarine landslide, offshore Angola, revealed by 3D seismic stratigraphy and geomorphology. Journal of Sedimentary Research, **76**(1): 9–19.

Gee, M.J.R., Uy, H.S., Warren, J., Morley, C.K., and Lambiase, J.J. 2007. The Brunei slide: a giant submarine landslide on the North West Borneo margin revealed by 3D seismic data. Marine Geology, **246**(1): 9–23.

Ghobrial, F., Karray, M., Delisle, M.C., and Ledoux, C. 2015. Development of spectral pseudostatic method for dynamic clayey slope stability analysis. 68th Candian Geotechnical Conference, September 21–23, Quebec, Canada.

Ghosh, B., and Madabhushi, S.P.G. 2003. A numerical investigation into effects of single and multiple frequency earthquake motions. Soil Dynamics and Earthquake Engineering, **23**(8): 691–704.

Gray, T., Puzrin, A., and Hill, A. 2015. Application of the shear band propagation method to slope stability analysis of a palaeo landslide in the Caspian Sea. *In* Proceedings of the offshore technology conference, May 4–7, Houston, Texas, USA, OTC 25869-MS.

Grelle, G., Revellino, P., and Guadagno, F.M. 2011. Methodology for seismic and post-seismic stability assessment of natural clay slopes based on a viscoplastic behaviour model in simplified dynamic analysis. Soil Dynamics and Earthquake Engineering, **31**(9): 1248–1260.

Griffiths, D. V, and Marquez, R.M. 2007. Three-dimensional slope stability analysis by elasto-plastic finite elements. Geotechnique, **57**(6): 537–546.

Gylland, A.S., Jostad, H.P., and Nordal, S. 2014. Experimental study of strain localization in sensitive clays. Acta Geotechnica, **9**: 227–240.

Hadj-Hamou, T., and Kavazanjian, E. 1985. Seismic stability of gentle infinite slopes. Journal of

Geotechnical Engineering, **111**(6): 681–697.

Haflidason, H., Lien, R., Sejrup, H.P., Forsberg, C.F., and Bryn, P. 2005. The dating and morphometry of the Storegga Slide. Marine and Petroleum Geology, **22**(1–2): 123–136.

Hampton, M.A., Lee, H.J., and Beard, R.M. 1982. Geological interpretation of cone penetrometer tests in Norton Sound, Alaska. Geo-Marine Letters, **2**(3): 223–230.

Hampton, M.A., Lee, H.J., and Locat, J. 1996. Submarine landslides. Reviews of Geophysics, **34**(1): 33–59.

Harbitz, C.B. 1992. Model simulations of tsunamis generated by the Storegga Slides. Marine Geology, **105**: 1–21.

Ho, I. 2014. Parametric studies of slope stability analyses using three-dimensional finite element technique: geometric effect. Journal of GeoEngineering, **9**(1): 33–43.

Hynes-Griffin, M.E., and Franklin, A.G. 1984. Rationalizing the seismic coefficient method. U.S. Army Corps of Engineers Waterways Experiment Station, Miscellaneous Paper GL-84–13, pp. 37.

Idelsohn, S.R., Onate, E., and Del Pin, F. 2004. The particle finite element method: a powerful tool to solve incompressible flows with free surfaces and breaking waves. International Journal for Numerical Methods in Engineering, **61**(7): 964–989.

Imbo, Y., De Batist, M., Canals, M., Prieto, M.J., and Baraza, J. 2003. The Gebra slide: a submarine slide on the Trinity Peninsula Margin, Antarctica, Marine Geology, **193**(3): 235–252.

Islam, N., and Hawlader, B. 2016. Pseudostatic seismic slope stability analyses using a large deformation finite element modeling technique. 69th Candian Geotechnical Conference, October 2–5, Vancouver, Canada.

Jibson, R.W. 2007. Regression models for estimating coseismic landslide displacement. Engineering Geology, **91**: 209–218.

Jibson, R.W. 2011. Methods for assessing the stability of slopes during earthquakes–a retrospective. Engineering Geology, **122**: 43–50.

Kawata, Y., Benson, B.C., Borrero, J.C., Borrero, J.L., Davies, H.L., Lange, W.P., Imamura, F., Letz, H., Nott, J., and Synolakis, C.E. 1999. Tsunami in Papua New Guinea was as intense as first thought. Eos, Transactions American Geophysical Union, **80**(9): 101–105.

Khosravi, M., Leshchinsky, D., Meehan, C.L., and Khosravi, A. 2013. Stability analysis of seismically loaded slopes using finite element techniques. Geo-Congress 2013, March 3–7, San Diego, California, USA.

Kourkoulis, R., Anastasopoulos, I., Gelagoti, F., and Gazetas, G. 2010. Interaction of foundation-structure systems with seismically precarious slopes: numerical analysis with strain softening constitutive model. Soil Dynamics and Earthquake Engineering, **30**(12): 1430–1445.

Kramer, S.L. 1996. Geotechnical Earthquake Engineering. Upper Saddle River: Prentice Hall, **6**: 653.

Kramer, S.L., and Smith, M.W. 1997. Modified Newmark model for seismic displacements of compliant slopes. Journal of Geotechnical and Geoenvironmental Engineering, **123**(7): 635–644.

Kvalstad, T.J., Andresen, L., Forsberg, C.F., Berg, K., Bryn, P., and Wangen, M. 2005a. The Storegga slide: evaluation of triggering sources and slide mechanics. Marine and Petroleum Geology, **22**: 245–256.

Kvalstad, T.J., Nadim, F., Kaynia, A.M., Mokkelbost, K.H., and Bryn, P. 2005b. Soil conditions and slope stability in the Ormen Lange area. Marine and Petroleum Geology, **22**: 299–310.

Kvenvolden, K.A., and McMenamin, M.A. 1980. Hydrates of natural gas: a review of their geologic occurrence. US Department of the Interior, US Geological Survey, Circular 825, Arlington, Virginia, USA.

L'Heureux, J.S., Longva, O., Steiner, A., Hansen, L., Vardy, M.E., Vanneste, M., Haflidason, H., Brendryen, J., Kvalstad, T.J., and Forsberg, C.F. 2012. Identification of weak layers and their role for the stability of slopes at Finneidfjord, Northern Norway. In Y. Yamada et al. (eds.): Submarine Mass Movements and Their Consequences, Advances in Natural and Technological Hazards Research, **31**: 321–330.

Laberg, J.S., and Vorren, T.O. 2000. The Trænadjupet Slide, offshore Norway - morphology, evacuation and triggering mechanisms. Marine Geology, **171**: 95–114.

Laberg, J.S., Vorren, T.O., Mienert, J., Haflidason, H., Bryn, P., and Lien, R. 2003. Preconditions leading to the Holocene Trænadjupet slide offshore Norway. In Locat, J., Mienert, J. (eds.): Submarine Mass Movements and Their Consequences, pp. 247–254.

Lebuis, J., Robert, J.M., and Rissmann, P. 1983. Regional mapping of landslide hazard in Quebec. *In* Proceedings of the Symposium on Slopes on Soft Clays, Swedish Geotechnical Institute, Linkoping, Sweden. Report No. 17, pp. 205–262.

Lee, H.J. 2009. Timing of occurrence of large submarine landslides on the Atlantic Ocean margin. Marine Geology, **264**(1): 53–64.

Lee, H.J., Edwards, B.D., Field, M.E., and Survey, U.S.G. 1981. Geotechnical analysis of a submarine slump. 13th Annual Offshore Technology Conference, May 4–7, Houston, TX, USA.

Lee, H.J., Syvitski, J.P.M., and Hutton, E.W.H. 2002. Distinguishing sediment waves from slope failure deposits: field examples, including the Humboldt Slide, and modelling results. Marine

Geology, **192**: 79–104.

Leynaud, D., Mienert, J., and Nadim, F. 2004. Slope stability assessment of the Helland Hansen area offshore the mid-Norwegian margin. Marine Geology, **213**(1–4): 457–480.

Li, X. 2007. Finite element analysis of slope stability using a nonlinear failure criterion. Computers and Geotechnics, **34**(3): 127–136.

Locat, A., Jostad, H.P., and Leroueil, S. 2013. Numerical modeling of progressive failure and its implications for spreads in sensitive clays. Canadian Geotechnical Journal, **50**: 961–978.

Locat, A., Leroueil, S., Bernander, S., Demers, D., Jostad, H.P., and Ouehb, L. 2011. Progressive failures in eastern Canadian and Scandinavian sensitive clays. Canadian Geotechnical Journal, **48**(11): 1696–1712.

Locat, A., Leroueil, S., Bernander, S., Demers, D., Locat, J., and Ouehb, L. 2008. Study of a lateral spread failure in an eastern Canada clay deposit in relation with progressive failure: the Saint Barnabé-Nord slide. *In* Proceedings of GeoHazards 2008, May 20–24, Quebec, Canada. pp. 89–96.

Locat, A., Leroueil, S., Demers, D., and Locat, J. 2014a. Landslides in sensitive clays. Advances in Natural and Technological Hazards Research, Vol. 36.

Locat, A., Leroueil, S., Fortin, A., Demers, D., and Jostad, H.P. 2014b. The 1994 landslide at Sainte-Monique, Quebec: geotechnical investigation and application of progressive failure analysis. Canadian Geotechnical Journal, **52**(4): 490–504.

Locat, J., Lee, H., ten Brink, U.S., Twichell, D., Geist, E., and Sansoucy, M. 2009. Geomorphology, stability and mobility of the Currituck slide. Marine Geology, **264**(1–2): 28–40.

Locat, J., and Lee, H.J. 2002. Submarine landslides: advances and challenges. Canadian

Geotechnical Journal, **39**(1): 193–212.

Loukidis, D., Bandini, P., and Salgado, R. 2003. Stability of seismically loaded slopes using limit analysis. Geotechnique, **53**(5): 463–479.

Low, H.E., and Randolph, M.F. 2010. Strength measurement for near-seabed surface soft soil using manually operated miniature full-flow penetrometer. Journal of Geotechnical and Geoenvironmental Engineering, **136**(11): 1565–1573.

Lunne, T., and Andersen, K.H. 2007. Soft clay shear strength parameters for deepwater geotechnical design. *In* Proceedings of the 6th International Offshore Site Investigations and Geotechnics Conference, September 11–13, London, UK, pp. 151–176.

Lunne, T., Berre, T., Andersen, K.H., Strandvik, S., and Sjursen, M. 2006. Effects of sample disturbance and consolidation procedures on measured shear strength of soft marine Norwegian clays. Canadian Geotechnical Journal, **43**(7): 726–750.

Lykousis, V. 1991. Submarine slope instabilities in the Hellenic arc region, northeastern Mediterranean Sea. Marine Georesources & Geotechnology, **10**(1–2): 83–96.

Makdisi, F.I., and Seed, H.B. 1977. A simplified procedure for estimating earthquake-induced deformations in dams and embankments. In: Rept. UCB/EERC-77/19, Earthquake Eng. Res. Center.

Marcuson III, W.F. 1981. Earth dams and stability of slopes under dynamic loads. *In* Proceedings of the International Conference on Recent Advances in Geotechnical Earthquake Engineering and Soil Dynamics, St. Louis, Missouri, Vol. 3, pp. 1175.

Marcuson III, W.F., and Franklin, A.G. 1983. Seismic design, analysis, and remedial measures to improve stability of existing earth dams. Corps of Engineers Approach, in Seismic Design of Embankments and Caverns, T. R. Howard, Ed., New York, USA.

Martinez, J.F., Cartwright, J., and Hall, B. 2005. 3D seismic interpretation of slump complexes: examples from the continental margin of Israel. Basin Research, **17**(1): 83–108.

Martino, S. 2016. Earthquake-induced reactivation of landslides: recent advances and future perspectives. Earthquakes and Their Impact on Society, 291–322.

Maslin, M., Owen, M., Day, S., and Long, D. 2004. Linking continental-slope failures and climate change: testing the clathrate gun hypothesis. Geology, **32**(1): 53–56.

Masson, D.G., Harbitz, C.B., Wynn, R.B., Pedersen, G., and Lovholt, F. 2006. Submarine landslides: processes, triggers and hazard prediction. Philosophical Transactions of the Royal Society, **364**: 2009–2039.

Matsui, T., and San, K.C. 1992. Finite element slope stability analysis by shear strength reduction technique. Soils and Foundations, **32**(1): 59–70.

Matsuo, M., Itabashi, K., and Sasaki, Y. 1984. Study on aseismicity of earth structures by inverse analyses of actual cases. *In* Proceedings of the Japan Society of Civil Engineers, **343**: 25–33.

McSaveney, M.J., Goff, J.R., Darby, D.J., Goldsmith, P., Barnett, A., Elliott, S., and Nongkas, M. 2000. The 17 July 1998 tsunami, Papua New Guinea: evidence and initial interpretation. Marine Geology, **170**(1): 81–92.

Mello, U.T., and Pratson, L.F. 1999. Regional slope stability and slope-failure mechanics from the two-dimensional state of stress in an infinite slope. Marine Geology, **154**(1): 339–356.

Melo, C., and Sharma, S. 2004. Seismic coefficients for pseudostatic slope analysis. 13th World Conference on Earthquake Engineering, August 1–6, Vancouver, B.C., Canada.

Micallef, A. 2007. Failure processes in submarine landslides: a geomorphological approach. Ph.D. dissertation, University of Southampton, England.

Micallef, A., Masson, D.G., Berndt, C., and Stow, D.A. 2007. Submarine spreading: dynamics and

development. Submarine Mass Movements and Their Consequences, Dordrecht, 119–127.

Mienert, J., Berndt, C., Laberg, J.S., and Vorren, T.O. 2002. Slope instability of continental margins. *In* Ocean Margin Systems, 179–193.

Monaghan, J.J. 1988. An introduction to SPH. Computer Physics Communications, **48**(1): 89–96.

Moore, D.G., Curray, J.R., and Emmel, F.J. 1976. Large submarine slide (olistostrome) associated with Sunda Arc subduction zone, northeast Indian Ocean. Marine Geology, **21**(3): 211–226.

Nadi, B., Askari, F., and Farzaneh, O. 2014. Seismic performance of slopes in pseudostatic designs with different safety factors. Iranian Journal of Science & Technology, **38**(2): 465–483.

Nadim, F., Biscontin, G., and Kaynia, A.M. 2007. Seismic triggering of submarine slides. *In* Proceedings of the Offshore Technology Conference, April 30–May 3, Houston, TX, USA, OTC 18911.

Nadim, F., and Kalsnes, B. 1997. Evaluation of clay strength for seismic slope stability analysis. *In* Proceedings of the International Conference on Soil Mechanics and Foundation Engineering, September 6–12, Hamburg, Vol. 1, 377-379.

Nadim, F., and Whitman, R. V. 1983. Seismically induced movement of retaining walls. Journal of Geotechnical Engineering, **109**(7): 915–931.

Nazem, M., Carter, J.P., and Airey, D.W. 2009. Arbitrary Lagrangian–Eulerian method for dynamic analysis of geotechnical problems. Computers and Geotechnics, **36**(4): 549–557.

Nazem, M., Sheng, D., Carter, J.P., and Sloan, S.W. 2008. Arbitrary Lagrangian–Eulerian method for large-strain consolidation problems. International Journal for Numerical and Analytical Methods in Geomechanics, **32**(9): 1023–1050.

Newmark, N.M. 1965. Effects of earthquakes on dams and embankments. Géotechnique, **15**(2): 139–160.

Newton, C.S., Mosher, D.C., and G.D., W. 2004. Importance of mass transport complexes in the quaternary development of the Nile Fan, Egypt. Offshore Technology Conference, May 3–6, Houston, Texas, USA, OTC 16742.

Nian, T.K., Huang, R.Q., Wan, S.S., and Chen, G.Q. 2012. Three-dimensional strength-reduction finite element analysis of slopes: geometric effects. Canadian Geotechnical Journal, **49**(5): 574–588.

Nichol, S.L., Hungr, O., and Evans, S.G. 2002. Large-scale brittle and ductile toppling of rock slopes. Canadian Geotechnical Journal, **39**(4): 773–788.

Nixon, M.F., and Grozic, J.L.H. 2007. Submarine slope failure due to gas hydrate dissociation: a preliminary quantification. Canadian Geotechnical Journal, **44**(3): 314–325.

Norwegian Geotechnical Institute. 1997. Earthquake hazard and submarine slide. Submarine Slides a Literature Survey, NGI Report 963014-1.

Oñate, E., Idelsohn, S.R., Del Pin, F., and Aubry, R. 2004. The particle finite element method— an overview. International Journal of Computational Methods, **1**(2): 267–307.

Palmer, A.C., and Rice, J.R. 1973. The growth of slip surfaces in the progressive failure of overconsolidated clay. Proceedings of the Royal Society of London, Series A: Mathematical, Physical and Engineering Sciences, **332**(1591): 527–548.

Park, D.S., and Kutter, B.L. 2015. Static and seismic stability of sensitive clay slopes. Soil Dynamics and Earthquake Engineering, **79**: 118–129.

Pauli, C.K., Ussler, W., and Dillon, W.P. 2000. Potential role of gas hydrate decomposition in generating submarine slope failures. Natural Gas Hydrate, 149–156.

Pestana, J.M., and Biscontin, G. 2001. A simplified model describing the cyclic behavior of lightly overconsolidated clays in simple shear. Geotechnical Engineering Report No.

UCB/GT/2000-03, Department of Civil and Environmental Engineering, University of California, Berkeley, pp. 1-67.

Pestana, J.M., and Nadim, F. 2000. Nonlinear site response analysis of submerged slopes. Geotechnical Engineering Report No. UCB/GT/2000, Department of Civil and Environmental Engineering. University of California, Berkeley, pp. 1–51.

Pinkert, S., and Klar, A. 2016. Enhanced strain-softening model from cyclic full-flow penetration tests. Journal of Geotechnical and Geoenvironmental Engineering, **142**(3): 4015087.

Piper, D.J.W., and Aksu, A.E. 1987. The source and origin of the 1929 grand banks turbidity current inferred from sediment budgets. Geo-Marine Letters, **7**(4): 177–182.

Piper, D.J.W., Cochonat, P., and Morrison, M.L. 1999. The sequence of events around the epicentre of the 1929 Grand Banks earthquake: initiation of debris flows and turbidity current inferred from sidescan sonar. Sedimentology, **46**(1): 79–97.

Popenoe, P., Schmuck, E.A., Dillon, W.P., and Schwab, W. 1993. The Cape Fear landslide: slope failure associated with salt diapirism and gas hydrate decomposition. In Schwab, W. C., Lee, H. J., Twichell, D. C., (eds.): Submarine Landslides: Selected Studies in the U.S. Exclusive Economic Zone, U.S. Geological Survey Bulletin 2002, pp. 40-53.

Pradel, D., Smith, P.M., Stewart, J.P., and Raad, G. 2005. Case history of landslide movement during the Northridge earthquake. Journal of Geotechnical and Geoenvironmental Engineering, **131**(11): 1360–1369.

Prior, D.B., Doyle, E.H., and Neurauter, T. 1986. The Currituck Slide, mid-Atlantic continental slope—revisited. Marine Geology, **73**(1–2): 25–45.

Puzrin, A.M. 1996. The behaviour of soft clay under irregular cyclic loading. D.Sc. thesis, Faculty of civil engineering, Technion-Israel Institute of technology, Technion, Haifa.

Puzrin, A.M. 2016. Simple criteria for ploughing and runout in post-failure evolution of submarine landslides. Canadian Geotechnical Journal, **53**: 1305–1314.

Puzrin, A.M., and Germanovich, L.N. 2005. The growth of shear bands in the catastrophic failure of soils. Proceedings of the Royal Society of London, Series A: Mathematical, Physical and Engineering Sciences, **461**(2056): 1199–1228.

Puzrin, A.M., Germanovich, L.N., and Friedli, B. 2016. Shear band propagation analysis of submarine slope stability. Géotechnique, **66**(3): 188–201.

Puzrin, A.M., Gray, T.E., and Hill, A.J. 2015. Significance of the actual nonlinear slope geometry for catastrophic failure in submarine landslides. Proceedings of the Royal Society of London, Series A: Mathematical, Physical and Engineering Sciences, **471**(2175): 20140772.

Puzrin, A.M., Gray, T.E., and Hill, A.J. 2017. Retrogressive shear band propagation and spreading failure criteria for submarine landslides. Géotechnique, **67**(2): 95–105.

Puzrin, A.M., Kim, S., and Germanovich, L.N. 2004. Catastrophic failure of submerged slopes in normally consolidated sediments. Géotechnique, **54**(10): 631–643.

Pyke, R. 1991. Selection of seismic coefficients for use in pseudostatic slope stability analyses. Consulting Engineer, Lafayette.

Quinn, P., Diederichs, M.S., Hutchinson, D.J., and Rowe, R.K. 2007. An exploration of the mechanics of retrogressive landslides in sensitive clay. *In* Proceedings of the 60th Canadian Geotechnical Conference, October 21–24, Ottawa, Canada, pp. 721–727.

Quinn, P.E. 2009. Large landslides in sensitive clay in eastern Canada and the associated hazard and risk to linear infrastructure. Ph.D. thesis, Queen's University.

Randolph, M.F. 2004. Characterisation of soft sediments for offshore applications. *In* Proc. 2nd Int. Conf. on Site Characterisation, Porto, Portugal, Vol. 1, pp. 209–231.

Randolph, M.F., Hefer, P.A., Geise, J.M., and Watson, P.G. 1998. Improved seabed strenght profiling using T-bar penetrometer. Offshore Site Investigation and Foundation Behaviour 'New Frontiers: Proceedings of an International Conference, September 22–24, London, UK.

Richards Jr, R., and Elms, D.G. 1979. Seismic behavior of gravity retaining walls. Journal of Geotechnical and Geoenvironmental Engineering, **105**(4), 449–464.

Rodríguez-Ochoa, R., Nadim, F., and Hicks, M.A. 2015. Influence of weak layers on seismic stability of submarine slopes. Marine and Petroleum Geology, **65**: 247–268.

Roy, S., and Hawlader, B. 2017. Finite element modeling of progressive and retrogressive failure of submarine slopes for varying angle of inclination. 70th Canadian Geotechnical Conference, October 1–4, Ottawa, Canada.

Sarma, S.K. 1975. Seismic stability of earth dams and embankments. Geotechnique, **25**(4): 743–761.

Sarma, S.K., and Chlimintzas, G.O. 2001. Co-seismic & post-seismic displacements of slopes. 15th ICSMGE TC4 Satellite Conference, August 25, Istanbul, Turkey.

Sarma, S.K., and Tan, D. 2008. Finite element verification of an enhanced limit equilibrium method for slope analysis. Géotechnique, **58**(6): 481–487.

Saygili, G., and Rathje, E.M. 2008. Empirical predictive models for earthquake-induced sliding displacements of slopes. Journal of Geotechnical and Geoenvironmental Engineering, **134**(6): 790–803.

Schwab, W., Danforth, W.W., and Scanlon, K.M. 1992. Tectonic and stratigraphic control on a giant submarine slope failure: Puerto Rico insular slope. In Schwab, W. C., Lee, H. J., Twichell, D. C., (eds.): Submarine Landslides: Selected Studies in the U.S. Exclusive Economic Zone, U.S. Geological Survey Bulletin 2002, pp. 60–68.

Schwab, W.C., Lee, H.J., and Twichell, D.C. 1993. Submarine landslides: selected studies in the U.S. Exclusive Economic Zone, U.S. Geological Survey Bulletin 2002, U.S. Geological Survey, Reston, VA.

Seed, H.B. 1979. Considerations in the earthquake-resistant design of earth and rockfill dams. Geotechnique, **29**(3): 215–263.

Shanmugam, G., and Wang, Y. 2015. The landslide problem. Journal of Palaeogeography, **4**(2): 109–166.

Sigarán-Loría, C., Kaynia, A.M., and Hack, R. 2007. Soil stability under earthquakes: a sensitivity analysis. *In* Proceedings of the 4th international conference on earthquake geotechnical engineering, June 25, Thessaloniki, Greece.

Soga, K., Alonso, E., Yerro, A., Kumar, K., and Bandara, S. 2016. Trends in large-deformation analysis of landslide mass movements with particular emphasis on the material point method. Géotechnique, **66**(3): 248–273.

Solheim, A., Berg, K., Forsberg, C.F., and Bryn, P. 2005. The Storegga Slide complex: repetitive large scale sliding with similar cause and development. Marine and Petroleum Geology, **22**(1–2): 97–107.

Solheim, S.L.Y.T.K. a, and Forsberg, C.F. 2007. Slope stability at Northern Flank of Storegga slide. *In* Proceedings of the Seventeenth International Offshore and Polar Engineering Conference, July 1–6, Lisbon, Portugal.

Stark, T.D., and Contreras, I.A. 1996. Constant volume ring shear apparatus. Geotechnical Testing Journal, **19**(1): 3–11.

Stewart, D.P., and Randolph, M.F. 1994. T-bar penetration testing in soft clay. Journal of Geotechnical Engineering, **120**(12): 2230–2235.

Strasser, M., Stegmann, S., Bussmann, F., Anselmetti, F.S., Rick, B., and Kopf, A. 2007. Quantifying subaqueous slope stability during seismic shaking: Lake Lucerne as model for ocean margins. Marine Geology, **240**(1–4): 77–97.

Suito, H., and Freymueller, J.T. 2009. A viscoelastic and afterslip postseismic deformation model for the 1964 Alaska earthquake. Journal of Geophysical Research: Solid Earth, **114**(11): 1–23.

Sulsky, D., Zhou, S.-J., and Schreyer, H.L. 1995. Application of a particle in cell method to solid mechanics. Computer Physics Communications, **87**(1–2): 236–252.

Sultan, N., Cochonat, P., Foucher, J.P., and Mienert, J. 2004. Effect of gas hydrates melting on seafloor slope instability. Marine Geology, **213**(1–4): 379–401.

Sultan, N., Cochonat, P., Foucher, J.P., Mienert, J., Haflidason, H., and Sejrup, H.P. 2003. Effect of gas hydrates dissociation on seafloor slope stability. In Locat, J., Mienert, J. (eds.): Submarine mass movements and their consequences, pp. 103–111.

Sultan, N., Savoye, B., Jouet, G., Leynaud, D., Cochonat, P., Henry, P., Stegmann, S., and Kopf, A. 2010. Investigation of a possible submarine landslide at the Var delta front (Nice slope - SE France). Canadian Geotechnical Journal, **47**(4): 486–496.

Taiebat, M., and Kaynia, A.M. 2010. A practical model for advanced nonlinear analysis of earthquake effects in clay slopes. Fifth International Conference on Recent Advances in Geotechnical Earthquake Engineering and Soil Dynamics, May 24, San Diego, California, USA.

Talling, P., Clare, M., Urlaub, M., Pope, E., Hunt, J., and Watt, S. 2014. Large submarine landslides on continental slopes: geohazards, methane release, and climate change. Oceanography, **27**(2): 32–45.

Taniguchi, E., and Sasaki, Y. 1985. Back analysis of a landslide due to the Naganoken Seibu earthquake of September 14, 1984. *In* Proc. of 11th International Conference on Soil Mechanics and Foundation Engineering, August 12–16, Sanfrancisco, California, USA.

Tappin, D.R., Matsumoto, T., Watts, P., Satake, K., McMurtry, G.M., Matsuyama, M., Lafoy, Y., Tsuji, Y., Kanamatsu, T., and Lus, W. 1999. Sediment slump likely caused 1998 Papua New Guinea tsunami. Eos, Transactions American Geophysical Union, **80**(30): 329–340.

Tavenas, F., Flon, P., Leroueil, S., and Lebuis, J. 1983. Remolding energy and risk of slide retrogression in sensitive clays. *In* Proceedings of the Symposium on Slopes on Soft Clays, Linköping, Sweden, SGI Report. 17, 423–454.

Terzaghi, K. 1950. Mechanism of landslides. Application of geology to engineering practice, Geological Society of America, New York, pp. 83–123.

Thakur, V. 2007. Strain localization in sensitive soft clays. Doctoral thesis, Norwegian University of Science and Technology, Trondheim, Norway.

Tjelta, T., Strout, J., Solheim, A., Mokkelbost, K.H., Berg, K., and Bryn, P. 2002. Geological and geotechnical site investigations in the Storegga Slide area. International Conference Offshore Site Investigation and Geotechnics, November 26–28, London, UK.

Trapper, P.A., Puzrin, A.M., and Germanovich, L.N. 2015. Effects of shear band propagation on early waves generated by initial breakoff of tsunamigenic landslides. Marine Geology, **370**: 99–112.

Ugai, K., and Leshchinsky, D.O. V. 1995. Three-dimensional limit equilibrium and finite element analyses: a comparison of results. Soils and Foundations, **35**(4): 1–7.

Viesca, R.C., and Rice, J.R. 2012. Nucleation of slip-weakening rupture instability in landslides by localized increase of pore pressure. Journal of Geophysical Research: Solid Earth, **117**(3).

Viesca, R.C., Templeton, E.L., and Rice, J.R. 2008. Off-fault plasticity and earthquake rupture dynamics: 2. Effects of fluid saturation. Journal of Geophysical Research: Solid Earth, **113**(B9).

Wang, D., Randolph, M.F., and White, D.J. 2013. A dynamic large deformation finite element method based on mesh regeneration. Computers and Geotechnics, **54**: 192–201.

Wang, D., Zhang, L., Xu, J., and He, M. 2009. Seismic stability safety evaluation of gravity dam with shear strength reduction method. Water Science and Engineering, **2**(2): 52–60.

Watson-Lamprey, J., and Abrahamson, N. 2006. Selection of ground motion time series and limits on scaling. Soil Dynamics and Earthquake Engineering, **26**(5): 477–482.

Watson, P.G., Newson, T.A., and Randolph, M.F. 1998. Strength profiling in soft offshore soils. *In* Proc. 1st Int. Conf. On Site Characterisation-ISC'98, April 19–22, Balkema, Rotterdam, pp. 1389–1394.

Whelan, T., Coleman, J.M., Suhayda, J.N., and Roberts, H.H. 1977. Acoustical penetration and shear strength in gas-charged sediment. Marine Georesources & Geotechnology, **2**(1–4): 147–159.

Whitman, R. V, and Liao, S. 1985. Seismic design of gravity retaining walls. Miscellaneous Paper GL-85-1, U.S. Army Engineer Waterways Experiment Station, Vicksburg, MS.

Wilson, R.C., and Keefer, D.K. 1983. Dynamic analysis of a slope failure from the 6 August 1979 Coyote Lake, California, earthquake. Bulletin of the Seismological Society of America, **73**(3): 863–877.

Wong, C.P. 1982. Seismic analysis and an improved design procedure for gravity retaining walls. Ph.D. thesis, Massachusetts Institute of Technology, Department of Civil Engineering.

Woodward, P.K., and Griffiths, D. V. 1996. Influence of viscous damping in the dynamic analysis

of an earth dam using simple constitutive models. Computers and Geotechnics, **19**(3): 245–263.

Wright, S.G., and Rathje, E.M. 2003. Triggering mechanisms of slope instability and their relationship to earthquakes and tsunamis. Pure and Applied Geophysics, **160**(10–11): 1865–1877.

Yang, S.L., Solheim, A., Kvalstad, T.J., Forsberg, C.F., and Schnellmann, M. 2006. Behaviour of the sediments in the Storegga Slide interpreted by the steady state concept. Norsk Geologisk Tidsskrift, **86**(3): 243–253.

Yegian, M.K., Marciano, E.A., and Ghahraman, V.G. 1991. Seismic risk analysis for earth dams. Journal of Geotechnical Engineering, **117**(1): 18–34.

Zhang, W., Wang, D., Randolph, M.F., and Puzrin, A.M. 2015. Catastrophic failure in planar landslides with a fully softened weak zone. Geotechnique, **65**(9): 755–769.

Zhuang, J., Cui, P., Hu, K., Chen, X., and Ge, Y. 2010. Characteristics of earthquake-triggered landslides and post-earthquake debris flows in Beichuan County. Journal of Mountain Science, **7**(3): 246–254.